Effects of Buoyancy Source Composition on Multiphase Plume Behavior in Stratification

by

Aaron C. Chow

Submitted to the Department of Civil and Environmental Engineering
in partial fulfillment of the requirements for the degree of

Master of Science in Civil and Environmental Engineering

at the

MASSACHUSETTS INSTITUTE OF TECHNOLOGY

June 2004

Author . . . .
Department of Civil and Environmental Engineering
May 21, 2004

Certified by . . . .
E. Eric Adams
Senior Research Engineer of Civil and Environmental Engineering
Thesis Supervisor

Accepted by . . . .
Heidi Nepf
Chairman, Committee for Graduate Students

Effects of Buoyancy Source Composition on Multiphase Plume Behavior in Stratification

by

Aaron C. Chow

Submitted to the Department of Civil and Environmental Engineering
on May 21, 2004, in partial fulfillment of the
requirements for the degree of
Master of Science in Civil and Environmental Engineering

Abstract

Experiments are performed where a dense multiphase plume is released vertically in a salinity stratified ambient. The constituent phase composition of the initial buoyancy flux can be dense brine, particles, or a mixture of the two in a prescribed ratio. The resulting trapping heights and peeling depths are recorded by visual acquisition and from dye fluorescence measurements. Also, the radial concentration distribution of the dispersed phase after the first peeling event is obtained by collecting the settled particles from the bottom of the tank. Analytical models assuming plug flow and well-mixed particle distributions within the intrusion layer are used to predict the spread of the particle distribution based on initial buoyancy flux, momentum flux, stratification parameter and particle fall velocity. The effects of initial momentum and volume flux on peel and trap depths were studied by comparing the predictions from these models. Finally the observed results are compared to a single-phase plume numerical prediction (CORMIX) and a multiphase numerical plume model. Observed peeling depths were not sensitive to buoyancy composition, while observed trap depths decreased slightly with high particle fractions, possibly from the 'lift-off' phenomenon where particle fallout decreases the bulk buoyancy of the intrusion layer. The observed radial distribution was Gaussian, consistent with particles being vertically well mixed in the intrusion layer, and the standard deviation agreed well with predictions.

Thesis Supervisor: E. Eric Adams
Title: Senior Research Engineer of Civil and Environmental Engineering

Acknowledgments

This work was supported by the Ocean Carbon Sequestration Program, Biological and Environmental Research (BER), U.S. Dept. of Energy (grant number DE-FG02-01ER63078), the National Energy Technology Laboratory, U.S. Dept. of Energy (grant number DE-FG26-98FT40334). MIT's Martin Family Society of Fellows for Sustainability (MFSFS) also provided financial support.

I would first like to thank my thesis advisor, Eric Adams, for his immense patience and astute insight. Several Undergraduate Research Opportunities Program (UROP) members, Abigail Popp, Tom Kilpatrick and in particular Nicole Hollingsworth, contributed greatly to setting up and conducting experiments, and I would like to thank them for their help and enthusiasm.

I wish to thank all of my friends at Parsons Lab, at MIT and in Boston for their humor and support, and especially Blake Landry for sharing so many experiences with me. Finally I thank my parents, my brother Jonathan and Grandma for support from afar.

Contents

Chapter 1

Environmental Applications of Multiphase Plumes

1.1 Ocean Carbon Sequestration

The global atmospheric build-up of carbon dioxide (CO_2) and other greenhouse gases in recent history has been attributed to industrialization leading to increased fossil fuel combustion and deforestation. It is feared that rising concentrations of greenhouse gases will cause adverse changes in the climate, and that two-thirds of the change will be attributed to CO_2(Herzog et al. [29]). Possible effects include increased likelihood of extreme weather events, the rising of the mean ocean level, and even the cessation of large scale global climatological phenomena like the North Atlantic Gulf Stream (IPCC 2 [66]) Figure 1-2). Carbon sequestration in the ocean has been suggested to try to reduce the peak concentration of carbon dioxide levels, since even if overall CO_2 emissions were reduced today the climatic effects will manifest themselves long afterwards (as illustrated in Figure 1-1).

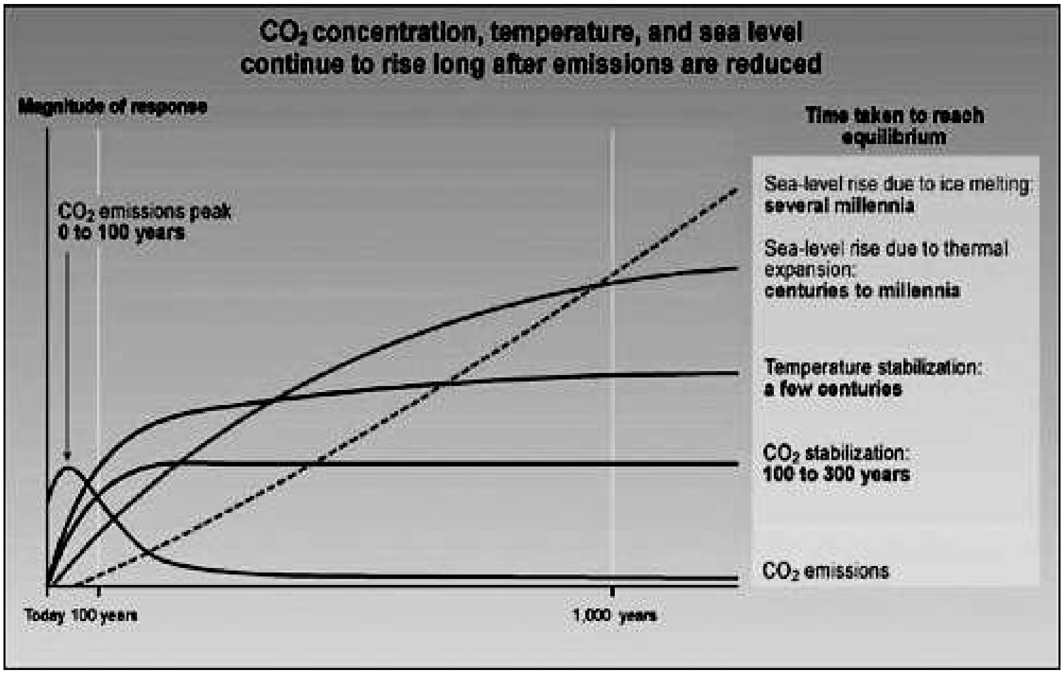

Figure 1-1: Predictions of long term atmospheric CO_2 levels, with reduced emissions, showing a continual rise to an equilibrium concentration. (Figure 5-2 of IPCC [66])

CO_2 sequestration first involves capture from their sources, one of which are coal-fired power plants. The CO_2 emissions are relatively pure from this source, and can be isolated and injected into the ocean. Herzog et al. [29] have outlined different chemical forms in which the CO_2 is delivered. Positively buoyant forms of carbon dioxide, such as liquids and gaseous forms, would go against the need for it to stay in deep ocean. Negatively buoyant forms are more favorable also because the sinking CO_2, while dissolving, will make the plume water more dense, forming a positive feedback for sinking. A number of negatively buoyant forms of CO_2 have been proposed:

Dry Ice (Nakashiki et al. [46], Caulfield [16])

Very cold CO_2 (COSMOS) (Aya et al. [9]) Dry ice and subcooled CO_2 are pure negatively buoyant forms.

CO_2/$CaCO_3$ mixtures A slurry or emulsion of carbon dioxide with basic carbonate systems. (Rau and Caldeira [47], Caldeira and Rau [11], Angelopoulos and Golomb [6])

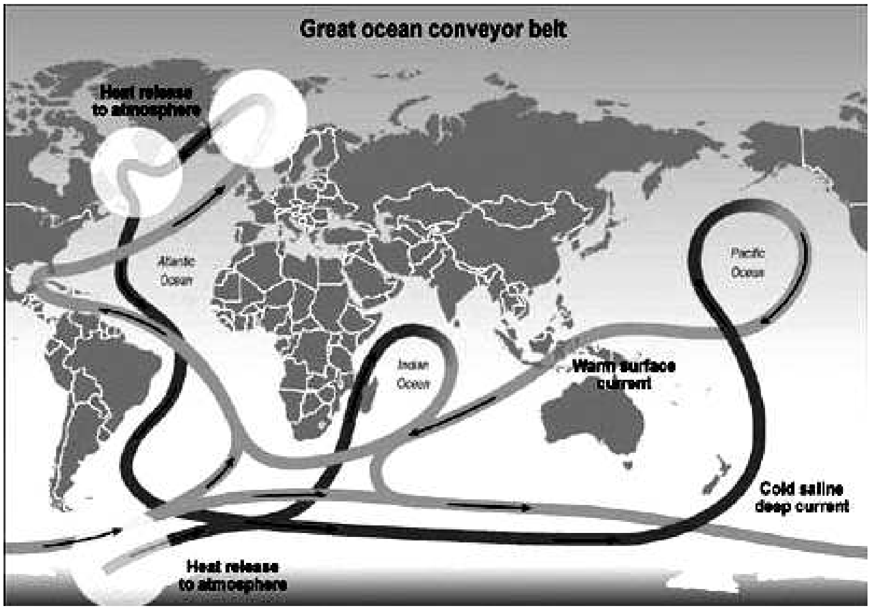

Figure 1-2: Global ocean circulation. Polar regions have significant heat exchange capability, which drives oceanic flow, and which may be threatened by rising global temperatures. (Figure 4-2 of IPCC [66])

Dense CO_2 brine solutions (Haugen and Drange [28], Adams et al. [4], Adams et al. [3], Saito et al [51]) The presence of the salt with CO_2 will induce a gravity current (a possible method for delivering carbon dioxide down the slope of ocean floors)

CO_2 Hydrate (Clathyrate Hydrate) particles (Holder et al. [31], Warzinski et al. [65]) At higher pressure (as found in ocean depths below 500m), CO_2 will form a hydrate, of specific gravity of around 1.1. Wannamaker's [64] numerical models for CO_2 hydrates predict the possibility of very deep sequestrations using these particles due to their buoyancy. The behavior of hydrates are a main focus of the current work.

Liquid CO_2 and Hydrate mixtures These may be intentionally produced as a bulk medium of CO_2 delivery, but also could be a result of incomplete reactions in forming clathrate hydrate particles from liquid CO_2 and water.

In comparing the methods above for effectiveness, one needs to consider both the persistence of the carbon dioxide once it is injected into the ocean, and also the dilution of CO_2 as it dissolves into the surrounding water. The former can be enhanced by injecting deeper under the ocean, or having a buoyancy source that sinks as far as possible. The latter is important, as is noted by Knutzen [35], since dissolved CO_2 will lower the local ocean pH, and affect marine organisms. Tamburri et al. [61] note that increased partial pressure of carbon dioxide will also have a detrimental effect on marine organisms, causing slow respiratory distress and a narcotic effect on fish. The work of Auerbach et. al. [8] and Caulfield et al. [16] on modeling lowered pH on passive marine organisms such as zooplankton show that minimizing the local pH change, by maximizing dilution, will decrease the mortality rate. Therefore the ultimate effectiveness of a method of sequestration has a large bearing on the plume dynamics of the carbon release.

1.2 Deep Sea Oil Blowout Remediation

While more efficient energy sources are being sought and developed on a large scale, the industrialized world will remain highly dependent on fossil fuels for fuel and manufacturing. As oil exploration ventures to deeper parts of the ocean, an increased risk arises from deep-ocean oil spills and blowouts, which are potentially deadly hazards to oil workers, and which have serious marine ecological consequences.

An oil well blowout occurs when deep-sea drilling encounters a region of high-pressure fluids (oil, gas or water), and the fluid flows uncontrollably towards the surface. Typically, Blowout Prevention (BOP) devices are installed at the cap of the oil well to prevent such an occurrence (Holland [32]), but in the event that such devices fail, surfactants are used to break the oil slick into smaller droplets. In order to determine where such surfactants are to be released, so as to maximize their incorporation into the plume, and also to study where these encapsulated hydrocarbons will end up on the surface, an understanding of the motion of fine droplets in plumes is necessary.

In June 2000, to better understand the plume dynamics of deep water oil spills, SINTEF conducted experimental releases of oil and gas in the Norwegian Sea to observe their behavior (SINTEF [2]). It was observed that, in the steady releases, significant amounts of oil surfaced in about half the time predicted by their droplet rise velocities. A number of multiphase flow phenomena may explain the fate of the released oil in such an experiment: the separation of phases due to crossflow current, the effect of the ambient density gradient on the motion of the oil droplets and gas bubbles, and adhesion and other interactions between the different oil phases. Ultimately, knowledge of the spread of the dispersed phase in a stratified environment is key to its containment in the case of accidents.

1.3 Reservoir Destratification

A well-studied environmental application of multiphase plumes has been reservoir destratification and lake aeration (Asaeda and Imberger [7], Lemckert and Imberger [38], Wüest et al. [68], Leitch and Baines [37], Milgram [42], McDougall [41]). Bubble plumes introduced at the bottom of a water body such as a reservoir serve to mix dense bottom water with top surface water. The purpose of destratification is to improve overall water quality and oxygen levels in the water supply. If a reservoir has a thermocline, oxygen from the atmosphere is not able to penetrate throughout the depth of the water, and fish suffer in the oxygen-deficient hypolimnion. Another effect of an anoxic hypolimnion is that the lake bottom sediments may release phosphorus, minerals (iron or manganese) and gases (hydrogen sulfide), which give undesirable taste and odor to the water supply. The presence of phosphorus may also trigger algal blooms, and destratification will help reduce the presence of algae via reduction of phosphorus and by other methods, such as reducing their exposure to sunlight. (Illinois EPA [1])

1.4 Sediment-laden plumes

Particle laden plumes are of interest for aquatic applications ranging from the transport of silt and soil in rivers and estuaries, to marine waste water disposal.

Below are two additional geophysical applications.

1.4.1 Volcanic Plumes

The study of sediment deposition due to volcanic eruptions columns is a field in itself, with relevance to diverse problems such as climate change, aircraft safety, volcanic hazards mitigation, global chemical cycles, and speciation in the deep ocean (Sparks et al. [58], Dobran [24]). The combination of hot gases and advected ash and particles in volcanic eruptions, make it a multiphase plume in the atmosphere. A study of multiphase flow is useful to predict the motions of umbrella clouds, which is an example of a plume trapping in stratification while containing particles. Pyroclastic flows are also buoyancy sources that do not stem immediately from the initial volcanic eruption, but are caused by the heated air from the lava flow travelling down the slope of a volcano. As a result, the source of buoyancy is spread much wider, and they are able to lift more particulates and aerosols into the atmosphere, causing what is called a co-ignimbrite plume. Examples of co-ignimbrite plumes include the 1980 Eruption of Mount St Helens, and Mount Pinatubo in 1991.

1.4.2 Hydrothermal Plumes

Underwater, hydrothermal plumes are also caused by volcanic activity, and often they are laden with sediment due to precipitation of minerals in the cooler environment of the sea bed (forming what are called smokers and black smokers). A schematic of a hydrothermal plume is shown in Figure 1-3. Because of the high temperature of the discharged fluid at the hydrothermal vents, the resulting flows are highly buoyant. The high temperatures also enable many chemical reactions to occur with the surrounding basaltic rock, releasing Ca, K Si and S ions. They are considered very important agents in ocean geochemical exchange, and also the home to many deep-sea chemosynthetic organisms. Smoker plumes found shallow ocean ridges can also contain gases such as methane and CO_2, forming bubble plumes.

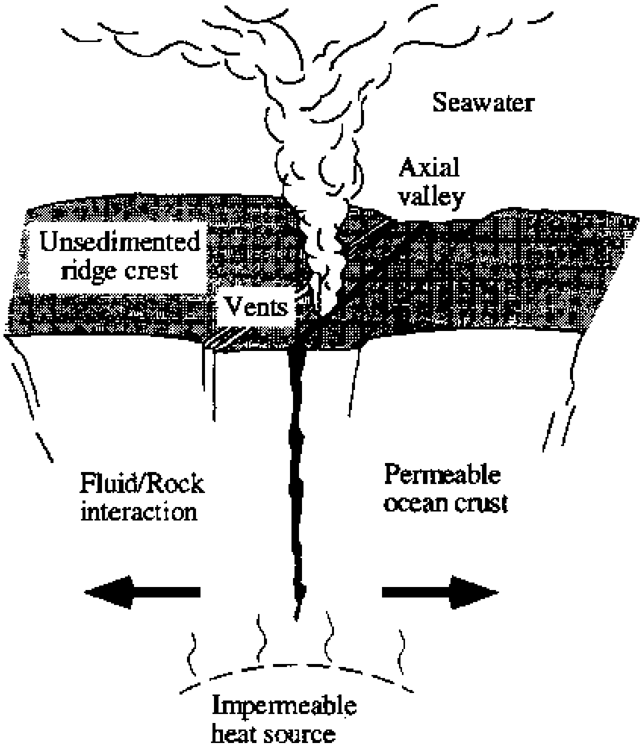

Figure 1-3: Schematic of a hydrothermal vent , from Sparks et al. (1997)

Chapter 2

Multiphase Plumes

2.1 Introduction

This chapter details the theory of multiphase plumes on which the current experiments are based, and other findings in the literature.

2.2 Single Phase Plumes

A plume is due to a steady release of a buoyant liquid, gas or particles in an environment. The motion of a pure plume is solely buoyancy-driven, as opposed to a pure jet whose motion is driven by its initial momentum. Buoyant jets, or forced plumes, are flows combining initial buoyancy and momentum. A well studied flow is the single-phase plume, where the released liquid is the same fluid as the surroundings, but is made buoyant by temperature (thermal plumes) or the presence of density-altering solutes such as salt (salinity plumes).

2.2.1 Governing Equations

For a single phase, steady thin vertical buoyant axisymmetric plume, the time-averaged governing equations are presented below (Chen and Rodi [17], McDougall [41]). Note that boundary layer approximations have already been applied which

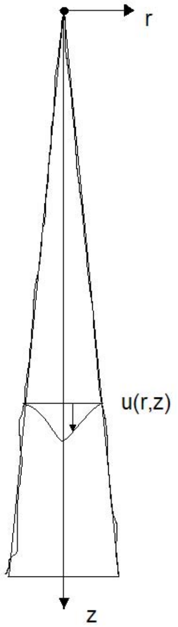

Figure 2-1: Schematic of vertical, single phase, negatively buoyant plume, showing coordinate system and an example radial velocity profile.

state that the radial derivative of a quantity is much greater than the longitudinal derivative, which is true far from the source point.

Continuity:

$$\frac{\partial(\rho ur)}{\partial z}+\frac{\partial(\rho vr)}{\partial r}=0 \tag{2.1}$$

Conservation of momentum in the longitudinal direction:

$$\frac{\partial(\rho u^2 r)}{\partial z}+\frac{\partial(\rho uvr)}{\partial r}=g(\rho-\rho_a)r-\frac{\partial}{\partial r}(r\rho\overline{u'v'}) \tag{2.2}$$

Conservation of mass (concentration):

$$\frac{\partial(\rho ucr)}{\partial z}+\frac{\partial(\rho vcr)}{\partial r}=-\frac{\partial}{\partial r}(r\rho\overline{v'c'}) \tag{2.3}$$

Conservation of thermal energy (temperature):

$$\frac{\partial(\rho uTr)}{\partial z}+\frac{\partial(\rho vTr)}{\partial r}=-\frac{\partial}{\partial r}(r\rho\overline{v'T'}) \tag{2.4}$$

u, v denote the mean local longitudinal and radial velocities, and c and T the mean local concentration of dissolved material (such as pollutant or salt) and temperature. The primed values represent the fluctuations of the value from the mean, and the overbars are time averaged values of products. In Equation 2.2, the sign of the gravitational term g is positive for negatively buoyant (sinking) plumes, where the gravity vector points in the same direction as the plume, and negatively for a rising plume. ρ_a is the local ambient density.

2.2.2 Integral Method

An approach often used in dealing with plumes is the integral method, or flux model. They are in essence the same equations as Equations 2.1 to 2.4, integrated over the entire plume cross-section. Chen and Rodi [17] show their interconversion in detail. This method offers a more physically intuitive way of viewing plume dynamics, and of keeping track of quantities of interest such as the buoyancy flux.

In the integral method for vertical buoyant flows, four fluxes across the plume cross section are of interest: volume flux V; kinematic momentum flux M; kinematic buoyancy, or density deficit 'flux' B, which can be thought of as resultant effect of the weight of the fluid and the surrounding hydrostatic pressure; and concentration flux. The definitions are given below:

$$Q = \int_0^\infty 2\pi r u dr \tag{2.5}$$

$$M = \int_0^\infty 2\pi r u^2 dr \tag{2.6}$$

$$B = \int_0^\infty 2\pi r g' u dr \tag{2.7}$$

$$J = \int_0^\infty 2\pi r \Delta c u dr \tag{2.8}$$

where

$$g' = \frac{(\rho_a - \rho)g}{\rho_0}, \tag{2.9}$$

and Δc the concentration difference of the solute with that of the ambient fluid. In defining the kinematic fluxes the Boussinesq approximation have been used, in which the density is constant except in the buoyancy terms. As a result, the equations have been divided through by ρ_0, the density of the ambient at the source point.

The resulting conservation equations for vertical plumes are:

Continuity (mass):

$$\frac{dQ}{dz} = 2\pi b(z)|v_e| = 2\pi \alpha b u|_{r=0} \tag{2.10}$$

Momentum:

$$\frac{dM}{dz} = \int_0^\infty 2\pi r g' dr \tag{2.11}$$

Buoyancy:

$$\frac{dB}{dz} = -N^2(z) \int_0^\infty 2\pi r u dr \tag{2.12}$$

Concentration of conservative pollutant, for example:

$$\frac{dJ}{dz} = 0 \tag{2.13}$$

where N is the buoyancy frequency, or Brunt-Väisälä frequency, which is given by $\left|\frac{g\partial\rho}{\rho\partial z}\right|^{1/2}$.

In Equation 2.10, the increase of volume flux with height is the entrainment flux v_e. Morton et al. [44] adapted Prandtl's second hypothesis that relates to shear layers, and suggested that the entrainment flux is directly proportional to the centerline velocity difference with the ambient (which in this case, is equal to the centerline velocity itself). The constant of proportionality is α, the entrainment coefficient, which is of order 0.1 from experiments.

2.2.3 Similarity Solution

In order to evaluate the integrals in Equations 2.10 to 2.13, it is necessary to assume a velocity and concentration profile at each cross section of the plume.

A similarity solution mathematically is used in fluid mechanics to combine two different physical variables into a new parameter, which often reduces the system of partial differential equations into a simpler ordinary differential equation for the flow. The parameter often suggests that in the flow, the two or more different physical variables contained are related to each other. Chen and Rodi [17] derive this in detail by non-dimensionalizing the differential governing equations.

Physically for the plume, the similarity solution means that, the shape of the plume cross section profile does not change even as the width of the plume increases with distance from the source. The similarity form means also that the mean velocity of any point on the plume can be expressed in terms of only the vertical distance from the source, and the radial distance away from the plume centerline. This is also called a self-similar, or a self-preserving flow. Mathematically, for any z, the local mean velocity can be described by

$$\frac{u(z)}{u|_{r=0}} = f\left(\frac{r}{b(z)}\right) \tag{2.14}$$

For mathematical simplicity, a top hat model is often used, whereby the mean velocity across a plume cross section is assumed throughout the cross section. The other model, supported by experiments (Kobus [36]), is a Gaussian profile for the velocity, concentration and temperature. For the mean plume quantity $j(r,z)$

$$\frac{j}{j|_{r=0}} = g\left(\frac{r}{b}\right) = \exp\left(-\frac{r^2}{\lambda b^2}\right) \tag{2.15}$$

where λ, of order 1, differs slightly depending on the quantity represented by j.

Chen and Rodi [17] point out that the buoyancy flux and momentum flux are constant (and therefore equal to the initial values) only if the ambient density ρ_a is constant throughout. When this is the case, the integral conservation equations 2.10 to 2.13 can be solved readily to give analytical solutions for the mean flow quantities. However, in a stratified environment, where ρ_a is not constant by definition, the above governing equations need to be solved numerically as an initial value problem.

2.2.4 Plume trapping

In a stratified environment, what is also observed is trapping, where the plume fluid, while constantly entraining the surrounding fluid and diluting, reaches a vertical extent where it become neutrally buoyant with respect to its surroundings. The plume fluid, having gained momentum from its buoyancy, will travel a little beyond the neutral buoyancy point, in what is known as the momentum offshoot. At this point, the plume fluid no longer travels along the axial direction, but will start to intrude horizontally and spread at the neutrally buoyant height. Turner [62], using dimensional analysis and empirical observations, predicts the trapping height h_t in terms of the initial buoyancy flux at the source and the buoyancy frequency of the ambient:

$$h_t = 2.8 \left(\frac{B}{N^3}\right)^{1/4} \tag{2.16}$$

The plume behavior at the intrusion implies three things, all of which are equivalent: governing equations with the boundary layer approximation no longer hold; the flow is no longer self similar in the axial direction; the entrainment coefficient is not constant, and indeed breaks down when the plume no longer moves forward. Other methods of solution are to be sought, e.g. (i) direct numerical simulation (as done by Sato et al. [50]), which is typically computationally expensive; (ii) by dimensional analysis; and (iii) by returning to the differential equations relaxing several assumptions.

2.3 Double Phase Plumes

Double phase or multiphase plumes are buoyant flows where the source of buoyancy is of a different phase than the ambient fluid. Figure 2-2 is a schematic comparing the single phase plume to a multiphase plume. Thus the flow is divided between the dispersed phase (the initial source of buoyancy) and the continuous phase (formed by the ambient fluid).

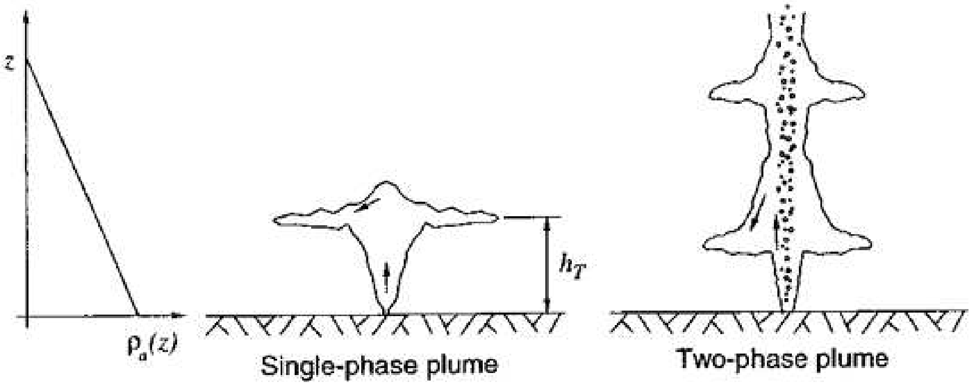

Figure 2-2: Single and bubble plumes in stratification

Examples of double phase plumes are bubble plumes, studied intensively for purposes of reservoir destratification (Lemckert and Imberger [38], Asaeda and Imberger [7], McDougall [41]). Other examples include oil droplet plumes and sediment laden plumes, in which the dispersed phase is oil and solid particles respectively. These examples and other multiphase plumes have been described in Chapter 1.

In these multiphase plumes, the governing equations are similar to that of a single phase plume, except that both phases need now to be accounted for - the plume water and the dispersed phase.

The plume fluid flux, Q_p, is expressed as

$$Q_p(z) = \int_0^\infty 2\pi r(1 - C(r,z))dr \tag{2.17}$$

where C is the particle volume fraction. The dispersed phase typically will travel faster than the plume fluid by a slip velocity u_s, such that the mean transport velocity of the bubbles is $u_b = u + u_s$ (Kobus [36], McDougall [41]). The dispersed phase flux, Q_b, is thus

$$Q_b(z) = \int_0^\infty 2\pi r C(r,z)(u(r,z) + u_s(r_z))dr \tag{2.18}$$

The total kinematic momentum flux is the sum of the momentum fluxes of the two phases:

$$M(z) = \gamma \int_0^\infty 2\pi r[u^2(r,z)(1-C(r,z)) + \frac{\rho_b}{\rho_w}(u(r,z)+u_s(r,z))^2 C(r,z)]dr \tag{2.19}$$

where γ is a momentum amplification factor introduced by Milgram [42] that takes into account the additional momentum transport due to turbulent fluctuations from the mean velocity, u, used for the determination of M for multiphase plumes.

The total kinematic buoyancy flux B of a buoyant release of dispersed phase and continuous phase, in which both phases are buoyant with respect to the local ambient is

$$\begin{aligned} B(z) &= B_p(z) + B_b(z) \\ &= \int_0^\infty 2\pi r[(1-C(r,z))g\frac{\Delta\rho_w(z)}{\rho_w}u(r,z)]dr \\ &+ \int_0^\infty 2\pi r[C(r,z)g\frac{\Delta\rho_b(z)}{\rho_w}(u(r,z)+u_s(r,z))]dr \end{aligned} \tag{2.20}$$

The integral conservation equations for plumes are used, Equations 2.10, 2.11 and 2.12, with the fluxes defined for the multiphase plume Equations 2.17, 2.18 2.19 and 2.20.

McDougall [41] normalized the governing equations above with the depth of the water body, since this was a length scale at which bubble expansion played a significant role in reservoir destratification. Socolofsky and Adams [55] used the characteristic plume length scale $l_c = (B/N^3)^{1/4}$.

Though Equation 2.20 suggests that the buoyancy of the dispersed phase and the continuous dense phase are linearly additive, there may be interaction between the two buoyant phases, like the momentum amplification factor for Milgram [42] for momentum. The clear interaction between the three fluxes of buoyancy, momentum and mass does not exist for the multiphase plume. The dispersed phase interfaces will create additional shear within the interstitial fluid. Additional processes such as the volume expansion of bubbles during its rise, are detailed by McDougall [41], and may also affect the overall plume dynamics.

Accordingly, the similarity solution does not necessarily hold true for the double phase plume, though this is still often assumed in the literature. Like for a single phase plume, the velocity, bubble void fraction and concentration profiles are modeled as a Gaussian profile of the two separate phases (Kobus [36], Milgram [42], McDougall [41]). Thus Equation 2.15 is used, with different constant values of λ used for each of the two phases, to yield similarity solutions. This assumption is supported by experimental observations of bubble plumes in unstratified environments (Kobus [36]), and also in gas bubble jets in various liquid/gas systems (Tacke et al. [60]).

The plume release has also been modeled as a double plume, made up of an inner core, containing the dispersed phase, with outer plume region that is free of bubbles or droplets (McDougall [41], Asaeda and Imberger [7], and Crounse [20]).

2.3.1 Peeling

In a stratified environment for multiphase plumes, what is also observed is peeling. This occurs because the dispersed phase particles or droplets, being unable to mix locally with the entrained fluid, will always remain buoyant, while the continuous phase is able to dilute and often reverse buoyancy. The result is that the plume fluid ‘peels’ and leaves the dispersed phase at a level near its neutral buoyancy. The depth or height at which this occurs is called the peeling depth or height.

As shown in Section 2.3.2, Socolofsky [53] predicts the fraction of fluid that leaves the plume core in the first peeling event, as a function of initial plume release conditions. For the plumes studied by the current work, the predicted fraction that peels is close to one.

2.3.2 Plume Structure

Since regions of the plume where peeling and trapping occurs have appreciable width, the original boundary layer approximations (Equation 2.2), and their associated similarity solutions , are no longer applicable. However, the practical aim is not to know the mean velocities at every point, but to be able to predict the extent of plume rise or fall, trapping level, and resulting dilutions. For this one could study the general plume behavior empirically.

Overall plume structure have been investigated by previous authors, mainly pertaining to optimizing reservoir destratification. Asaeda and Imberger [7] classified plumes as exhibiting three distinct behaviors, or types, as shown in Figure 2-3.

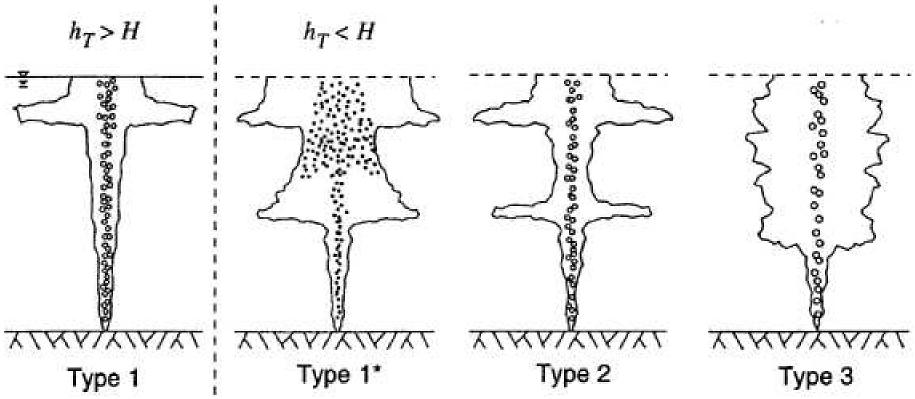

Figure 2-3: Stagnant multiphase plume structure types (after Socolofsky [52]). The plumes depicted are positively buoyant.

Type 1 plumes have no intermediate intrusion layers, except when they impinge on a surface. Type 2 plumes have one or more distinct intrusions, and Type 3 plumes show continuous peeling from the plume core, resulting in a random set of intrusions. Experiments by Socolofsky and Adams [55] also identified a new type, Type 1*, which differs from Type 2 in that the bubbles are also carried into the intrusion layers temporarily.

Socolofsky and Adams [55] introduced a parameter, the non-dimensional slip velocity U_N, that relates the observed plume type with only the plume source and ambient conditions. U_N is defined by

$$U_N = \frac{u_s}{(BN)^{1/4}} \tag{2.21}$$

where u_s is the slip velocity of the dispersed phase droplets or particles, B the initial kinematic buoyancy flux, and N the Brunt-Väisälä frequency, or stratification frequency of the ambient. The denominator, $(BN)^{1/4}$, is a characteristic plume fluid velocity. It is found by that Type 1* plume behavior is observed for $U_N < 1.4$, Type 2 for $1.4 < U_N < 2.4$, and Type 3 for $U_N > 2.4$.

It is also possible to relate the trap and peel levels using the new parameter U_N. Using experiments by Asaeda and Imberger [7], Lemckert and Imberger [38], Socolofsky and Adams [55] and Reingold [48], all shown in Figure 2-4, the following equations were used as fitting curves.

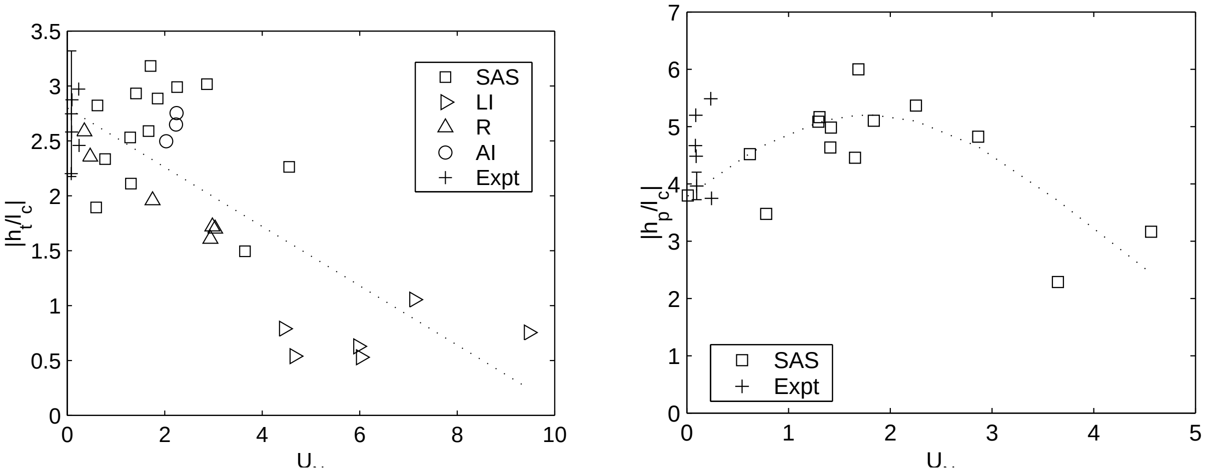

Non-dimensional trap depth

Non-dimensional peel depth

Figure 2-4: Plot of experimental trap and peel depths against U_N. The current work's experimental data points have been inverted for comparison with bubble plumes. Key: SAS = Socolofsky [52]; LI = Lemckert and Imberger [38]; R = Reingold [48]; AI = Asaeda and Imberger [7]; Expt = Current Experiments (with typical error bar shown).

Prediction of trap height h_t as a function of U_N:

$$h_t = (2.8 - 0.27U_N)\left(\frac{B}{N^3}\right)^{1/4} \tag{2.22}$$

Peeling height h_p as a function of U_N:

$$h_p = 5.2\exp\left(-\frac{(U_N - 1.8)^2}{10.1}\right)\left(\frac{B}{N^3}\right)^{1/4} \tag{2.23}$$

In Equations 2.22 and 2.23, the dimensional group $(B/N^3)^{1/4}$, was also shown by Socolofsky and Adams [55] as a characteristic plume length scale. For $U_N = 0$, the trap and peel height predictions yield those found for single phase plumes as reported in Fischer et al. [26] and Turner [62].

Another plume property of interest is the intrusion layer volume flux Q_i, as this is the measure for intrusion layer dilution. This was investigated experimentally by Lemckert and Imberger [38] for step stratification, Yeh [69] for plumes with crossflow, and also by Socolofsky [53] for linear stratification. Though it was shown that Q_i is a decreasing function of U_N, in general,

$$Q_i = c\left(\frac{B^3}{N^5}\right)^{\frac{1}{4}} \tag{2.24}$$

Experiments showed typical values of c as 0.4 to 0.8. For a single phase plume, according to Fischer et al. [26], $c = 0.9$.

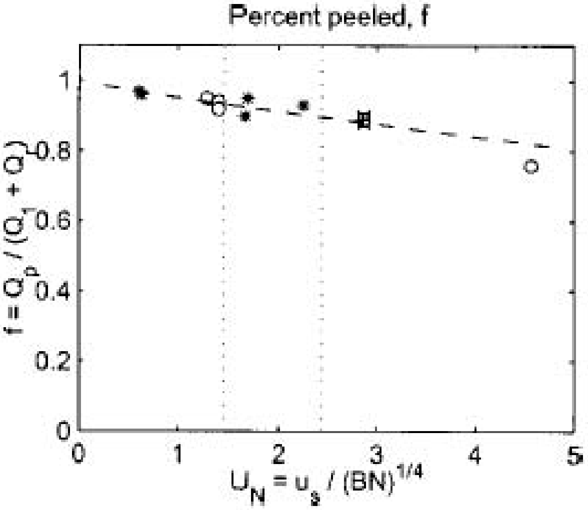

Figure 2-5: First plume fluid peeling fraction plotted against U_N . Circles represent air bubble experiments; stars represent glass-bead experiments (from Scott and Adams [54].

In the current work, it is expected that the observed plume type will be Type 1*, as $U_N << 1$. Though Socolofsky and Adams [54] show a decreasing function of peeling fraction with U_N (shown in Figure 2-5), for plumes of Type 1* and 2, the fraction is experimentally close to one. For this work this means that nearly all of the plume fluid will leave the plume at the first peeling event. In particular, for plumes of Type 1*, this means that the particles, will be advected by the plume fluid even as it completely intrudes outwards at the first peeling event.

2.4 Physical Modeling Scenarios in Literature

A number of conditions for multiphase plumes have been studied experimentally, as categorized in this section.

Stratification

Leitch and Baines [37], Baines and Leitch [10], Asaeda and Imberger [7] and Chen and Cardoso [18] have studied bubble plumes in step stratification, which is most relevant to lake destratification, where a step stratification exists.

On the other hand, to allow the buoyancy frequency N to be constant in the ambient, many bubble plume studies were conducted in linear density environments (McDougall [41], Baines and Leitch [10], Asaeda and Imberger [7], Milgram [42], Socolofsky and Adams [55]).

Crossflow

Axisymmetry is assumed in quiescent situations, as well as in weak crossflow, where the horizontal current is not sufficiently strong to overly deflect the plume. Fischer [26] details the effects of a crossflow on single phase jets and plumes, and provides length scales which can be used to predict momentum or crossflow dominance of the release. Pun and Davidson, 1999 investigated the separation of tracer due to crossflow on a buoyant plume, and predicted the height at which transition to a strongly advected, flow occurs. Yeh [69] studied the buoyant detrainment of plumes with crossflow and the effects of crossflow current on the radial spread of an intrusion layer, and made predictions based on the initial plume and crossflow conditions.

Socolofsky and Adams [53] extended this study to bubble plumes in crossflow. Here separation may also occur, in which the intrusion layer will be deflected by the current sooner than it would passively leave due to buoyant trapping (See Figure 2-6). A prediction for the height at which separation occurs was made based on experimental measurements. Like for the single phase buoyant plume in strong crossflow, the flow cannot be treated as self similar.

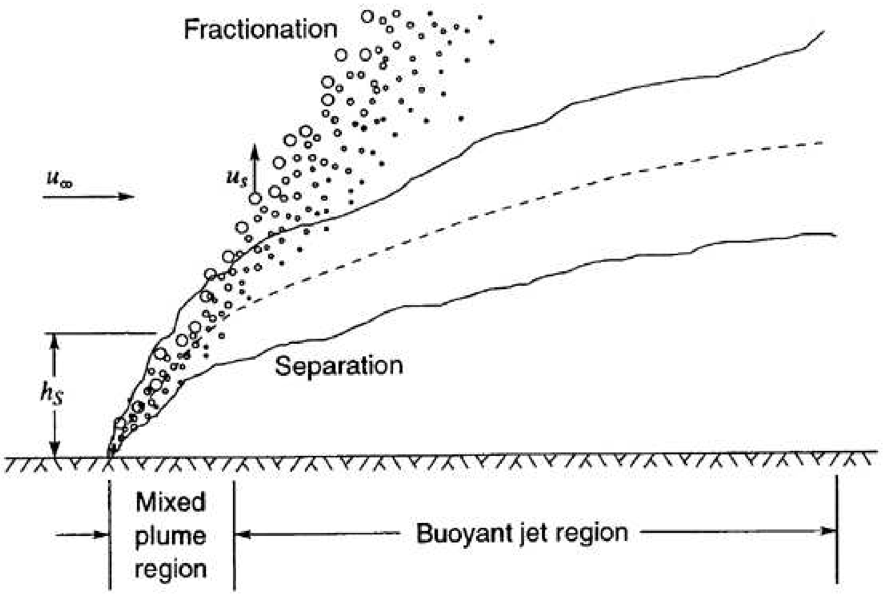

Figure 2-6: Effect of crossflow current on bubble plume (after Socolofsky [52])

Particle Laden Plumes in Stratification

Carey et al. [14], Sparks et al. [59], Zarrebini and Cardoso [70] and Cardoso and Zarrebini [13] have studied particle-laden plumes in experimental conditions, where particle laden plumes are released across density stratified environments. In these studies, the plume continuous phase was positively buoyant, but contained negatively buoyant particles. The particles used were fine particles that were readily advected by the surrounding fluid, suggesting that $U_N << 1$ in the flow, albeit locally (as a step stratified environment was chosen). In the case of Zarrebini and Cardoso [70], the particles, while sinking back to the bottom (and the location of the plume source), were entrained towards the rising plume. As a result, the sediment that was collected showed a distribution with zero sediment towards the center source region.

Distributed plume

The theories developed by Morton et al. [44], Chen and Rodi [17], and McDougall [41], all take the source of the plume to be a point of no initial area. In practice, though there is always a finite source area, most plume behaviors are observed far from the source, where the diameter of the source will no longer be important. However, there is a class of so-called lazy plumes, or distributed plumes, in which the source diameter is significant. In these plumes, there is a momentum deficit in the source, compared to the buoyancy and mass flux. The single-phase versions of these have been studied by Hunt and Kaye [33]. They have also been applied to plumes which mix with the ambient to cause non-monotonic changes in density (Caulfield and Woods [15]).

Large Scale Plumes

Woods and Bush [67] have studied plumes in rotational flows in stratification in the laboratory. Large scale equivalents are termed Megaplumes, where they are on a scale where the Coriolis force will act to shear the resulting plumes and create other concentration and density gradients. They have been applied to hydrothermal plume behavior, since they can be tens of kilometers in diameter. Since CO_2 hydrate releases in the ocean, if implemented, will be of comparable scale, the effect of rotation, combined with ambient crossflows that move the plume fluid, may therefore be an important factor in determining their dynamics.

2.5 Carbon Dioxide Hydrates

As outlined in Section 1.1, there is ongoing study of carbon dioxide hydrates as a possible vehicle for deeper carbon sequestration (Warzinski et al. [65], Holder et al. [31]). Figure 2-7 show the dependence of CO_2 phase on pressure and temperature.

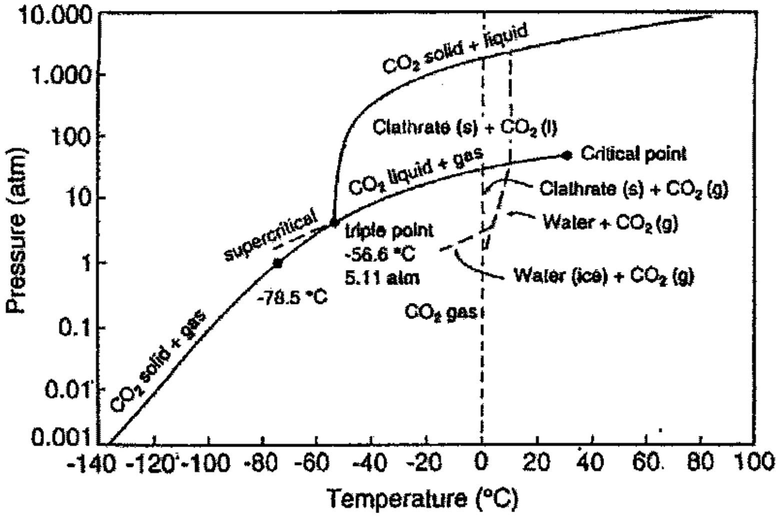

Figure 2-7: Phase Diagram for CO_2 with water (After Murray et al. [45])

CO_2 hydrates will also dissolve in the ambient seawater upon its descent. There are two main reasons that the dissolution behavior requires study. Aqueous CO_2 will exist in various charged forms in water according to these main reactions, known in aquatic chemistry as the carbonate system (Morel and Hering [43]):

$$CO_2(aq) + H_2O \rightleftharpoons H_2CO_3(aq) \tag{2.25}$$

$$H_2CO_3(aq) \rightleftharpoons H^+ + HCO_3^- \tag{2.26}$$

$$HCO_3^- \rightleftharpoons H^+ + CO_3^{2-} \tag{2.27}$$

The result of this is that increasing dissolved CO_2 will shift the equilibria above to the right, and lower the local pH of the ambient seawater, which is expected to affect passive marine organisms. (Alendal and Drange [5]). Understanding the dissolution dynamics will enable better prediction on the eventual pH drop caused by the release of hydrate particles into the ocean.

The dissolution of CO_2 will also increase the density of the seawater, according to the solute density effect. For a binary aqueous solution, based on thermodynamic theory, the density can be expressed as (Söhnel, O. and Novotný [56])

$$\rho(T, P, c) = \rho_w(T, P) + [M_2 - \rho_w(T, P)V_\phi(T, P)]c \tag{2.28}$$

where $\rho_w(T, P)$ is the density of pure water, M_2 the molecular weight of the solute (here for CO_2 $M_2 = 44$ g/mol) and V_ϕ the apparent molar volume of dissolved solute. The value of V_ϕ is often determined experimentally and fitted as a function of temperature (Garcia [27]). Pressure dependence of V_ϕ for CO_2-water systems only comes into play above about 300 degrees Celsius. The increased density due to the presence of dissolved CO_2 can be an advantage to sequestration, since the plume becomes one in which there are two negatively buoyant sources: the original hydrate particles, and the dense CO_2 rich seawater immediately surrounding the particles.

As the particle dissolves, their size is expected to decrease. This has also been studied in the context of lake aeration (Wüest et al. [68]), where oxygen is the dissolving material. A model for the dissolution of the mass of a single bubble m_b of radius r_b would take the following form:

$$\frac{dm_b}{dt} = -4\pi r_b K \rho_b (C_s - C_\infty) \tag{2.29}$$

where C_s is the solubility, the concentration very close to the surface of the particle, C_∞ the dispersed phase solute, and K a mass transfer coefficient.

Since the value of U_N is dependent on the slip velocity of the particle u_s, which in turn is diameter-based, the large scale plume characteristics described in Section 2.3.2 will change with droplet diameter. On the small scale, it is also expected that particle shrinkage, CO_2 dissolution, and solute density effect will be three additional feedbacks to the dynamics of turbulent bubble plume motion, and thus need to be incorporated into a plume dynamics model.

2.6 Focus of Current Work

The previous section presented different combinations of experimental conditions. The current experiments will focus on stable linear stratification with no crossflow current. The dispersed phase will be negatively buoyant, and the continuous phase will also be negatively buoyant with respect to the ambient. This is to model the behavior of a release of carbon dioxide hydrate particles, where part of the dispersed phase has dissolved into the continuous phase, and has increased its density. The plume trap and peel depths, and the dispersed phase radial spread will be observed for Type 1* plumes, varying the dispersed phase to dense continuous phase ratio.

2.6.1 Observations

In the current experiments, the carbon dioxide hydrates and the dense, CO_2-enriched seawater are modeled by dense beads and brine respectively.

The typical values of U_N of the plume releases of the current experiments are from 0.08 to 0.14. They are expected to have Type 1* plume behavior, whereby the dispersed phase are advected with the intruding fluid. For fine particles in the plume, since the particles act as if they are also plume fluid up until the peel region, there is no double plume structure (inner and outer). Indeed, the particles make their way out into the outer plume, and form part of the intrusion layer, for a certain time until their negative buoyancy again dominates their individual motion.

Socolofsky [54] relates the peeling fraction, the fraction of the original fluid that leaves the dispersed phase upon the first peeling event, and found experimentally that even at high values of $U_N \sim 4$, about 80% of the original plume fluid will enter the intrusion (see Figurech2:peel-frac). At lower U_N values, this fraction is higher, and at $U_N \sim 0$, it is expected to be equal to unity (as is the observation in a single-phase plume, which completely traps at the intrusion height).

One of the observations from the experiments is the effect of varying buoyancy source on the trap and peeling depths for the plume. This has been noted by Sparks et al. [57] and Hogg et al. [30], in the context of sediment-laden gravity currents, which are observed to 'lift-off' the floor after depositing sediment. Since the particles are fine, and are readily incorporated into the intrusion layer, they also can be viewed as imparting additional density to the bulk intrusion layer, similar to the solute density effect due to suspension.

In a similar way, as the sediment particles fall out of the intrusion fluid, the bulk fluid may experience an overall decrease in density. In the physical situation of the current experiments, this would mean that the intrusion layer will become slightly positively buoyant after sediment fall out, and will begin to rise, entraining ambient fluid on its way up to its new neutrally buoyant level. Therefore, it is expected, and is observed in the current experiments, that the higher the presence of fine particles in the intrusion layer (as a result of having a higher initial buoyancy due to particles, and not fluid), the smaller the final observed trapping depth.

It is also predicted that the plume fluid, carrying the fine particles along as a dispersed phase, will almost completely enter the first intrusion layer, and that no particles will sink along the plume centerline, in the usual Type 2 plume behavior.

2.6.2 Prediction of Sediment Spread

Here two methods of prediction are offered for the radial spread of fine particles due to outward advection by the plume intrusion layer. Both are based on estimation of the settling particles' residence time within the intrusion layer. This is applicable to fine particles or droplets, which are readily advected by the plume fluid, i.e. the U_N value of the steady plume release is much less than one.

Consider the intrusion layer of a Type 1* plume, as shown in Figure 2-8. The plume fluid, upon vertically overshooting the neutrally buoyant level, has transferred its turbulent kinetic energy back to buoyant potential energy. While the vertical momentum of the plume will drop to zero at the peel height, locally there is a lateral density gradient, which translates to a pressure gradient, and this results in lateral intrusion. Cardoso and Woods [12] suggest that, since the intrusions have a sharp leading edge, and a smooth outer appearance compared to the plume itself, there is lower turbulence in the intrusion layer. In addition, continuity and axisymmetry dictates an intrusion layer to form. As the intrusion layer spreads radially outward, the sediment particles will begin to settle out of the intrusion layer by their own weight.

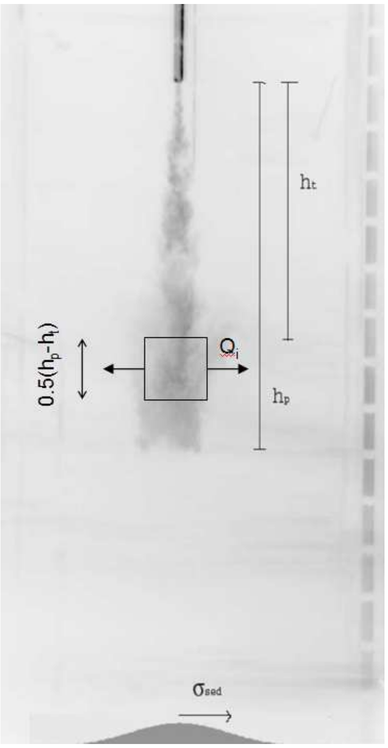

Figure 2-8: A schematic of intrusion layer and sediment deposition, with estimates of length scales.

As Figure 2-8 shows, several length scales of the plume and the intrusion fluxes can be used to predict final particle spread. Let the particles fall at their slip velocity u_s through the intrusion layer. The thickness of the intrusion layer Δh, is assumed constant. Thus in an axisymmetric intrusion (as is expected in the vertical plume with minimal crossflow), with the above assumption the intrusion is modeled as a cylinder whose radius increases with time. It is assumed (and also shown in experimental observations) that particles leaving the intrusion layer will fall passively to the bottom of the tank. This means that the radial spread within the intrusion layer, and thus the residence time of particles whilst in the layer, will determine the bottom sediment radial spread.

Constant particle flux model

If the flow of the intrusion is treated as a radially spreading plug flow, then Figure 2-9 shows the characteristic particle trajectory through a slice of the intrusion layer.

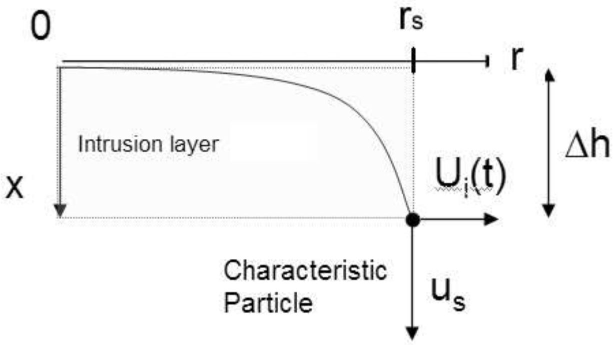

Figure 2-9: Schematic of characteristic particle trajectory through plume intrusion layer.

This typical particle is expected to move laterally with the intrusion fluid, while falling at its slip velocity. All the particles in this model thus start at the center of the intrusion layer, $r = 0$ (this assumption is tested later in the section). The time taken for the this to fall out of the intrusion layer is given by:

$$t_b = \frac{\Delta h}{u_s} \tag{2.30}$$

Another assumption here is that the intrusion layer has a uniform thickness Δh. At the time t_b, the following is true for the intrusion fluid:

$$Q_i t_b = \pi r_s^2 \Delta h \tag{2.31}$$

where r_s is the lateral spread radius of the characteristic particle, and Q_i the intrusion flux. This assumes that the intrusion layer is spreading out in a radial plug flow from the center.

Combining Equations 2.30 and 2.31, the assumed thickness of the intrusion layer Δh cancels out, yielding:

$$r_s = \sqrt{\frac{Q_i}{\pi u_s}} \tag{2.32}$$

Using the estimate of the intrusion flux Q_i [54], Equation 2.24, a characteristic radial particle spread is given by

$$r_s = \sqrt{\frac{c}{\pi}} \left(\frac{B^3}{N^5}\right)^{1/8} \frac{1}{u_s^{1/2}} \tag{2.33}$$

where $c = 0.9$ is the constant of proportionality, determined for single phase plumes (and the limit of multiphase plumes as $U_N \rightarrow 0$) by Fischer et al. [26].

The particle in Figure 2-9 also starts its descent at the top of the intrusion layer. It can be conceived that this particle will be the one to travel the farthest radially, and that the rest of the particles that start in the middle of the layer, will fall out of the layer sooner than this particle. In a model where the sediment acts as a downward plug flow with a constant sediment flux, the value of r_s would be the expected maximum radial extent of the particle settling. Less than this radius, the concentration of particles is expected to be constant.

Well Mixed Model

If the particles are well mixed in the intrusion layer, the governing equation for the concentration of sediment in the layer C is given by

$$\frac{dC}{dt} = -\frac{u_s}{\Delta h}C \tag{2.34}$$

yielding the time evolution of concentration of sediment in the intrusion layer:

$$C = C_0 \exp\left(-\frac{u_s}{\Delta h}t\right) \tag{2.35}$$

where C_0 is the mean concentration of sediment entering the intrusion layer. As in Equation 2.31 for the plug flow model, the time can be translated into the radial distance by

$$Q_i t = \pi r^2 \Delta h \tag{2.36}$$

Substituting the expression for t from Equation 2.36 into Equation 2.35 gives

$$\begin{aligned} C &= C_0 \exp\left(-\frac{r^2 \pi u_s}{Qi}\right) \\ &= C_0 \exp\left(-\frac{r^2}{\sigma_r^2}\right) \end{aligned} \tag{2.37}$$

where

$$\sigma_r = \sqrt{\frac{Q_i}{\pi u_s}} \tag{2.38}$$

Q_i is again obtained using Equation 2.24 from Socolofsky and Adams [54], yielding

$$\sigma_r = \sqrt{\frac{c}{\pi}}\frac{B^{3/8}}{N^{5/8}U_s^{1/2}} \tag{2.39}$$

Note that $\sigma_r = r_s$, and Equation 2.37 describes a radial Gaussian distribution for the sediment concentration below the intrusion layer.

Figure 2-10 summarizes the predictions of the two models of sedimentation for fine sediment out of the plume intrusion layer.

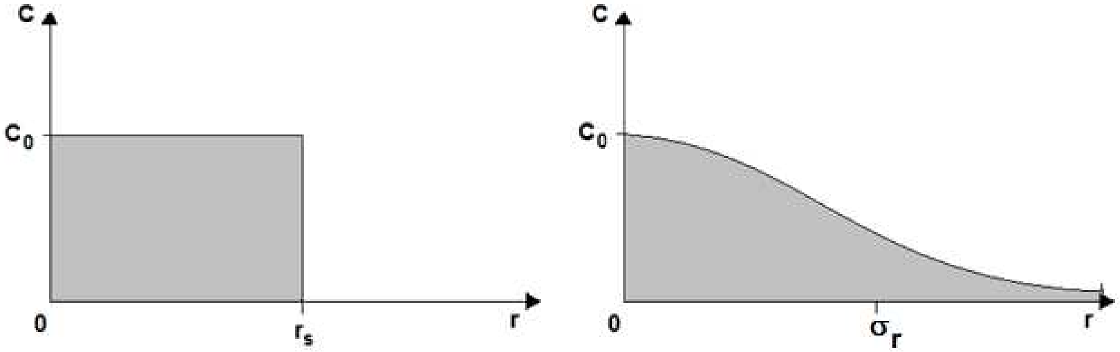

(a) (b)

Figure 2-10: Sedimentation models out of plume intrusion layer: (a) Constant particle flux model, resulting in a constant concentration of sediment at radii less than r_s; (b) Well mixed model, yielding a Gaussian radial profile with standard deviation σ_r.

Intrusion layer-sediment interaction

In order to determine whether the sediment will be well mixed within the intrusion layer, or will follow the particle trajectory model, it is useful to define a Peclet number for the sediment:

$$Pe = \frac{u_s \Delta h}{E_z} \tag{2.40}$$

where u_s is the slip velocity of the sediment, Δh the intrusion layer thickness, and E_z a vertical turbulent diffusivity, often characterized as

$$E_z = c_1 u_* / \Delta h \tag{2.41}$$

where u_* is the shear velocity, and c_1 a proportionality constant which is often empirically determined from different flow situations. Substituting Equation 2.41 into Equation 2.40 gives

$$Pe = \frac{u_s}{cu_*} \tag{2.42}$$

Therefore in this system, the Peclet number is equivalent to the sediment Rouse number $R \sim u_s/u_*$. This is reasonable, since the Rouse number is a measure of the propensity for the sediment to remain suspended, while the Peclet number in this case describes how vertical diffusion of sediment will keep the sediment well mixed within the intrusion layer. Furthermore, it is possible to relate the shear velocity u_* to the characteristic velocity of the plume intrusion, i.e. $u_* = c_2(BN)^{1/4}$ where $c_2 \sim 0.05$ for many turbulent flows.

Since the smaller the value of the Peclet number, the more well mixed the system, Equation 2.46 suggests that for small values of U_N, the intrusion layer will be well mixed with respect to the sediment, and the Gaussian sediment radial distribution well mixed model would be observed. Conversely, for plumes characterized by high U_N, the high Peclet or Rouse number indicates that the sediment will not be affected by the intrusion velocity and simply fall through the intrusion.

Dhamotharan et al. [22] studied numerically the effect of the Peclet number on the unsteady deposition rates of sediment in a one-dimensional, sedimentation column. They present the time evolution of vertical sediment concentration for Peclet numbers ranging from zero to infinity, and suggest that the transition between sedimentation from vertically homogeneous mixed reservoir to simple settling occurs in the range of Pe from 0.2 to about 20, for sediment that is initially uniformly distributed.

Furthermore, one can relate the shear velocity u_* to the characteristic velocity of the plume intrusion. Typically the shear velocity is taken to be proportional to a characteristic velocity of the flow, i.e. $u_* = c_2U$. Here the characteristic velocity is taken as the intrusion layer horizontal velocity, $U_i(r)$ is obtained in terms of the intrusion flux:

$$
\begin{aligned}
U_i(r) &= \frac{Q_i}{2\pi r \Delta h} \\
&= \frac{(B^3/N^5)^{1/4}}{2\pi r \Delta h} \qquad (2.43)
\end{aligned}
$$

Note that the intrusion velocity decreases with radius (or time elapsed from the origin). The intrusion layer thickness can be estimated by half the difference of the trap and peel depths $\Delta h = (h_p - h_t)/2$. The factor of $\frac{1}{2}$ is taken based on observations that suggest that the plume, after peeling or reaching its maximum depth, rebounds about halfway before intruding outwards. The maximum velocity can be calculated by taking $r = \alpha h_t$, the plume width at the trap level, and using Equation 2.24 for the intrusion flux:

$$U_{i,max} = \frac{(B^3/N^5)^{1/4}}{\pi \alpha h_t (h_p - h_t)} \qquad (2.44)$$

using Equations 2.23 and Equation 2.22 for low values of U_N, the resulting expression for $U_{i,max}$ is

$$
\begin{aligned}
U_{i,max} &= \frac{(B^3/N^5)^{1/4}}{2\pi\alpha 2.8 (B/N)^{1/4} (B/N)^{1/4}/2} \\
&= \frac{1}{2.8\pi\alpha}(BN)^{1/4} \qquad (2.45)
\end{aligned}
$$

The intrusion velocity, and thus u_*, is proportional to the characteristic plume velocity. The Peclet (or Rouse) number can thus be rewritten as

$$Pe = \frac{u_s}{\frac{c_1 c_2}{2.8\pi\alpha}(BN)^{1/4}} = \frac{U_N}{c'} \qquad (2.46)$$

where $c' = \frac{c_1 c_2}{2.8\pi\alpha}$ = constant. Since the smaller the value of the Peclet number, the more well mixed the system, Equation 2.46 suggests that for small values of U_N, the intrusion layer will be well mixed with respect to the sediment, and the Gaussian sediment radial distribution well mixed model would be observed. Conversely, for plumes characterized by high U_N, the high Peclet or Rouse number indicates that the sediment will not be affected by the intrusion velocity and simply fall through the intrusion.

For the current work, typical U_N values range between 0.08 to 0.14. A typical Reynolds number for the intrusion, $Re = u\Delta h/\nu$, can be calculated: taking $U = (BN)^4$=0.05 m/s, $\Delta h = 0.15m$ and kinematic viscosity $\nu = 10^{-6}\text{m}^2/\text{s}$, $Re = 7500$. Taking typical values of $c_1 = 0.07$, for open channel turbulent flow, and $c_2 = 0.05$ for bottom shear, the resulting Peclet numbers are in the range of 20 to 40. Also, note that since the characteristic velocity of the intrusion decays with a 1/r dependence, the Peclet number defined by this formulation will increase linearly with radial distance.

It is reasonable to model all of the sediment as beginning their trajectories from the center, $r = 0$, even though the sediment laden plume already has a finite width at the intrusion depth. To test this, the ratio is taken of the width of the plume at the trapping depth $b(h_t)$ observed and the intrusion layer lateral width of interest, σ_r. The current experiments showed that

$$\frac{b(h_t)}{\sigma_r} \sim \frac{1}{8} \tag{2.47}$$

which is small, and supports the assumption.

Finally, Sparks et al. [59] and Zarrebini and Cardoso [70] also predict the radial distribution of sediment. The particles used in their experimental study are also fine enough to be readily advected by the surrounding fluid (i.e. $U_N << 1$ for the current work). However, since a step stratification was used, the definition of U_N must be applied to a smaller, local density gradient. Although their plumes had a positively buoyant continuous phase, they observe a Gaussian distribution of sediment within their intrusion layer at the step stratification height, and this was previously shown also by Carey et al. [14] for different elevations across the plume. Thus, if the intrusion layer is well mixed, the observed particle spread is also expected to have a radial Gaussian profile, with radial standard deviation σ_r, as described by Equation 2.37.

Chapter 3

Experimental Set-Up

This chapter briefly describes the apparatus and methods used for the experiments described in this thesis. A majority of the equipment was designed, built and used by Socolofsky [52] and Ruggaber [49] for their work on plume dynamics, in stagnant stratification. While this chapter describes some of the adaptations to the current experiments, please refer to Socolofsky [52] for a more thorough description of the following which were employed in the same way:

- The tall experimental tank
- Two-tank stratification method
- Density profiler, consisting of a belt driven linear positioner and an Ocean Sensors Conductivity and Temperature (CT) probe, connected to a computer interface
- Flow illumination using an Argon laser sheet across the central slice of the plume
- Image acquisition system using a CCD camera and framegrabber interface to computer

3.1 Experimental Tank

The main apparatus for the experiments is the tall experimental tank at Parsons Lab at MIT, built specifically for housing a salinity-stratified environment. It measures 1.22 m square by 2.44 m tall and was built by Excalibur Glassworks, Inc. of Woburn, Massachusetts in June 1997. It is made of 38mm thick, two-ply, fully tempered laminated glass.

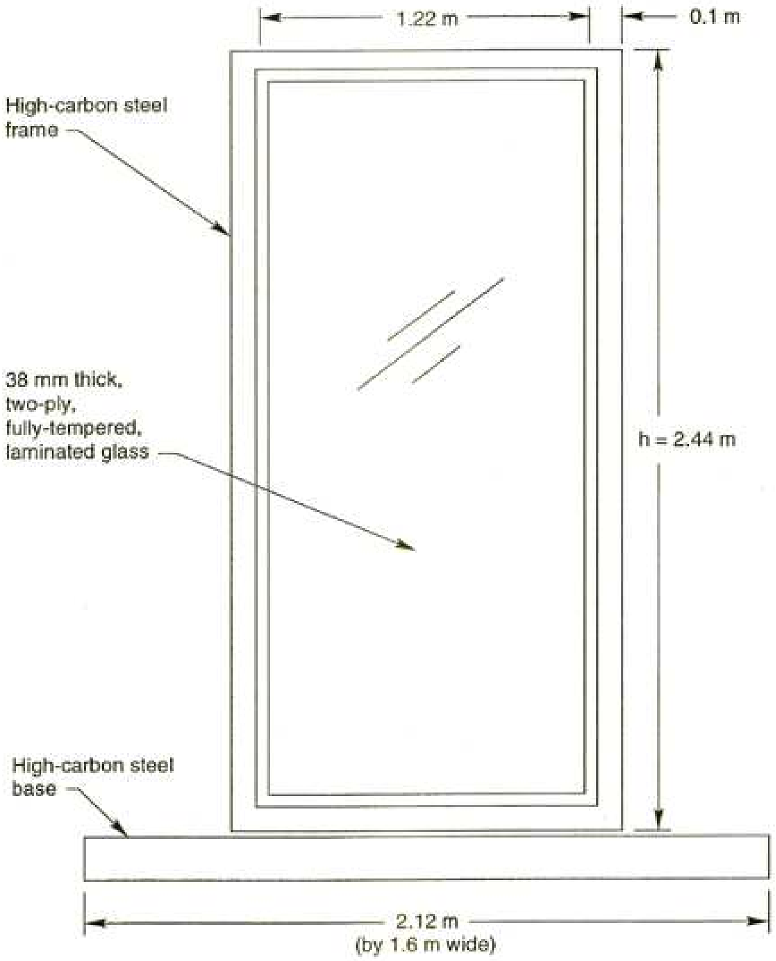

Figure 3-1: Elevation of experimental tank (from Socolofsky [52])

The first peel height of a typical bubble flow used by Socolofsky [52] in the design of the tank was about 1.2 m above the release point, well within the maximum depth of 2.4 m. While Socolofsky also wanted to observe at least two discrete, Type 2 peels, the current experiments were negatively buoyant, characterized by $U_N << 1$, and expected to exhibit only one visible peel and intrusion layer. Peel depths predicted for the experiments were less than 1 m. As a result, the depth of the tank was more than sufficient to observe the peeling and trapping depths of the negatively buoyant plumes. In addition, the remainder of the depth was traversed by the sediment particles which fell out of the intrusion layer after radial spread, and their post-peel behavior was able to be observed.

After a period of time the plume intrusion layer began to contact the tank walls. If the volume of the intrusion layer V_i when contacting the tank is modeled as a cylinder with the same diameter as the tank width w, and with a uniform thickness of half the difference of trap and peel height, i.e.,

$$V_i = \frac{1}{2}(h_p - h_t)\frac{1}{4}\pi w^2 \tag{3.1}$$

then an estimated time for contact to occur could be given by dividing a predicted intrusion layer volume, V_i by an estimate of the intrusion flux, Q_i based on plume and stratification conditions (Equation 2.24 from Socolofsky [52]):

$$t \sim \frac{V_i}{Q_i} = \frac{\frac{1}{2}(h_p - h_t)\pi(w/2)^2}{0.9(B^3/N^5)^{1/4}} \tag{3.2}$$

where $w = 1.2$m. The predicted times for the different experimental runs were about four times greater than the planned duration of the experiments. In the experiments conducted with fine sediment spreading radially, less than 1% of the sediment typically made its way out to the furthest collecting trays (distance from center about 60 cm, or the half width of the tank). The plume peeled from the center of the tank, and so was unaffected by the sides. Also, the plume intrusions, away from the plume centerline, were observed to travel horizontally in the tank for the duration of the experiment, so the trap depth should not be affected by the side walls. From these observations, the width of the tank was sufficient for the current experiments to model a laterally infinite domain.

3.2 Stratification

The predictions of trap height, peel height, U_N and sediment spread all depend on N, the Brunt-Väisälä frequency, which in turn depends on the vertical density gradient of the ambient. A linear density gradient over the region of the plume is desired to obtain a constant value for N.

3.2.1 Two-Tank Method

The tank was stratified using the two-tank method, which is capable of producing any arbitrary salt density stratification profile, including linear. Refer to the schematic of the two-tank method in Figure 3-2. The second tank in the method's naming refers to the well stirred mixing tank for preparing the local salt concentration (and thus density) for pumping into the main experimental tank. Initially, the mixing tank had a density equal to the maximum desired for the final density profile in the experimental tank. As the latter was filled from the top, freshwater was added to the mixing tank, the rate of which determined the rate of decrease in density. Also, a perforated splash plate made of plastic, the size of the cross-section of the tank, topped with horsehair and supported by styrofoam floaters, was used to divert the incoming salt water sideways, thus minimizing vertical mixing of the lower density layers by the incoming water.

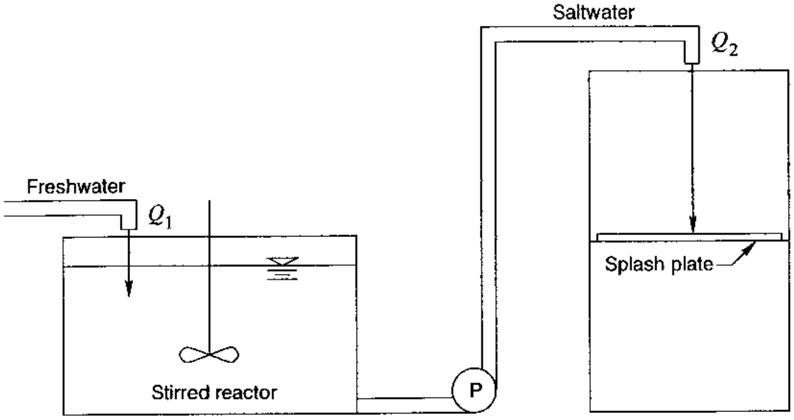

Figure 3-2: Schematic of the two-tank stratification method (from Socolofsky [52])

For a mixing tank which is well mixed, with initial volume V_0 and salt concentration C_0, receiving freshwater at a rate Q_1 and delivering saltwater to the experimental tank at a rate Q_2, the change of salt concentration over time in the water received by the latter $C(t)$, is given by

$$\frac{C(t)}{C_0} = \left(\frac{V_0 - (Q_2 - Q_1)t}{V_0}\right)^{\frac{Q_1}{Q_2 - Q_1}} \tag{3.3}$$

Thus for a linear profile, the exponent needs to be 1, requiring $Q_2 = 2Q_1$. Also to have $C = 0$ at the top of the tank, V_0 needs to be half the volume of the experimental tank.

For the current experiments, the freshwater was fed via a 3.8 cm (1.5 in) local water supply into a tank measuring 3 m by 1.5 m by 1 m deep. The tank had one of its sides replaced with glass such that the water level was constantly visible and the desired initial tank water level can be marked. To make up the initial salt solution, 68 kg (150 lb) of salt (Cargill food grade sodium chloride) was placed into the mixing tank, and freshwater wasadded to the initial water level, to make up a solution of about 1020 kg/m^3. During the stratification process, the freshwater was fed by a firehose into a line diffuser aligned in the center of the bottom of the tank, to encourage mixing. Also at the bottom of the tank was a drain which connects to the experimental tank. A corrosion-resistant centrifugal pump (Teel model number 4RJ44), connected to the mixing tank drain, delivered the salt solution to the experimental tank. In order to prevent air bubbles from entering the pump, the mixing tank was not allowed to completely empty out: instead the initial volume was such that by the end of the stratification process, the mixing tank retained about 10 cm of water depth. One consequence of not emptying the tank was that, if the water flow rates in and out of the tank were kept constant, the surface of the tank did not achieve zero salinity. But since the experimental predictions and observations only require a smooth density gradient, and since the source for the experiments conducted were placed at least 10 cm below the surface, the absolute density at the top of the tank was not important.

The flow of the freshwater and saltwater lines were monitored by passing both lines through identical rotometers, each with a scale of 0.4 to 3.6 l/s (6 to 60 gpm). Ball valves were also placed in the line for manual adjustment of the two flows until the saltwater flow was twice the freshwater flow. While the freshwater flow could be increased to the maximum rotometer reading, the pump delivered a maximum saltwater flow of 2.2 l/s (35 gpm). In the experiments, typical freshwater (Q_1) and saltwater (Q_2) flows were 0.5 and 1.0 l/s (8 and 16 gpm) respectively.

3.2.2 Measurement of Density Gradient

The density profile of the stratified tank was measured using an Ocean Sensors OS300 Conductivity, Temperature and Depth (CTD) probe. The OS300 CT probe consisted of a plastic housing for its internal electronics, which was connected via cable to an computer I/O card, and the probes for conductivity and depth. The probe was custom made such that the two probes were not also in the housing, but connected via long waterproof cables to the main unit. This was so that the CT probe could be connected to the belt-driven linear positioner.

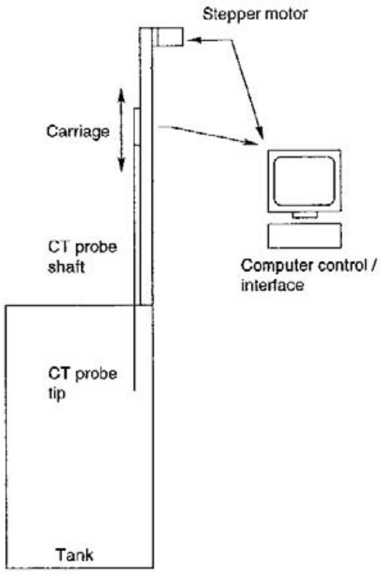

Figure 3-3: Schematic of the density profiler.

The belt-driven linear positoner (Schematic in Figure 3-3) was a Parker HLE 60 Series, single axis, linear actuator supplied by Empire Automation of Woburn, Massachusetts (Part number `HLE060RB.NL.E.2712.DA0000.MBL.SP7.GAW03.H1.ZA.LH1`). It was controlled by a separate stepper motor and encoder (Parker Zeta 6104-83-93), which in turn can output its position to and can be moved by a Windows NT computer via serial port. The linear actuator was necessary since the pressure transducer on the Ocean Sensors probe responded slower than the temperature and conductivity probe, and could not be relied on to obtain synchronized readings. Using the above equipment, the OS300 probe mounted to the linear actuator carriage was able to output temperature and conductivity readings at a known depth in the tank. As every 25,000 motor steps on the actuator corresponded to the vertical carriage distance of 160 mm, the distance traveled by the density probe from the starting point of the density profile, was known theoretically to the nearest 6.4×10^{-6} m. In practice, the determination of the location of the surface, from which all encoder positions are determined, introduced inaccuracies. This was reduced by filling the tank to the same level for each experiment.

During a density profile measurement, a `LabVIEW` program was run that moved the probe to the water surface of the tank, and initialized the linear actuator via the Zeta 6104 control box. Another `LabVIEW` program then signalled the carriage to move down at a constant speed and at rapid regular time intervals collected the encoder position (which translates to depth below surface), and the temperature and conductivity from the OS300 probe. At the bottom of the profiled depth, the above data was written to a text file on the computer, and the computer issued another command for the carriage to return to its initial position. The density was computed from the temperature and conductivity measurement with an equation of state (Equation 3.4)

Finally, The Windows NT software Motion Architect, included with the Zeta 6104 package, was also used for purposes of testing the speed of the carriage, and to determine the number of steps required for a density profile.

3.2.3 Density Profile in Experiments

The Ocean Sensors OS300 CT probe used for the density profile outputted temperature and salinity values at a given vertical position along the linear track (Refer to Figure 3-3). The local density ρ_w (in kg/m^3) was calculated from the probe output using the following equation of state, used for seawater (McCutcheon et al. [40]). Although the experiment used pure water, and salinity due to NaCl alone, this equation of state is able to predict the density of the resulting brine, as NaCl is a major salt in seawater.

$$\rho = 1000\left(1 - \frac{(T + 288.9414)}{508929.2(T + 68.12963)}(T - 3.9863)^2\right) + AS + BS^{1.5} + CS^2 \quad (3.4)$$

where T is the temperature in degrees C, S the salinity in g/kg, and

$$\begin{aligned} A &= 0.824493 - 0.0040899T + 0.000076438T^2 - 0.00000082467T^3 \\ &\quad +0.0000000053675T^4 \\ B &= -0.005724 + 0.00010227T - 0.0000016546T^2 \\ C &= 0.00048314 \end{aligned}$$

Figure 3-4 shows a typical density profile used in the experiments. Figure 3-5 depicts the resulting local buoyancy frequency N from the profile, and an average value used for numerical prediction. The profiles used were typically slightly non-linear, with smaller average density gradients near the top of the tank. They also showed strong local density gradients due to noise. The non-linear profile may be attributed to the saltwater and freshwater flowrates not being precisely in a 2:1 ratio throughout the stratification process, and to the turbulent disturbances at the top while the splash plate was removed from the tank. Because of these factors, a moving average was computed for the data, and the resulting profile shown superimposed in figure 3-4. However, since the plume release was at least 19 cm below the surface, and since the peeling and trapping of the plume occured at the top half of the tank, the line plotted in figure 3-4 shows that in the region of interest in the tank, the density gradient was near linear.

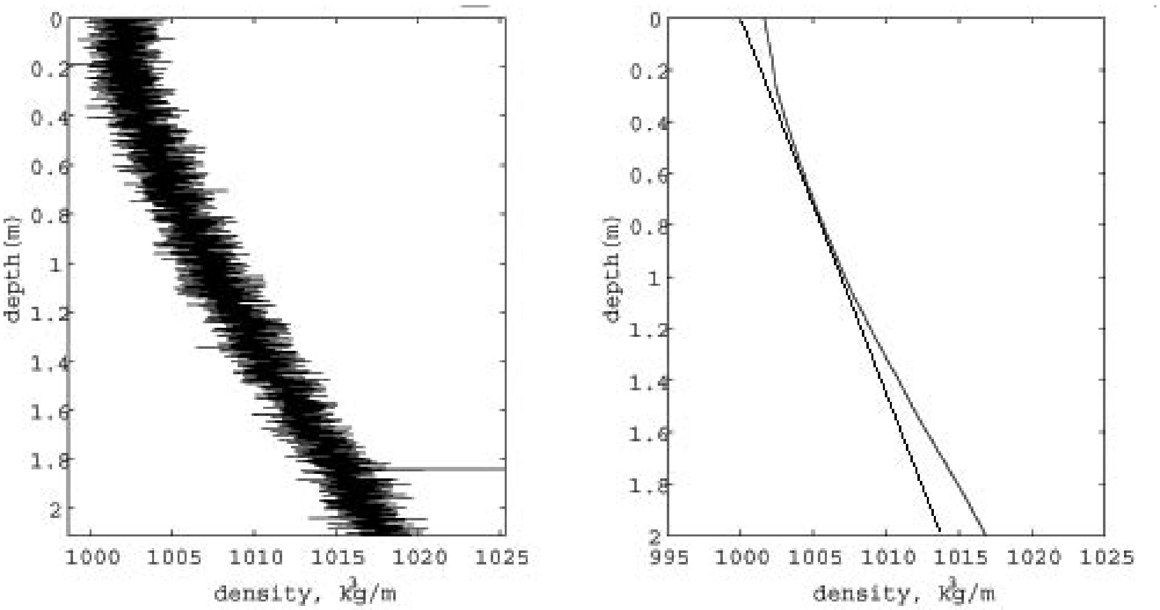

Figure 3-4: An example of a density profile (Experiment 042203). Left: raw density profile. Right: moving average profile, with straight line plotted next to the region of interest.

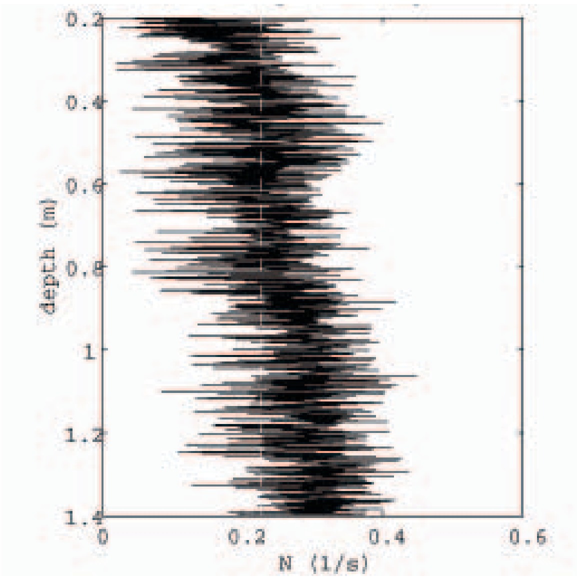

Figure 3-5: Plot of computed Buoyancy (Brunt Väisälä frequency N, with depth (Experiment 042203). Average value used was 0.24 s^{-1}

3.3 Buoyancy Sources

The driving force for the motion of the multiphase plume is its initial buoyancy flux, B. In the current work, this buoyancy is a sum of the buoyancy of particles, B_b, and the initial buoyancy flux of the brine introduced into the ambient B_s. Thus the definition of initial buoyancy used is:

$$B = B_b + B_s = Q_b g \frac{\rho_b - \rho_0}{\rho_0} + Q_s g \frac{\rho_s - \rho_0}{\rho_0} \tag{3.5}$$

3.3.1 Particles

The non-dimensional slip velocity $U_N = \frac{u_s}{(BN)^{1/4}}$, where B is the initial buoyancy flux, is highly dependent on the size and the density of the particles used, if the particles make up the buoyancy. This parameter in turn dictates many of the plume's shape (number of discrete peels and plume type) and characteristics such as the trap and peel depth (as predicted by Equations 2.23 and 2.23 respectively).

Most work on multiphase plumes have been using air bubbles as the dispersed phase. Very fine hydrogen bubbles can be created by the electrolysis of water, as has been done by Chen and Cardoso [18] to create a bubble plume, following Creighton and Koehler [19]. Reingold [48] stipulated that negatively buoyant particles can be used to model an inverted air bubble plume, with the added advantage that the particle size distribution, and thus U_N, is more easily controlled, and is unaffected by such factors as compressibility ambient salinity. Air bubbles will expand upon ascent, following the Ideal Gas Law. The presence of ions in solution such as salt, will buffer the electrostatic repulsion between water molecules, enabling them to exist on a surface with higher curvature. Therefore it is expected that in saltwater, air bubbles can be smaller. While the current experiments were mainly used to model sinking carbon dioxide hydrates, for which solid particles were suitable, the physically modeled scenario may also be inverted to include oil droplets and volcanic ash, as mentioned in Section 1.4.

The current work focused on U_N values of much less than 1. This was achieved by either having many particles (high B), or having very small slip velocities (low u_s). The selection of particles was also important to create a plume with a reasonably large peel and trap depth below the release point, but which also showed Type 1* behavior, where the particles would be significantly affected by the intrusion peeling layer.

Two types of materials were chosen, glass and polystyrene. The glass beads were Ballotini impact glass beads (From Potters Industries), used for finishing smooth metal surfaces in industry. Several size classes provided by the vendor were used, AE and AH. These were the smallest sized glass beads, which decreases their slip velocity, and thus U_N. Polystyrene beads were also used, since they had a smaller density (1050 kg/m^3), thus decreasing their slip velocity given the same buoyancy flux as for glass. This means that even smaller values of U_N were achieved with the polystyrene beads.

Particle Size Distribution

The size distributions of the particles used for the experiments was determined using sieve analysis. For each sieve analysis a known mass of beads was passed through a series of progressively finer mesh sieves (sieve j), which allowed particles of diameter d_j through d_{j+1} to be collected separately on individual sieves.

After about 20 minutes of shaking through the sieves, the beads left on each sieve m_j were weighed. Each weight fraction was determined by $\frac{m_j}{\sum_j m_j}$, and the diameter of the particles in the fraction was taken as the mean of d_j and d_{j-1}.

Figure 3-6 shows the sieve analysis results for the different size classes and materials of spherical particles used in the experiments. Note that for each individual experimental run, the particles used had the size distribution shown in one of these figures. Also based on these figures, the mean and standard deviation of the three particle types were determined.

For a few experiments the beads from only one sieve mesh size were used, namely for AH glass beads that were left on the 88 micron sieve. This was done to reduce the standard deviation of the particle sample. Since the particles in this sieve were

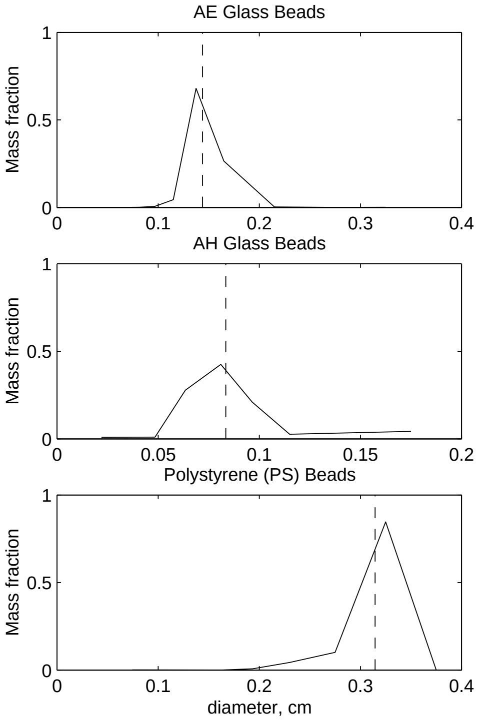

Figure 3-6: Sieve analysis mass fractions for particles used

between 88 and 105 microns in diameter, the mean was taken to be the mean of the two sieve mesh sizes $d = 97$ microns, and the standard deviation taken as 5 microns.

Determination of Slip Velocity

From the sieve analysis diameters, Dietrich [23] provides an empirical relation to obtain the slip velocity, based on a spherical particle:

$$\begin{aligned} log(W_s^*) &= -3.76715 + 1.92944(log(D^*)) - 0.09815(log(D^*))^2 \\ &\quad -0.00575(log(D^*))^3 + 0.00056(log(D^*))^4 \qquad (3.6) \end{aligned}$$

where the non-dimensional diameter and terminal velocity are given by

$$\begin{aligned} D^* &= \frac{(s-1)gd^3}{\nu^2} \\ W^* &= \frac{u_s^3}{(s-1)g\nu} \end{aligned}$$

where s is the local specific gravity at the release point and ν the kinematic viscosity of the ambient fluid.

Table 3.3.1 shows the resulting particle sizes and slip velocity distribution (for ambient of 1000 kg/m^3).

Table 3.1: Particle characteristics

	Density	Slip Velocity (cm/s)		Particle Size (μm)	
	(kg/m^3)	Mean	Std. dev.	Mean	Std. dev.
AE Glass	2450	1.2	0.2	145	16
AH Glass	2450	0.5	0.2	84	24
AH Glass 88	2450	0.6	0.05	97	5?
Polystyrene	1050	0.2	0.03	315	27

Brine

The buoyant releases in most of the current experiments required that a part of the total buoyancy be made up of negatively buoyant continuous phase fluid, to approximately model the effect that dissolved carbon dioxide has on the vicinity of CO_2 hydrate particles. This was done by mixing a brine solution in the 6 gallon carboy used for its delivery described in section 3.3.2. First, the salinity and temperature at the depth of the plume release in the tank was obtained by averaging the recorded salinities within ±1 cm of that depth from the salinity profile performed for the tank. Having determined the value of ρ_0, the mass of salt to create the desired brine density ρ_s and buoyancy flux $B = \frac{\rho_s - \rho_0}{\rho} g Q_0$, was calculated by solving for S in Equation 3.4.

3.3.2 Release methods

Depending on the material of the particles used, two different methods of release of the combined particles and brine were used.

Glass Release

Figure 3-7 shows a schematic of the glass particle release method. Glass beads were released from a 1 liter plastic bottle by gravity. Different flow rates were achieved by attaching different standard-sized funnels onto the opening of the bottle. A vibrator powered by a 3V DC transformer was also placed at the top of the bottle, to facilitate steady bead flow, which was confirmed by timing the funnels' output onto an analytical balance. The funnel rested on a PVC pipe setup, that spanned across the top of the tank as shown in Figure 3-7, and that acted as a conduit for the brine at the top of the tank. The conduit was placed close to the water surface to minimize the initial momentum of the fluid as it discharged into to the experimental tank. As the brine traveled through the conduit, the particles were added inline to the flow just prior to the point where the combined flow was diverted downwards into the source release point. Air bubbles that might enter the line, since the opening and the inline mixing area are exposed to the atmosphere, were minimized by keeping the conduit running full. This was achieved by placing a small piece of horsehair or a sponge in the line near the entry funnel of the brine. This semi-permeable sponge also served to reduce the momentum of the discharging fluid into the experimental tank.

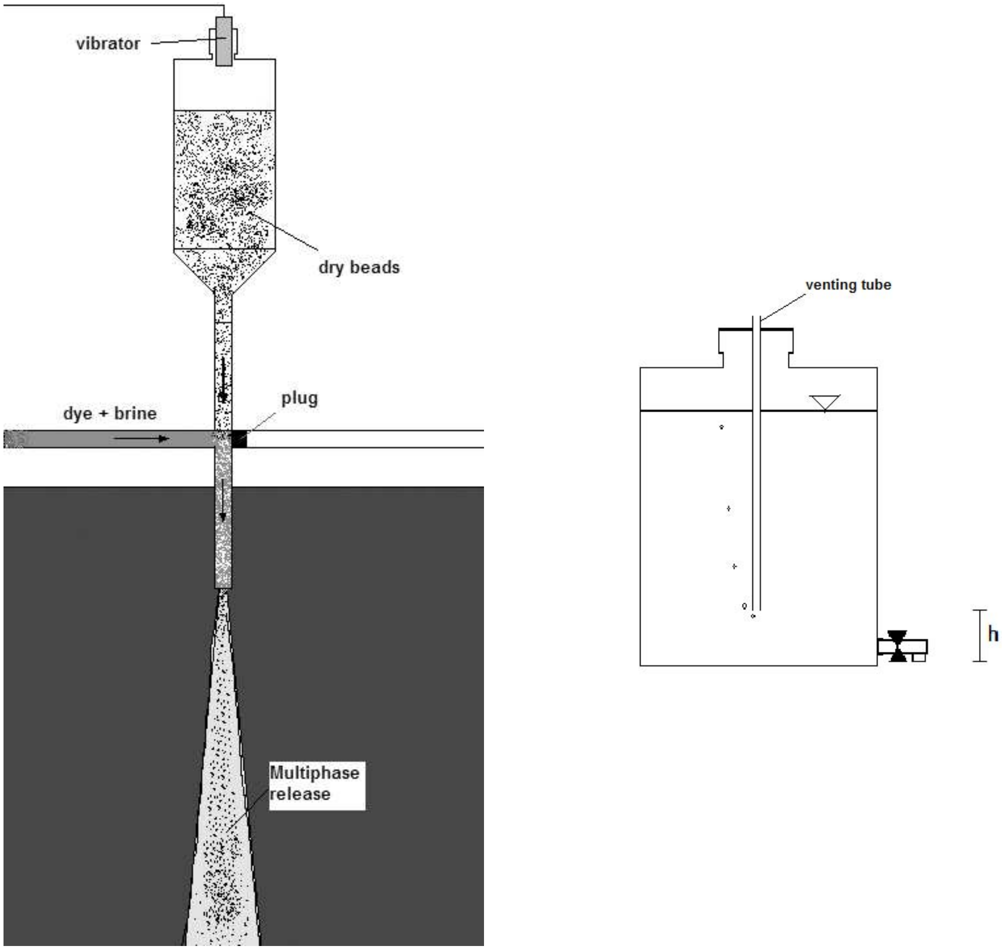

(a) (b)

Figure 3-7: (a) Set-up for glass particle mixed plume release. (b) Mariotte siphon used to deliver continuous plume phase (brine) for all experiments.

In order to deliver a steady flow of brine, a (6 gal) carboy was modified to become a large Mariotte siphon (Figure 3-7), mentioned in Fischer et al. [26]. A tube which opened to the atmosphere out of the top, but penetrated underneath the surface of the water in the delivery carboy, kept the discharging water at a constant pressure head, corresponding to the elevation of the the bottom of the tube. As the bottle emptied, a partial vacuum was created in the cavity between the top of the bottle and the water level, which served to keep the pressure head constant, as long as the bottom of the tube remained submerged.

Polystyrene Release

Figure 3-8 shows the method of buoyancy source release used for polystyrene beads.

These plastic particles tended to become electrostatically charged when flowing past each other, and hence either float on the water or coagulate if released alone into the water. In order to reduce this effect, a surfactant (window cleaner) was added to the solution to decrease the charge effect, and enable the particles to be thoroughly wetted by the water. To further improve wetting of individual beads, the reservoir of polystyrene beads was submerged for the experiment run.

For both the brine and the polystyrene beads to be released from the same orifice (for a more homogeneous plume composition), the brine delivered via the Mariotte siphon technique illustrated earlier, and in Figure 3-7, was passed into the particle delivering bottle via a flexible tube. The end of the tube opened as a manifold near the neck of the interior of the delivery bottle. This had the effect of mixing the local particles with brine of the desired density for the initial buoyant release.

To keep the flow of the mixed flow constant, the brine in the delivery bottle was kept at a constant head above the water. This was required, since for releases of beads through the smaller delivery bottle orifices, the fluid tended to accumulate in the delivery bottle, creating an extra pressure head.

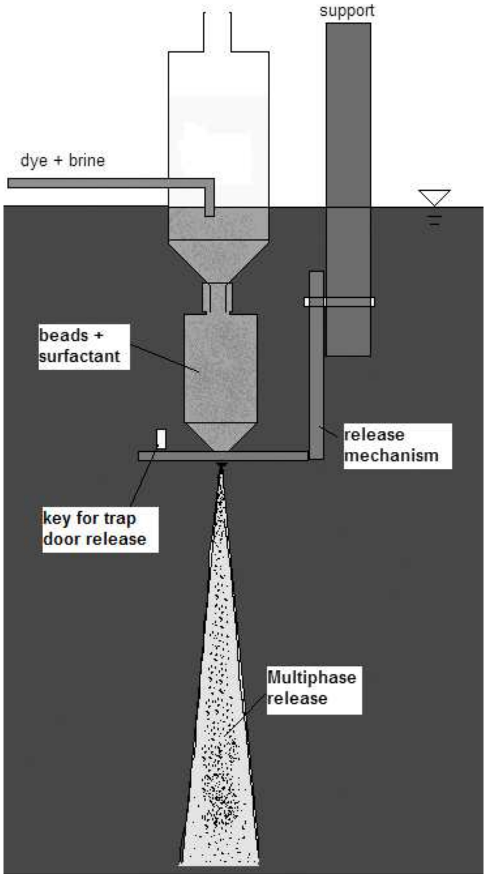

Figure 3-8: Set-up for the release of polystyrene/brine plume..

3.3.3 Initial Flow and Momentum

In a pure plume, the initial momentum and volume flow rate of the plume fluid is zero, but in practice experimental releases introduced some momentum and initial volume flux. The initial volume flux of the plume was given by the sum of the flow rates of brine and particles at the discharge, $Q = Q_s + Q_b$. The mean kinematic momentum flux of the particles (subscript b for beads) and brine (subscript s for saltwater) flow through an orifice of diameter d, into ambient density ρ_0, is described by

$$\rho_0 M = \rho_b M_b + \rho_s M_s = \rho_b Q_b u_b + \rho_s Q_s u_{saltwater} \tag{3.7}$$

where

$$\begin{aligned} u_b &= u_{saltwater} + u_s && (3.8) \\ u_{saltwater} &= \frac{Q_s}{a_s} && (3.9) \end{aligned}$$

where a_s is the area area of the cross section occupied by the continuous phase, and u_s the particle slip velocity. The above expression for M uses the form of Equation 2.19 with momentum amplification of one, which takes into account the extra momentum contribution of the settling velocity and density of the particle phase. If the value of a_s is taken as the volume fraction of brine multiplied by the total orifice area, $a = \pi d^2/4$, i.e.

$$a_s = \frac{Q_s}{Q_b + Q_s} a = \frac{Q_s}{Q_b + Q_s} \frac{\pi d^2}{4} \tag{3.10}$$

Equation 3.7 becomes

$$M = \frac{\rho_b}{\rho_0} Q_b \left(\frac{Q_b + Q_s}{\pi d^2/4} + u_s \right) + \frac{\rho_s}{\rho_0} Q_s \left(\frac{Q_b + Q_s}{\pi d^2/4} \right) \tag{3.11}$$

Characteristic length scales

In order to determine whether the initial momentum and flow rate of the experiments were large enough to affect the peel and trap depths, several characteristic plume length scales were defined by dimensional analysis. This method was used by Fischer et al. [26] to define different regimes within a buoyant flow, and is applied here for the initial plume conditions.

The volume length scale, l_q, is defined as the length scale where the magnitude of the volume flux Q, and the buoyancy flux B of the plume are comparable. (This is different from the length scale l_Q defined by Fischer et al. [26], which compares the volume flux with plume momentum). Dimensional analysis yields the length scale l_q as

$$l_q = \frac{Q^{3/5}}{B^{1/5}} \tag{3.12}$$

Below the value of l_q, the flow is still affected by the initial flow rate, or the port orifice conditions (such as the diameter used for the discharge). The momentum length scale l_m, is the length scale where the momentum flux M is about the same magnitude as the buoyancy flux, or where momentum still affects the flow. Using dimensional analysis,

$$l_m = \frac{M^{3/4}}{B^{1/2}} \tag{3.13}$$

Finally, the stratification plume length scale l_c, used earlier by Socolofsky [52] in defining the plume trap and peel depths, is a length scale describing the ratio of the magnitudes of the buoyancy to the strength of the ambient stratification, characterized by the buoyancy frequency, N.

$$l_c = \frac{B^{1/4}}{N^{3/4}} \tag{3.14}$$

It has been shown by Morton et al. [44] and Fischer et al. [26] that the trap and peel depth are a function of the stratification length scale, l_c. Here the value of l_c is pitted against the momentum length scale and the volume length scale as a measure of their relative importance. This gives two ratios:

$$\frac{l_m}{l_c} = \left(\frac{MN}{B}\right)^{3/4} \tag{3.15}$$

$$\frac{l_q}{l_c} = \left(\frac{Q^{1/5}N^{1/4}}{B^{3/20}}\right)^{3} \tag{3.16}$$

Normalizing the ratios such that the power of B is unity, yields the two characteristic ratios, the momentum and volume flux numbers.

Momentum number:

$$N_m = \left(\frac{MN}{B}\right) \tag{3.17}$$

Volume number:

$$N_q = \left(\frac{Q^{4/3}N^{5/3}}{B}\right) \tag{3.18}$$

Fischer et al. [26] used the value of $N = N_m^2$ to determine whether a buoyant release should be considered a pure jet or a pure plume: with $N_m^2 >> 1$ the plume can be considered a pure jet, and $N_m^2 << 1$ a pure plume. The value of N_m could thus be used to define the significance of initial momentum on the plume. Also, N_q will equivalently reflect the significance of the initial flow rate or port geometry on the plume length scales. The above ratios will be used as criteria for accepting or rejecting experimental runs based on their initial momentum or initial volume fluxes. Note that for the pure plume case, both N_m and N_q will approach zero, since initial momentum and volume fluxes are negligible.

3.3.4 Determination of Flow Rates

Using the glass delivery method, the two flows of brine and glass particles could be measured separately. The volume flow rate of the brine out of the carboy was measured by timing a known volume of dispensed brine. The mass flow of the glass beads was also timed, and was converted via its density to a volumetric flow rate.

With the polystyrene submerged combined delivery method, it was necessary to time the duration of each experiment, and measure the start and finish water levels in the carboy to obtain the liquid flow rate. As for the polystyrene particles, while a known mass of beads (600 g) was placed inside the delivery bottle at the beginning of each experiment, in order to time the average flow rate out of the bottle, any mass of beads left over in the bottle at the end of the experiment was dried overnight under a heat lamp and fan, and weighed on an analytical scale. Dividing the mass change of beads in the bottle by the duration of the experiment gives an average flow rate for the experimental run.

3.4 Peel Height

In order to aid visualization of the plume structure, Laser-Induced fluorescence (LIF) was used. The laser source was a 6-Watt Argon-ion LASER (Model Innova 70 by Coherent, Inc.). The laser was passed through fiber optic, the end of which was a rectangular slit, which generated an approximately 2 cm thick laser light sheet through the glass walls of the experimental tank. The sheet was then aligned so that it illuminated a longitudinal slice along the centerline of the plume.

Rhodamine WT dye was chosen for visualization of the plume fluid. because it was well illuminated by the laser, and the concentrations in the water were able to be determined by a fluorometer. In a plume release, both the dispersed phase and the dye were well illuminated by the laser. Since $U_N << 1$, i.e. the particle slip velocity was small compared to the intrusion velocity, the particles will travel with the intrusion and, at least initially, also act as a tracer for the plume fluid similar to the dye.

As the experiment progressed the particles began to drop out of the intrusion layer, and somewhat obscure the peeling event. However, by viewing the recorded images, it was still possible to discern the height at which the particles were reversing direction as they were advected by the intrusion fluid.

3.5 Trap Height

Vertical fluorescence profiles of a dye tracer were performed on the tank to obtain the trap depth of the plume fluid. A Rhodamine WT fluorometer, by Seapoint Sensors, Inc., of Exeter, New Hampshire, gave fluorescence readings. The fluorometer was connected to the Ocean Sensors, Inc., OS200 conductivity temperature and depth (CTD) probe, which was used as an interfacing device for the fluorometer to the computer, and also to provide depth readings. A fluorometer profile was run from the top to the bottom of the tank for up to 5 different lateral positions in the tank for one experimental run.

Rhodamine WT was used since the excitation wavelength of 540 nm matched that of the Seapoint Sensors fluorometer. Since the dye was used as a visual tracer to locate the trap height and peel height the absolute dye concentration was only important to ensure that the fluorometer was able to detect it in the fluorometer profile. Figure 3-9 shows the calibration curve of voltage reading to concentration of Rhodamine WT. There was a linear relationship in log-log space between the concentration of the dye and the voltage sensed by the fluorometer.

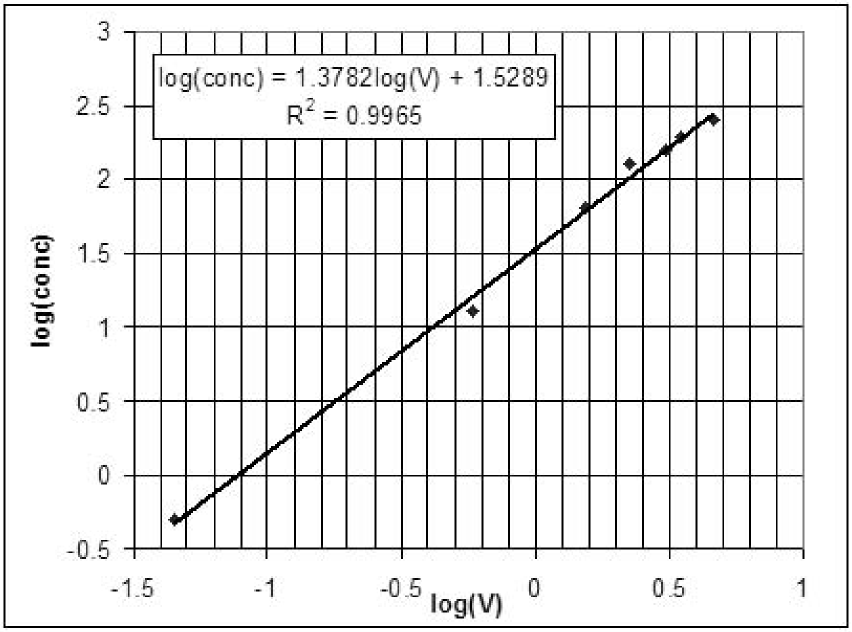

Figure 3-9: Calibration curve for Seapoint Sensors fluorometer.

The depth measurement for the fluorometer profiles were taken directly from the OS200 CTD probe. Since the computer interfacing program combined the fluorometer and the CTD outputs in one file, the fluorescence voltage output and the depth readings were synchronized at 7 readings per second. This depth measurement was different from the one obtained from the density profile by the OS300 CTD probe and linear track, since the linear track could not support the weight of the fluorometer and the interfacing device (the OS200 probe). The dye measurements could not be taken *in situ* of the experiment, since raising and lowering of the CT probe and fluorometer (with a combined frontal area of $57cm^2$) was enough to generate internal waves and extraneous turbulence, disturbing both the plume intrusions and the quiescent settling of the particles to the bottom. Thus the fluorometer profile was only performed about half an hour after the particles have settled on the collection trays, and the dye was allowed to mix horizontally across constant density levels. As illustrated in the fluorometer run results in the Appendix, which were done in different horizontal positions in the tank, the dye profiles were essentially uniform.

3.6 Particle Spread

The radial spread of the sediment advected by the plume, was measured by collecting the particles from beneath the peel event, in a series of 144 collecting trays measuring 3.0 cm by 5.0 cm by 3.0 cm deep.

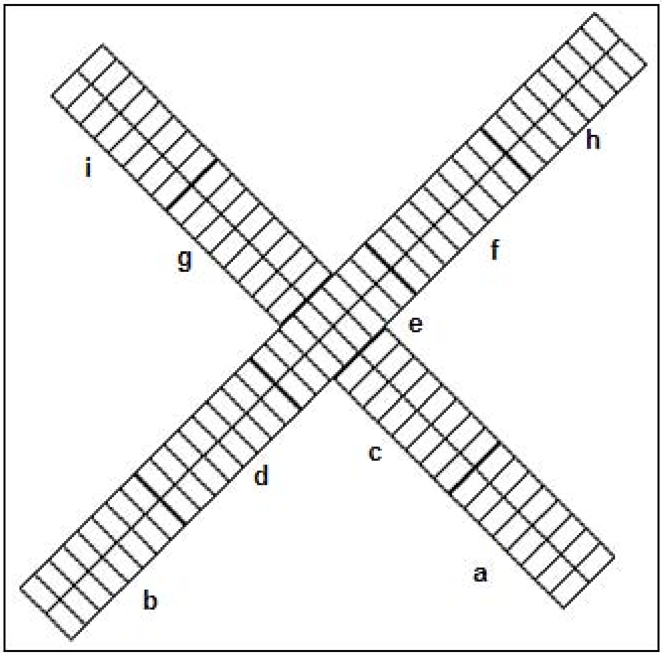

Figure 3-10: Set-up of particle collection trays. Each cell measures 3.0 cm × 5.0 cm × 3.0 cm.

Figure 3-10 shows the horizontal arrangement of the collection trays used. They were nine identical ice cube trays arranged in a diagonal cross, centered in the tank, and attached to a rigid plate which could be raised and lowered by pulley in the tank. This particular configuration was chosen so that a two dimensional distribution could be calculated, even without the center of the sediment distribution landing right on the center of the cross structure, either because the plume direction was not directed quite vertically, or if any circulation was created to translate the entire sediment distribution horizontally. However, for most of the of the experiments the region of the center of the cross arrangement was indeed close (within 10 cm) to the center of the radial sediment distribution. A sample radial spread is shown in Figure 3-11.

The sediment collection tray, if laid at rest at the bottom of the tank, was 195 cm below the plume source. In order to assess the degree to which the sediment, after falling out of the intrusion layer, would undergo additional radial spreading, the collection trays were raised to about 1.2 m below the plume source for some experimental runs. By decreasing the fall distance for the sediment particles it is hoped that any post-peel effects between the sediment particles can be isolated from

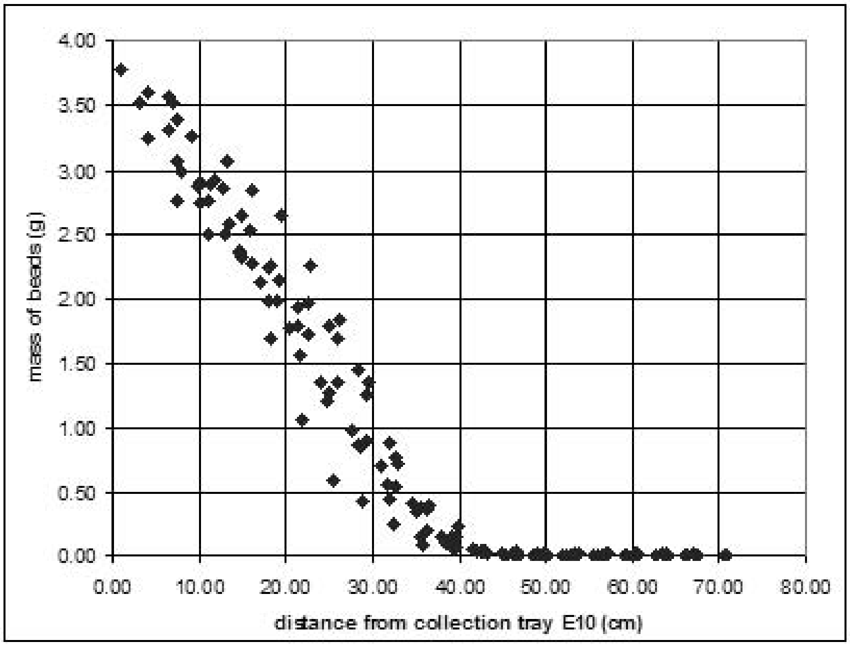

Figure 3-11: A sample radial mass distribution collected (Experiment 042503)

the radial spread due solely to the radial advection by the outer plume. In addition, if it was observed that the spread does not change significantly with the distance traversed by the sediment, it can be argued that the sediment particles, at least on an observational level, were simply passively falling in the post-peel stage.

After the tank were drained, collected samples were lifted out of the tank by a pulley, and the collected trays were dried under a heat lamp and fan overnight. Particles from each dried individual cell with assigned lateral coordinates were brushed out onto a weighing tray, and weighed on an analytical balance, to provide a lateral mass distribution.

Because it was not practical to collect mass samples during an experiment, it was assumed that the radial particle distribution, normalized by the total mass, would be steady, thus can be characterized by its distribution at the end of the experiment.

Chapter 4

Results

4.1 Initial Conditions

Table 4.1 lists the 26 experiments performed, and their associated initial buoyancy and stratification conditions. The three measured data obtained were the trap height, peel height and the radial sediment spread σ_r. The Appendix contains the raw experimental data from which the measured values and their errors were obtained. For each data point, the predicted values from various models are offered for comparison. The models used are CORMIX, a prediction for a multiphase phase plume by Socolofsky [52] with the same total initial buoyancy, and the integral plume model developed by Crounse [20] and Wannamaker [63]. This is presented in detail in Section 4.4. Model input values for each of the runs are shown in the Appendix.

Run	Source	Source	Bottom	ρ_0	N	Particles	particle	u_s	Q_b	ρ_s	Q_s	B	% Bead	% Salt
	d (cm)	depth (m)	depth (m)	(kg/m^3)	(1/s)		d (m)	(m/s)	(m^3/s)	(kg/m^3)	(m^3/s)	(m^4/s^3)		
040503	2.5	0.29	1.95	998.8	0.33	AH	8.35E-05	0.005	2.4E-06	998.8	5.0E-05	3.4E-05	100%	0%
042203	2.5	0.29	1.95	998.8	0.27	AH	8.35E-05	0.005	1.2E-06	1026.3	5.0E-05	3.0E-05	56%	44%
041803	2.5	0.29	1.95	998.8	0.28	AH	8.35E-05	0.005	4.1E-17	1067.5	5.0E-05	3.4E-05	0%	100%
120503	2.5	0.19	1.95	1002.1	0.27	AH 88	9.65E-05	0.006	8.9E-07	1036.1	4.3E-05	2.9E-05	44%	56%
121003	2.5	0.19	1.95	1002.0	0.27	AH 88	9.65E-05	0.006	1.1E-06	1051.6	4.3E-05	3.8E-05	40%	60%
071603	0.8	0.27	1.95	1004.0	0.29	PS	3.14E-04	0.002	3.2E-06	1004.0	3.7E-05	1.4E-06	100%	0%
072803	0.8	0.27	1.95	1003.8	0.31	PS	3.14E-04	0.002	3.2E-06	1009.2	3.7E-05	3.4E-06	42%	58%
081103	0.4	0.19	1.95	1003.6	0.32	PS	3.14E-04	0.002	3.7E-07	1019.3	4.7E-06	8.8E-07	19%	81%
081903	0.8	0.27	1.95	1001.7	0.36	PS	3.14E-04	0.002	1.4E-06	1001.7	2.6E-05	6.4E-07	100%	0%
082103	0.8	0.27	1.95	1005.4	0.27	PS	3.14E-04	0.002	1.7E-06	1024.2	2.3E-05	5.0E-06	15%	85%
082903	0.4	0.27	1.95	1005.0	0.26	PS	3.14E-04	0.002	1.6E-06	1024.4	1.2E-05	2.9E-06	24%	76%
090303	0.4	0.27	1.95	1004.9	0.29	PS	3.14E-04	0.002	1.2E-06	1016.7	2.3E-05	3.2E-06	17%	83%
091703	0.8	0.27	1.20	1001.6	0.27	PS	3.14E-04	0.002	1.6E-06	1002.3	2.3E-05	9.5E-07	82%	18%
091903	0.8	0.27	1.20	1004.3	0.26	PS	3.14E-04	0.002	1.7E-06	1004.3	2.6E-05	7.7E-07	100%	0%
092303	0.8	0.27	1.20	1006.5	0.25	PS	3.14E-04	0.002	2.0E-06	1006.5	2.6E-05	8.7E-07	100%	0%
100103	0.4	0.27	1.20	1003.4	0.32	PS	3.14E-04	0.002	2.3E-07	1055.1	1.2E-05	5.9E-06	2%	98%
100803	0.4	0.27	1.20	1002.8	0.30	PS	3.14E-04	0.002	2.3E-07	1022.9	1.2E-05	2.4E-06	4%	96%
101503	0.4	0.27	1.20	1004.1	0.28	PS	3.14E-04	0.002	2.3E-07	1024.9	1.2E-05	2.4E-06	4%	96%
111203	0.4	0.27	1.20	1001.2	0.26	PS	3.14E-04	0.002	1.1E-06	1002.0	2.4E-05	7.3E-07	75%	25%
111703	0.4	0.27	1.20	1003.1	0.27	PS	3.14E-04	0.002	1.3E-06	1004.0	2.1E-05	8.0E-07	76%	24%
111903	0.8	0.27	1.20	1002.9	0.27	PS	3.14E-04	0.002	2.0E-06	1004.3	2.6E-05	1.3E-06	74%	26%
112203	0.8	0.27	1.20	1003.4	0.29	PS	3.14E-04	0.002	1.7E-06	1017.0	1.8E-05	3.1E-06	24%	76%
071403	0.8	0.27	1.95	1002.8	0.27	PS	3.14E-04	0.002	9.5E-17	1013.1	3.7E-05	3.8E-06	0%	100%
042103	2.5	0.29	1.95	998.8	0.30	AE	1.45E-04	0.012	1.7E-06	998.8	5.0E-05	2.4E-05	100%	0%
042503	2.5	0.29	1.95	998.8	0.26	AE	1.45E-04	0.012	9.8E-07	1020.9	5.0E-05	2.5E-05	56%	44%
050103	2.5	0.29	1.95	998.8	0.29	AE	1.45E-04	0.012	4.1E-17	1048.8	5.0E-05	2.5E-05	0%	100%

Table 4.1: Initial conditions for current experiments. See index of figures in Table A.1 in Appendix for corresponding figures.

4.2 Experimental Determination of Data Points

4.2.1 Peel Depth

The peel depth for each experimental run was determined from the images taken by the CCD camera. Images were viewed to locate where the plume fluid began to reverse direction. Movie frames were loaded into `MATLAB` and the vertical coordinate at which the peel was observed was picked out by eye, and the vertical pixel distance from the plume source in the picture was converted to plume depth. This was done every 5 movie frames.

Figure 4-1 shows the peel depth determined from a range of frames in a movie from one experiment, plotted against a sample image frame number. This enabled the movie images to be used to locate a measurement of the peel depth. In a stratified environment, the Schlieren effect may be observed where there is vertical variation in the index of refraction from the top to the bottom of the tank. This may introduce a bias to any lengths that are taken from pictures taken of stratified environments. This was partly overcome, or at least shown to be not so significant in the experiment, by placing a pole, with a black marking every 10 cm, in the same plane as the centerline of the plume and the laser sheet. Figure 4-2 shows a tank picture, with pixel measurements every 10cm to show that the measurement pole markings lined up quite consistently with the pixel measurements (standard deviation of ±1 pixel), even in the presence of stratification.

(a)

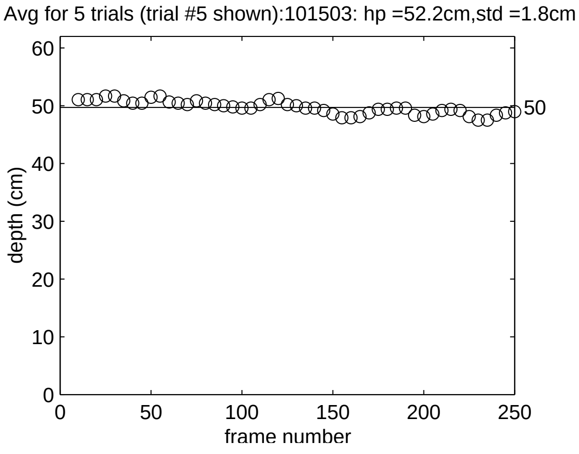

(b)

Figure 4-1: Experimental run 101503: a) A frame from the experimental movie, b) Plot showing the peel depth determined from a number of movie frames, and the average taken for one sample run. Five similar runs were used for each experimental run, to get an average for h_p.

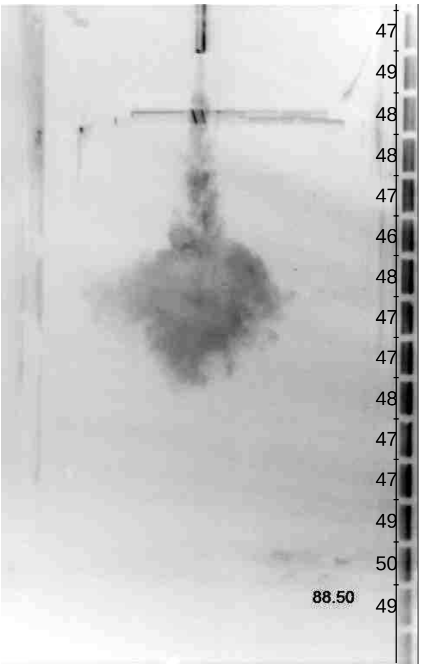

Figure 4-2: Inverted image of experimental tank. The black tick marks correspond to the midpoints of the 10 cm markings on the pole. Adjacent numbers represent the length of the line segments in pixels, showing that the effect of parallax on the acquired images is not significant.

4.2.2 Trap Depth

The trapping depth of the intrusion layer of the plume was obtained using the fluorescence profiles, from the fluorometer connected to the OS300 CTD probe, which was converted to a concentration against depth plot, as shown in Figure 4-3.

The trap depth was taken to be the ratio of the first and zeroth moment. Since up to five vertical profiles were measured for each experimental run at different horizontal positions of the tank, the individual trap depths were weighted by the respective zeroth moment of the profile. This was done so that if, for whatever reason, the dye readings in a single run were weak compared to the rest, the first moment of this run would not be as important in determining the overall trap height. So:

$$h_t = \frac{\sum_i \frac{M_{1,i}}{M_{0,i}} M_{0,i}}{\sum_i M_{0,i}}$$

which simplifies to

$$h_t = \frac{\sum_i M_{1,i}}{\sum_i M_{0,i}} \tag{4.1}$$

Similarly, the standard deviation of the concentration profile was used to express the variation of the reported trap depth,

$$\sigma_{h_t} = \sqrt{\frac{\sum_i M_{2,i}}{\sum_i M_{0,i}} - h_t^2} \tag{4.2}$$

where for each run i,

$$\begin{aligned} M_{0,i} &= \int_0^\infty c_i dz \\ M_{1,i} &= \int_0^\infty c_i z dz \\ M_{2,i} &= \int_0^\infty c_i z^2 dz \end{aligned} \tag{4.3}$$

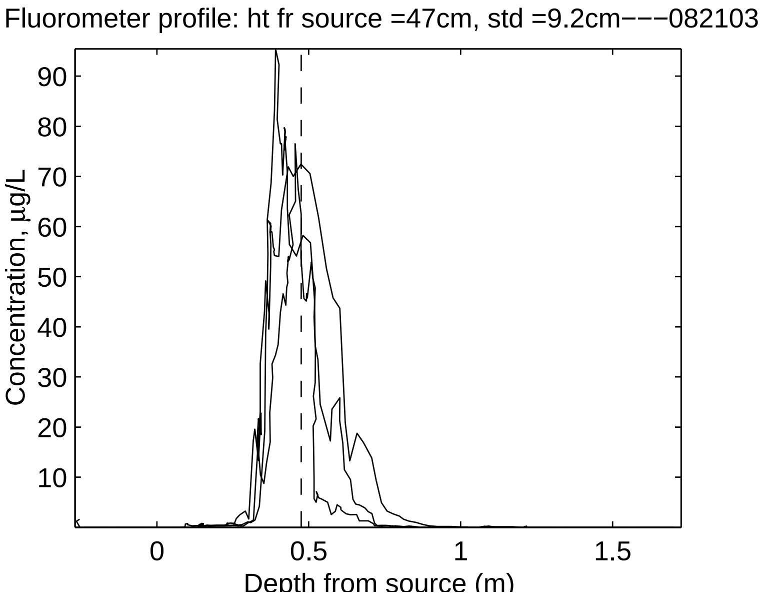

Figure 4-3: Sample fluorometer profile (Experiment 082103).

4.2.3 Radial Sediment Spread

The radial spread of the descending sediment was determined using the mass recorded from the collection trays. Collected samples were dried by heat lamp and fan, and particles from individual cells with assigned coordinates were weighed. When all the cells were weighed, the center of the distribution was taken to be the cell containing the maximum weight of collected particles. The variance and standard deviation were obtained for this two-dimensional distribution from the center, and this was taken to equal σ_r, the radial sediment spread.

Since initial observation of the distribution showed that the resulting sediment spread assumed a two-dimensional Gaussian distribution, one was fit to the data, and the sediment spread taken to be the radial variance of this distribution.

The method to fit a 2-D Gaussian distribution to the data was as follows:

A two-dimensional Gaussian distribution describing the concentration $c(r)$ of sediment, with maximum and mean located at the origin was given by

$$c = c_{max} \exp\left(-\frac{r^2}{\sigma_r^2}\right), \tag{4.4}$$

where

$$r = \sqrt{(x - x_0)^2 + (y - y_0)^2}. \tag{4.5}$$

In Microsoft Excel, a normal distribution of one dimension has been defined in a built-in function `normdist`, in which

$$\texttt{normdist(r,0,}\sigma_e\texttt{,false)} = \frac{1}{\sqrt{2\pi}\sigma_e} e^{-\frac{r^2}{2\sigma_e^2}} \tag{4.6}$$

Specifying an estimate for the location of the center of the distribution (x_0, y_o), and using Equations 4.4 and 4.6, A 2-D Gaussian concentration distribution was fit by

$$c_{fit}(r(x_0, y_o), \sigma_e) = c_{max}\sqrt{2\pi}\sigma_e \texttt{normdist(r,0,}\sigma_e\texttt{,false)}. \tag{4.7}$$

Therefore σ_e, x_0 and y_0 in Equation 4.7 were used as fitting parameters for the sediment distribution, center (x_o, y_o), and characteristic spread. In the current experiments the distribution of sediment was expected to be axisymmetric, i.e. the 1D variances σ_x and σ_y should be equal. Taking $\sigma_x = \sigma_y = \sigma_e$, the radial spread was therefore

$$\sigma_r = \sqrt{\sigma_x^2 + \sigma_y^2} = \sqrt{2}\sigma_e \tag{4.8}$$

The fitting values were chosen to minimize the least squares difference between the the points on the analytical curve and the corresponding measured value at the same radii, i.e. the expression $\sum_{i=1}^{144} |(c_{i,fit}(\sigma_e, x_0, y_0))^2 - c_{i,measured}^2|$ was minimized. Figure 4-4 shows a sample of a fit of the 2-D Gaussian with the measured sediment spread, which showed good agreement, and thus justified its use to define the distribution.

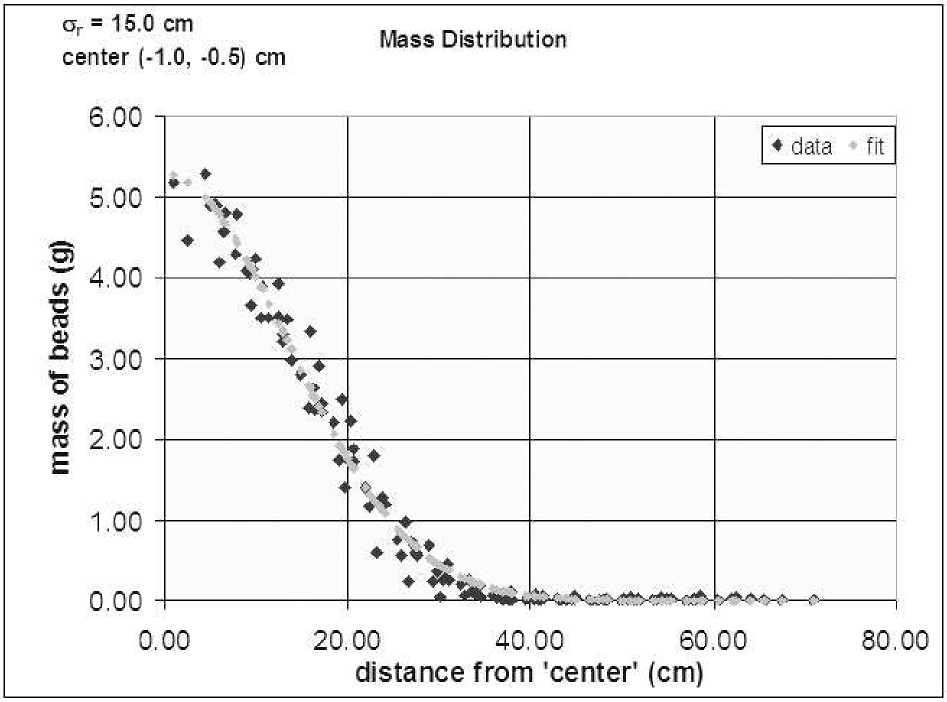

Figure 4-4: Sample of Gaussian fit to mass distribution of experimental run 101503, showing the center of the distribution and the resulting σ_r

4.3 Observations

Figure 4-5 shows the general observed behavior of a sediment laden plume of Type 1* ($U_N << 1$). Initially, both phases of the plume behaved like a single phase plume, with the combined phase reaching neutral buoyancy at around the trap depth. Because of the momentum imparted to it by the loss of buoyant potential energy, the bulk phase sank beyond the neutral buoyancy depth. The sediment particles, being constantly negatively buoyant, continued to sink out of the plume. The plume fluid reached a maximum depth, the peel depth h_p, after which it began to separate from the falling sediment, and level out at the trap height h_t.

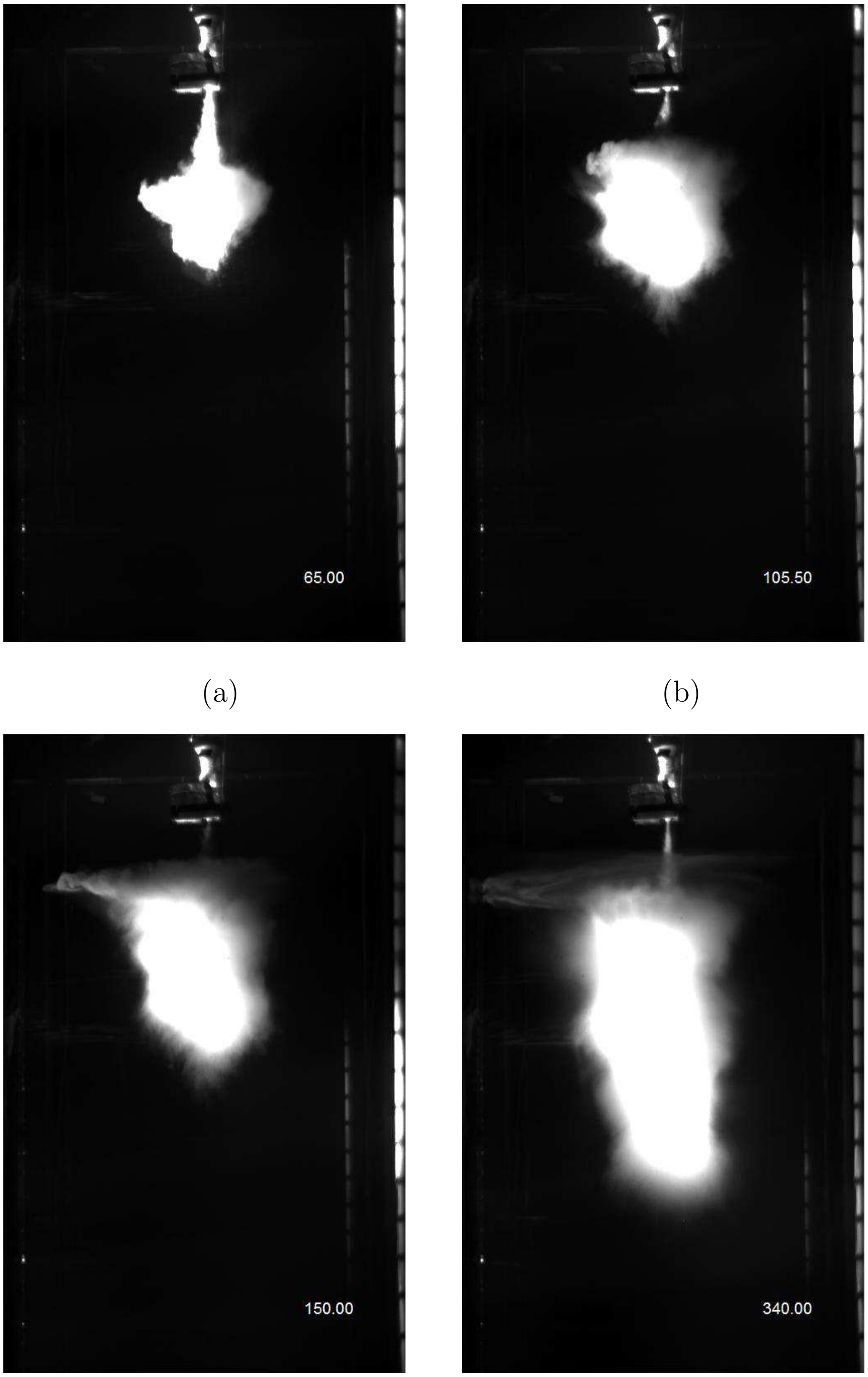

(a) (b)

(c) (d)

Figure 4-5: Experimental run 081903, showing: (a) Initial intrusion, (b) Sediment fallout from intrusion layer, (c) The intrusion layer spreading radially outward, (d) Sediment falling passively out of the intrusion. Corner numbers indicate the elapsed time (in seconds) based on movie frame delays.

However, for the Type 1* plume, the slip velocity of the sediment particles, u_s, was much smaller than this initial restoring velocity of the plume fluid (the definition of $U_N << 1$), and as a result, the sediment was prone to being advected along with the intrusion layer. Since the particles were still sinking at their slip velocity, they were only able to ride in the intrusion layer for as long as they stayed inside. Once they left the intrusion layer, they were observed to fall passively downwards. Observations over a longer time showed that a wide cylindrical column of falling particles forms below the intrusion layer, where the sediment appeared to be steadily falling out.

4.4 Trap and Peel Depth

Numerical models

While raw experimental data is presented in the Appendix, the method of presentation of the experimental results for trap and peel depth in this chapter is by comparison with different numerical predictions. The models used were an empirical prediction for a multiphase phase plume by Socolofsky and Adams [55] with the same total initial buoyancy, CORMIX, and the integral plume model developed by Crounse [20] and Wannamaker [63]. The reason for using multiple models was because each model was able to model some, but not all aspects of the experimental conditions.

The first prediction method used for predicting the trap and peel depths was that proposed by Socolofsky [52], described in Section 2.3.2. Equations 2.23 and 2.22 embody the dependence of trap and peel depth on U_N, and are repeated below: these will also be referred to as the SAS correlations.

Prediction of trap height h_t as a function of U_N:

$$h_t = (2.8 - 0.27U_N)\left(\frac{B}{N^3}\right)^{1/4}$$

Peeling height h_p as a function of U_N:

$$h_p = 5.2 \exp\left(-\frac{(U_N - 1.8)^2}{10.1}\right)\left(\frac{B}{N^3}\right)^{1/4}$$

The equations above are applicable to pure bubble plumes, where the buoyancy is solely due to the dispersed phase. When $U_N = 0$, Equations 2.22 and 2.23 predict trap and peel heights of single phase plumes. They also suggest that if $U_N << 1$, which was the case for the current experiments, the plumes will trap and peel at levels close to that of equivalent single phase plumes of equal buoyancy. While the two equations above do take the effect of particles into account, they do not account for situations where the initial buoyancy is due to a mixture of dispersed and continuous phases. In addition, the equations are suited for pure plumes, where no initial momentum is present.

4.4.1 CORMIX

The Cornell Mixing Zone Expert System (CORMIX) was developed by the DeFrees Hydraulics Laboratory at Cornell University, Ithaca, New York, in cooperation with the EPA, for studying aqueous pollutant discharges into a range of water bodies [34]. Therefore, at the current stage of the model's development, the model is only able to handle single phase plume discharges. It includes many different numerical algorithms for predicting plume behavior, which are automatically invoked as needed via a flowchart characterizing the flow in question. CORMIX can model a wide range of discharge flows, including attachment of a buoyant plume to the bottom, buoyancy and momentum dominated buoyant jets, and upstream intruding plumes. It has a very user-friendly graphical user interface which allows the user to input the water body geometry and properties, discharge flowrates and initial pollutant concentrations. The user is also able to add such effects as tidal effects to the water body, and the decay constants of non-conservative pollutants, all of which are delineated in its user manual. Although CORMIX can only model single phase plumes, the trap and peel depths from this model is useful for comparison with those of the current experiment.

The CORMIX1 input interface only allows for a linear density profile to be input for the water body (taken here to be unbounded). Also, the discharge is restricted to be directed upwards, and of a single phase. For this reason, to preserve the physics of the experimental flow, the CORMIX model used was for a positively buoyant plume, with the same discharge total buoyancy as that of the experiments, and with the same value of N experienced by the plume during ascent. A schematic of the comparison is shown in Figure 4-6

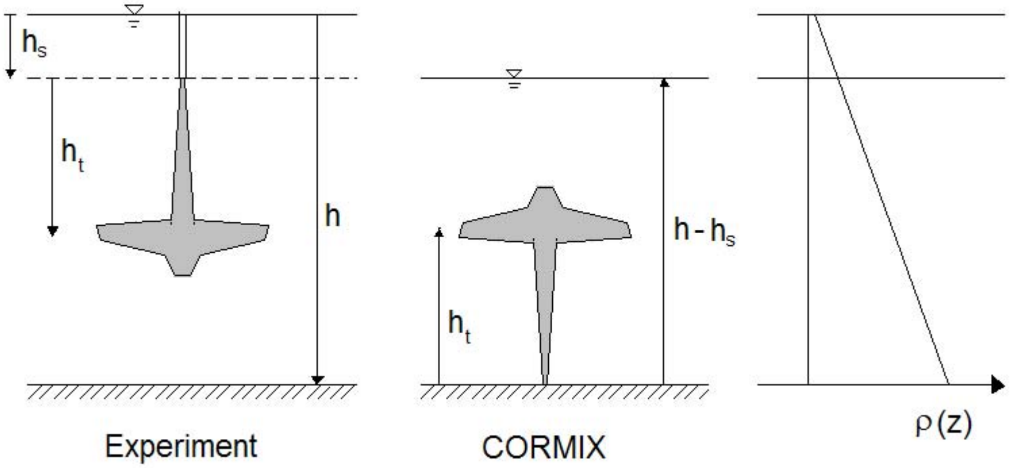

Figure 4-6: Schematic of inverted CORMIX model scenario used for comparison with experimental runs. Both scenarios will experience the same stratification parameter N, ceiling depth/height, and have the same initial buoyancy.

Examples of other inputs to the CORMIX model are outlined in Table A.28 of the Appendix. CORMIX, while only designed for single phase plumes, was deemed suitable for comparisons, since it can take initial plume momentum into account.

D-CORMIX Model

Another version of the CORMIX model, named D-CORMIX (for dredging), is available for modeling sedimenting flows, for example in particle laden gravity currents along shoreline and estuaries. The details of the model are explained by Doneker and Jirka [25]. D-CORMIX uses the same modules of flow classification as CORMIX, but is a mirror image, similar to what was done for CORMIX to model the current experiments, shown in Figure 4-6. However, the manual states that any settling that would occur and that would alter the density current's density, are implemented only if the flow itself comes into contact with the bottom (which only applies to certain flow classes in the program). Since the expected single phase plumes from all of the experiments did not contact the bottom, D-CORMIX would not predict a sediment fall-out. Instead, it would only yield the inverted versions of the CORMIX outputs, already presented above, and provides no additional information for the flow.

4.4.2 Full Multiphase Integral Plume Model

The final model used was the integral plume model, developed originally by Crounse et al. [20] for bubble plumes, calibrated using the experimental results from Socolofsky [52], and also adapted by Wannamaker [64] for sinking hydrate plumes. A detailed description of the workings of the model are found in the works above. For comparison with this set of experimental runs, the `PLUME RACE` version of the model was used, which enabled both a buoyant brine flow and particles to constitute the buoyancy source. The integral model took initial momentum into account throughout the plume descent. Also, by using this model, a more accurate ambient density profile (the profile obtained by the density profiler in section 3.2.2) could be used for the ambient environment for the numerical run. In addition, the size distribution of the particles (obtained by sieve analysis as outlined in Section 3-6) was directly inputted into the model. For the current experiments the sediment density was taken as 1050 kg/m^3 for polystyrene beads, and 2450 kg/m^3 for glass.

For each vertical depth grid point, the integral model calculated a wide variety of plume properties such as the buoyancy flux, momentum, entrainment fluxes, etc. The peel height was picked as the shallowest depth where an outer plume segment began, as this is the definition of the first peel. The trap height was determined as where the buoyant forces of the outer and inner plume coincided. This point was chosen because it occurred always at a depth that was greater than the first point where the inner plume reverses buoyancy (a good initial estimate), and less than the point where the outer plume begins to reverse its buoyancy. In this way the trap height estimate could roughly account for the overshoot of the intrusion layer due to its momentum, which allowed it to mix with denser fluid before intruding horizontally, and trap slightly lower.

While this model can match experimental initial conditions better than the other two models, this model was not able to model any post intrusion events such as the lift-off phenomena of the intrusion layer itself as it deposits sediment.

	Single /Multiphase	**Momentum**	**Particles**	**Mixed buoyancy source**	**Intrusion lift-off**
SAS correlations	Multiphase	no	yes	no	no
CORMIX	Single	yes	no	no	no
Integral model (IM)	Multiphase	yes	yes	yes	no

Table 4.2: Summary of modeling capabilities of numerical predictions.

4.4.3 Comparison among models

Table 4.2 summarizes the modeling capabilities of the three prediction methods. Figure 4-7 shows the outputs of each model for a range of initial buoyancy fluxes.

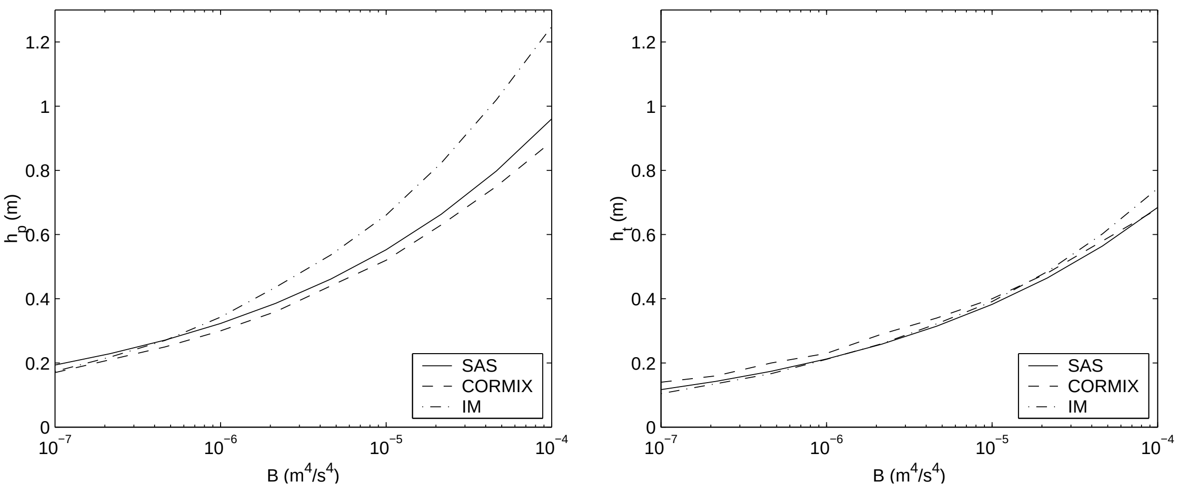

h_p h_t

Figure 4-7: Comparison of model outputs of h_p and h_t. Initial conditions: Glass (g' = 2450 kg/m^3), Brine ($\Delta\rho_b$ = 20 kg/m^3), $N = 0.3s^{-1}$, $N_m = 10^{-4}$.

While the trap depths were generally in agreement between the three models, the integral model overestimated the peel depth by up to 30% when compared to the other models. The reason for the discrepancy was not due to initial momentum effects, since the initial momentum number N_m was held constant in the runs depicted in Figure 4-7.

4.4.4 Buoyancy composition

The models were applied with inputs corresponding to typical experimental conditions, varying the fraction of particles in the initial buoyancy flux. Figure 4-8 shows the resulting peel and trap depths.

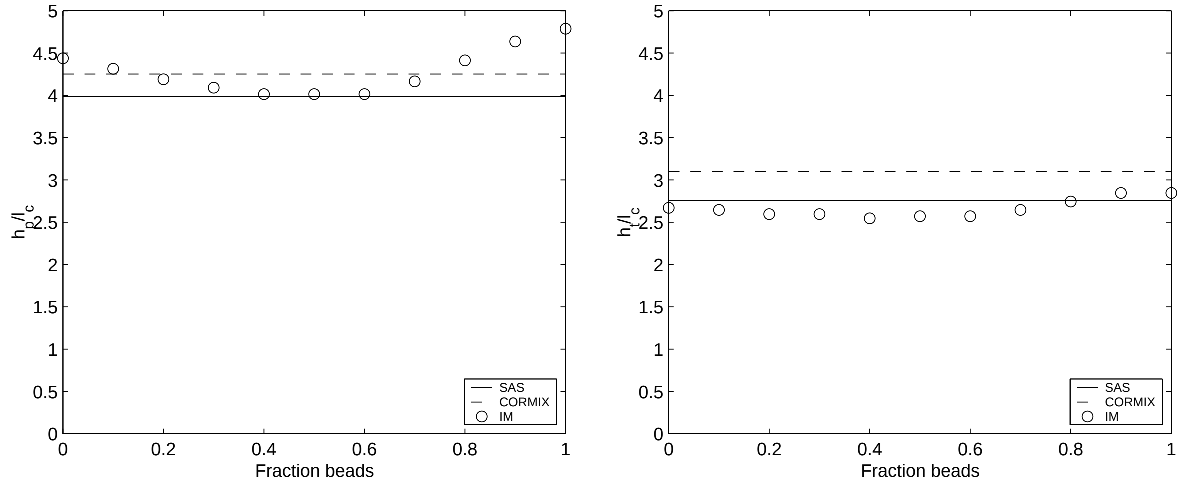

h_p h_t

Figure 4-8: Comparison of model outputs of h_p and h_t, varying bead fraction of initial buoyancy. Initial conditions: $B = 10^{-5}$ m^4/s^3, Glass (ρ_s = 2450 kg/m^3, d_s = 0.01 cm), Brine ($\Delta\rho_b$ = 20 kg/m^3), $N = 0.3s^{-1}$, d_{port} = 0.5 cm. l_c is the characteristic plume length scale, defined as $l_c = (B/N^3)^{1/4}$.

The output of the integral model showed a maximum peel depth with 100% particles. There was a minimum peel depth for buoyancies of a 1:1 ratio. The single phase peel depth was not as large in value as the pure particle plume, but was larger than the values predicted by the other models. The minimum predicted peel depth from the integral model was very close to the constant predicted values by CORMIX and by the empirical relation (SAS).

It was unclear why there existed a variation of the integral model prediction of the peel depth with buoyancy composition. If the momentum of the particles physically contributed significantly to the bulk fluid momentum, then the trend would have been monotonic with bead fraction. Also, the predicted peel depth when the bead fraction goes to zero, should approach that of a single phase plume. However, the predicted values were all within the range between the predictions of the other two models.

Although there was a small trough in the results for the trap depth, this is not nearly as marked as for the peel depth, the trap depths remained quite constant for all particle fractions, and were consistent with the other model predictions. The integral plume model did not take into account the possible change in buoyancy of the intrusion layer with sediment fallout, and thus predicted trap heights were in good agreement with the other models, which also did not consider this factor.

Initial Momentum and Volume

Section 3.3.3 described the use of two ratios of length scales, the momentum number N_m and the volume number, N_q, to determine the significance of the plume initial momentum and volume flux on plume trap and peel depths. In this section, for a typical buoyancy flux B and buoyancy frequency N of the experiments, the integral plume model and CORMIX were run for a range of momentum and volume numbers, and the resulting trap and peel depths compared to the pure bubble plume prediction by Socolofsky [52] (SAS prediction). Since the SAS prediction is that for a pure bubble plume, it does not factor in either momentum or initial volume flux, and is thus suitable as a reference for sensitivity of N_m and N_q for the other two computer models. The definitions of N_m and N_q are repeated below:

$$N_m = \left(\frac{MN}{B}\right)$$

$$N_q = \left(\frac{Q^{4/3}N^{5/3}}{B}\right)$$

varying N_m for the same buoyancy flux involved change of the port initial diameter (and thus initial velocity), while N_q was varied by varying the density difference of the brine (since $B = \frac{\Delta\rho}{\rho_0}Q$). Figure 4-9 plot the normalized difference in CORMIX model SAS predicted trap and peel depths for a buoyant release comprising low particle fraction, while Figure 4-10 plot the same with the buoyancy made up of half brine and half particles. Figures 4-11 and 4-12 compare the integral plume model with SAS. Note that the trap and peel depths have been non-dimensionalized by dividing by their respective stratification length scale $l_c = B^{1/4}/N^{3/4}$. While for the IM and SAS predictions the value of l_c were identical, for CORMIX, because certain flow rates brought the model to a different flow module, the value of B, and therefore l_c, was adjusted such that the same CORMIX flow module was used for all ranges of N_m and N_q.

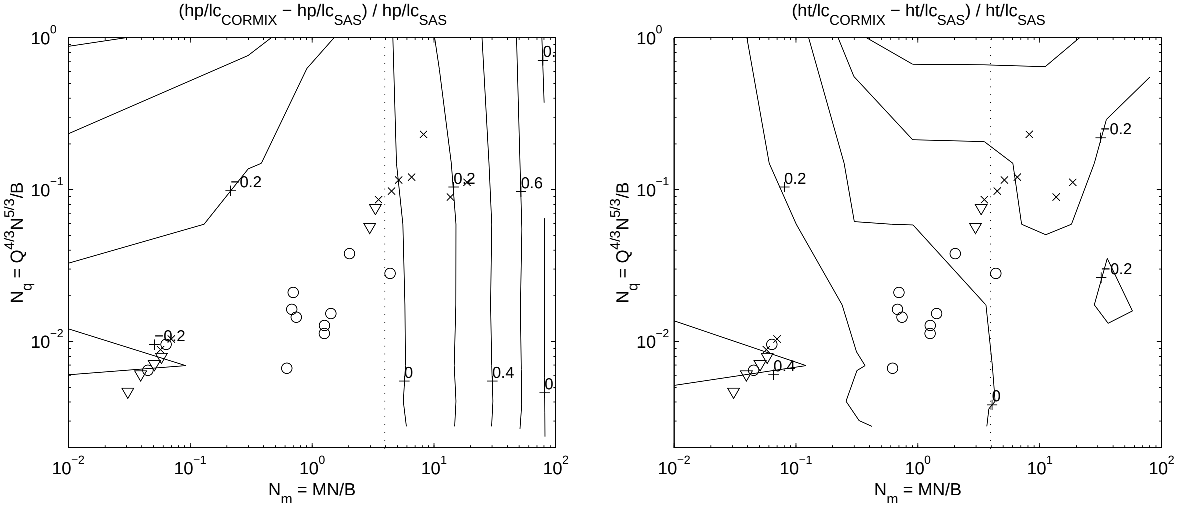

h_p h_t

Figure 4-9: Contours showing normalized difference between CORMIX model and SAS predictions, varying momentum and volume numbers N_m and N_q. Particle fraction = 6% Points represent individual experimental run values of N_m and N_q: Crosses: Particle fraction less than 25%; Triangles: Particle fraction between 25 % and 75%; Circles: Particle fraction greater than 75%. Dotted line is $N_m = 4$.

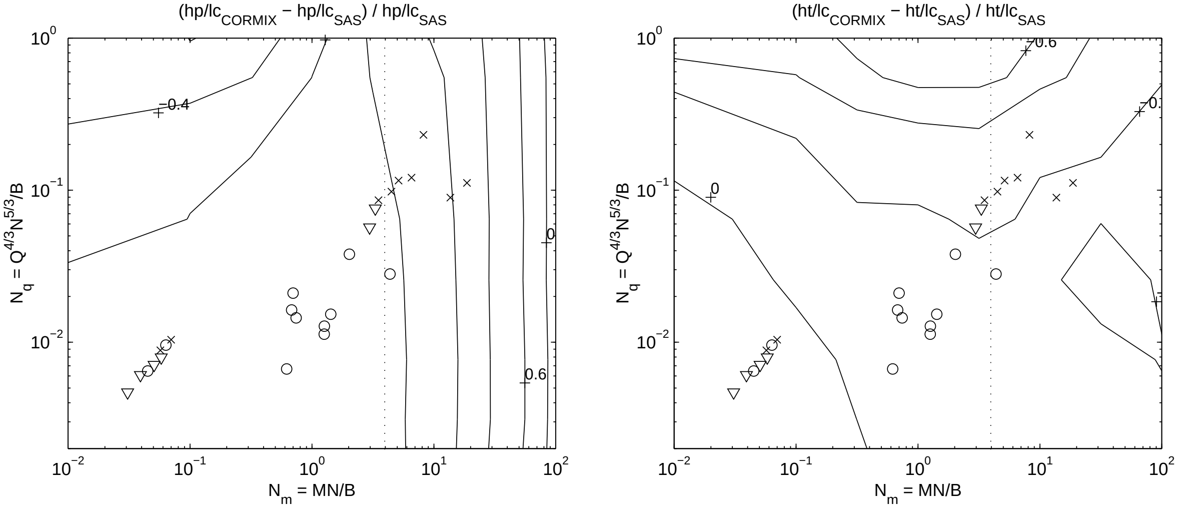

h_p h_t

Figure 4-10: Contours showing normalized difference between CORMIX model and SAS predictions, varying momentum and volume numbers N_m and N_q. Particle fraction = 50%. Points represent individual experimental run values of N_m and N_q: Crosses: Particle fraction less than 25%; Triangles: Particle fraction between 25 % and 75%; Circles: Particle fraction greater than 75%. Dotted line is $N_m = 4$.

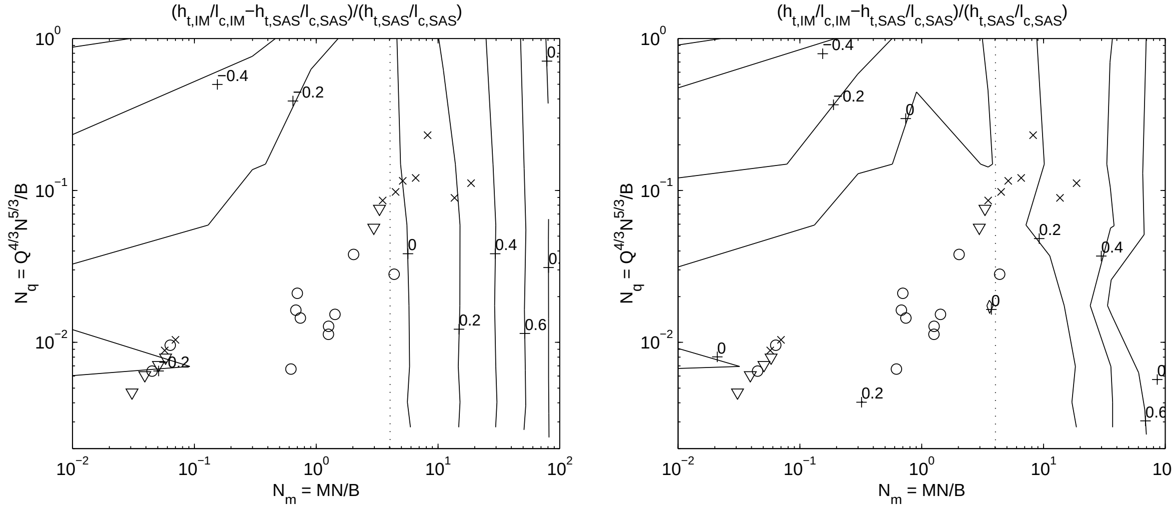

h_p h_t

Figure 4-11: Contours showing normalized difference between integral model (IM) and SAS predictions, varying momentum and volume numbers N_m and N_q. Particle fraction = 6% (IM model is incapable of modeling plumes with no particles). Points represent individual experimental run values of N_m and N_q: Crosses: Particle fraction less than 25%; Triangles: Particle fraction between 25 % and 75%; Circles: Particle fraction greater than 75%. Dotted line is $N_m = 4$.

Figure 4-9 show that for large momentum numbers the peel and trap depths predicted by the integral model will begin to differ significantly from the prediction of Equations 2.23 and 2.22. The values of N_m and N_q for each experimental run is also plotted in Figure 4-9. For the peel depth h_p, the plots show that for the range of N_q of the experiments, the runs of momentum number $N_m < 4$ were within 20% of the predictions of Equations 2.22 and 2.23 for pure bubble plumes. For values of $N_m > 4$, the peel and trap depths became increasing sensitive to initial momentum, and differed from the pure bubble plume predictions by more than 20% for the CORMIX-SAS prediction (Figures 4-9 and 4-10).

Figures 4-12 and 4-11 show the normalized difference of the trap depth predicted by the integral plume model, compared with the SAS prediction, at different values of N_m and N_q. Here, the range of experimental data are located on the plot where the integral plume model under-predicts the trap depth, compared to the pure bubble plume prediction (about 30% less). This lower value of predicted h_t is consistent with the under-prediction shown in Figure 4-8 between the integral model and the SAS prediction.

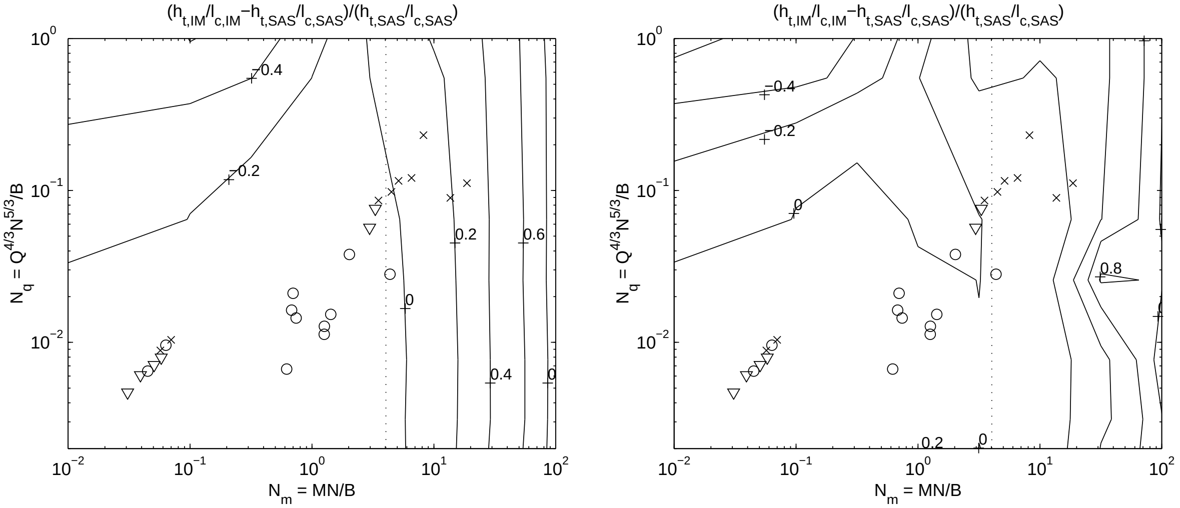

h_p h_t

Figure 4-12: Contours showing normalized difference between integral model (IM) and SAS predictions, varying momentum and volume numbers N_m and N_q. Particle fraction = 50%. Points represent individual experimental run values of N_m and N_q: Crosses: Particle fraction less than 25%; Triangles: Particle fraction between 25 % and 75%; Circles: Particle fraction greater than 75%. Dotted line is $N_m = 4$.

In the light of the sensitivity analysis of initial momentum and volume flux (characterized by the values of N_m and N_q), the criterion used to distinguish between high and low momentum runs was chosen to be $N_m > 4$ for high momentum runs, and $N_m < 4$ for low momentum runs. Since all the runs had values of N_q that were shown not to vary enough to cause significant deviation from the pure bubble plume prediction, it was concluded that the experimental results had low flow rates, and were not sensitive to N_q.

4.4.5 Comparison with Experiments

Figure 4-13 shows the experimentally obtained peel depths in comparison with the three models in two plots. The first set of data points have been categorized by low and high fraction of particles making up the total initial buoyancy (less than or greater than 50% particles). The second plot, with identical points, are sorted by N_m of the run, which characterized the plume release momentum. As described in the previous section, $N_m = 4$ was chosen as the cutoff momentum number for distinguishing between high and low momentum experimental runs.

Inspection of Figure 4-13 yielded fair agreement with the model predictions, for runs in which the momentum number $N_m < 4$. For most of the runs of high N_m, the points lay to the right of the straight line, meaning that the experimental peel depths were higher than all of the numerical predictions. This made sense physically, since the higher the momentum of the initial bulk fluid, the further it would descend to a depth where the buoyancy began to counteract its extra momentum.

The second plot of Figure 4-13 removed these high momentum runs to isolate the particle fraction effect. Overall, there was no clear trend of the peel depth being affected by the buoyancy composition. This also was reasonable, since for the experimental runs, $U_N << 1$, and the plumes were expected behave like single phase plumes.

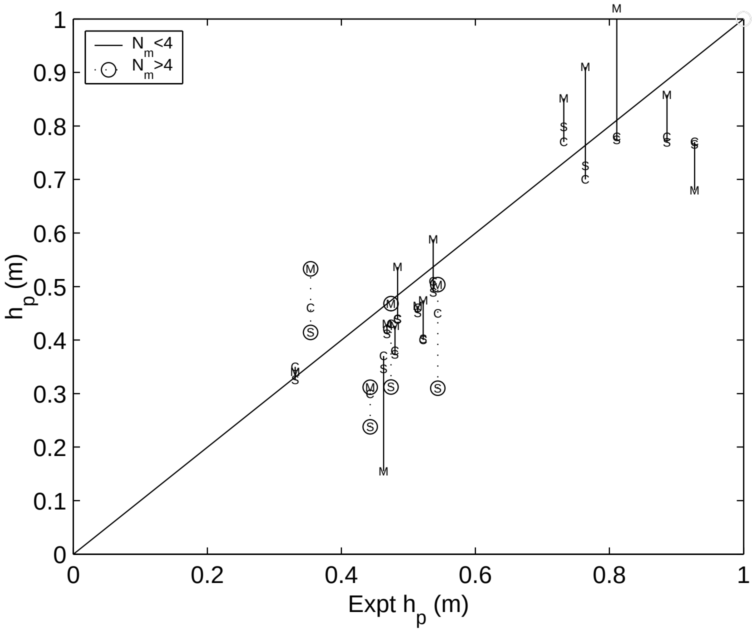

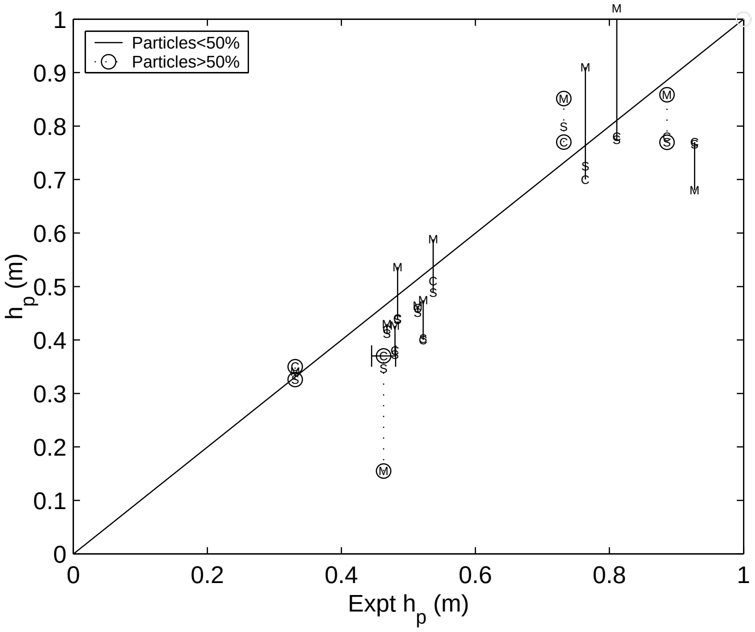

Figure 4-13: Comparison between experimental and model predictions for h_p, based on different experimental conditions. Top: Data points sorted by momentum number N_m; Bottom: Data points sorted by fraction of particles, and with high momentum ($N_m > 4$) runs omitted. Data points: S = Equation 2.23; C = CORMIX; M = Integral Model. Lines join the numerical predictions for the same experimental run. Typical experimental error bar (horizontal) shown on bottom plot.

Figure 4-14 shows the effect of both momentum and particle fraction of the trap depth, as compared with the numerical models. As for the peel depth in Figure 4-14, the data is presented with high momentum runs included in the top plot ($N_m > 4$), which in general resulted in trap depths greater than a plume predictions without momentum.

Upon removing the high momentum runs, and categorizing the data by the particle fraction, there was a slight trend of the experimental runs with higher bead fractions to consistently trap at a smaller depth than all of the models had predicted. This may be attributed to the gain of positive buoyancy of the intrusion layer after depositing its sediment, which enabled the layer to trap at a higher neutrally buoyant level (or smaller neutral depth).

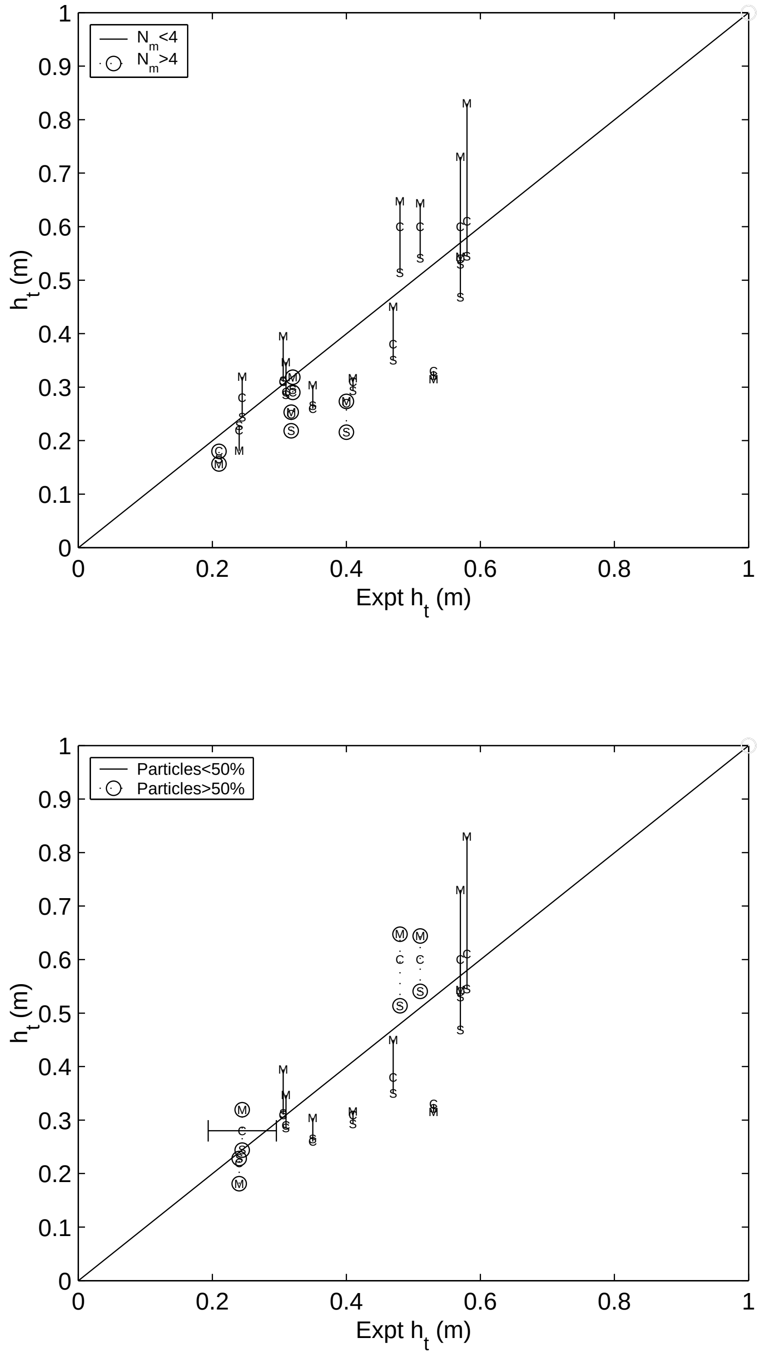

Figure 4-14: Comparison between experimental and model predictions for h_t, based on different experimental conditions. Top: Data points sorted by momentum number N_m; Bottom: Data points sorted by fraction of particles, and with high momentum ($N_m > 4$) runs omitted. Data points: S = Equation 2.22; C = CORMIX; M = Integral Model. Lines join the numerical predictions for the same experimental run. Typical experimental error bar (horizontal) shown on bottom plot.

4.4.6 Comparison with Pure Bubble Plume Predictions

The predictions of trap and peel depths are based on the non-dimensional slip velocity (U_N) of the particles used, Equations 2.22 and 2.23, and are repeated here:

$$\begin{aligned} h_t &= (2.8 - 0.27U_N)\left(\frac{B}{N^3}\right)^{1/4} \\ h_p &= 5.2\exp\left(-\frac{(U_N - 1.8)^2}{10.1}\right)\left(\frac{B}{N^3}\right)^{1/4} \end{aligned}$$

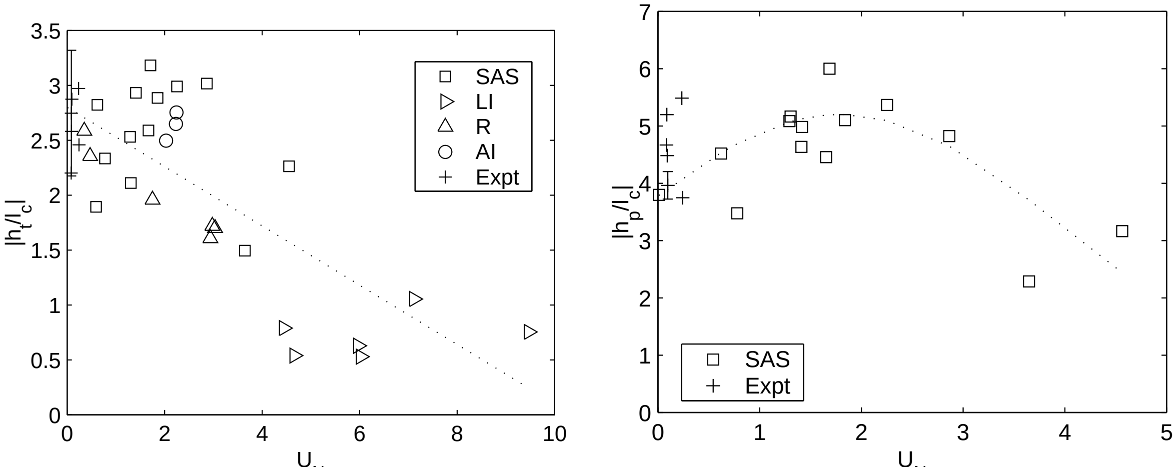

Non-dimensional trap depth Non-dimensional peel depth

Figure 4-15: Plot of experimental trap and peel depths against U_N. The current work's experimental data points have been inverted for comparison with bubble plumes. Key: SAS = Socolofsky [52]; LI = Lemckert and Imberger [38]; R = Reingold [48]; AI = Asaeda and Imberger [7]; Expt = Current Experiments. Only the experiments with mostly particles constituting the plume buoyancy (more than 50%), and with low initial momentum ($N_m < 4$) were used for the comparison. Typical error bar shown for one experimental data point (on far left).

Figure 4-15 plots some runs in comparison to bubble plumes by other authors, from which Equations 2.22 and 2.23 were fit. The trap and peel depths were reversed for comparison with positively buoyant multiphase plumes. The runs used for comparison had low initial momentum numbers (small N_m), and high percentage of particles (such that the buoyancy is mainly from the particles, in analogy to bubble plumes). This showed that the peel and trap depths in the current experiments were within the set of data points used for the curve fitting Equations 2.22 and 2.23.

4.5 Radial Sediment Spread

The results for the effects of buoyancy composition, slip velocity and ambient stratification on radial spread, are shown in Figure 4-16. There is an observed trend between the radial spread and the characteristic spread σ_r described in Equation 2.38. The relation confirms the following: the higher the intrusion flux, due to increased initial buoyancy, and the longer time elapsed for particles to remain inside the intrusion layer (indicated by lower slip velocity), the higher the resulting lateral spread. Also, the proposed relation between the total buoyancy B, N and u_s in Equation 2.38 appears reasonable.

Figure 4-16 shows the effect of plume U_N, composition of buoyancy source and initial momentum number, on the radial sediment spread. Examination of the data points labeled based on various experimental conditions in Figure 4-16, show that the sediment spread itself did not appear to be dependent on either buoyancy source composition or the non-dimensional slip velocity U_N. In the regime of $U_N << 1$, the particles behaved as if they were part of the continuous phase. However, the experimental runs with large initial momentum number $N_m = (MN/B)^2$, exhibited radial distributions higher than that expected by the prediction of Equation 2.38. The bottom plot of Figure 4-16 includes only the data with relatively low momentum number (less than 4).

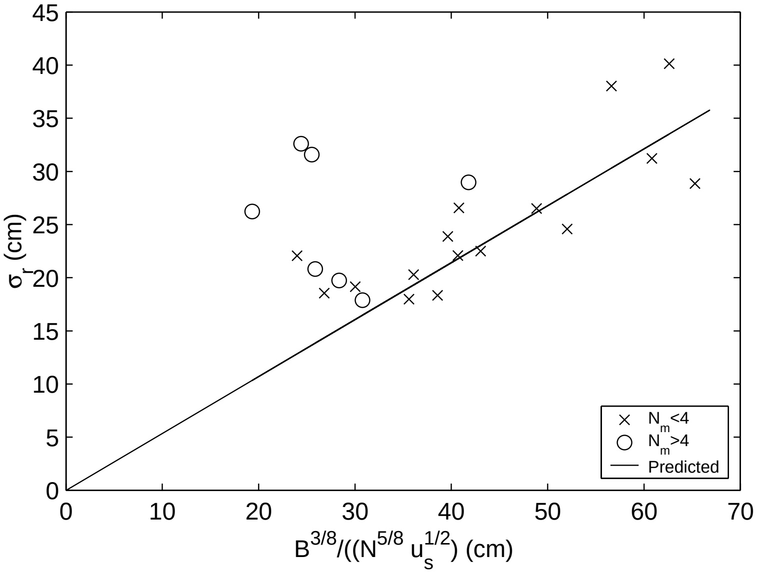

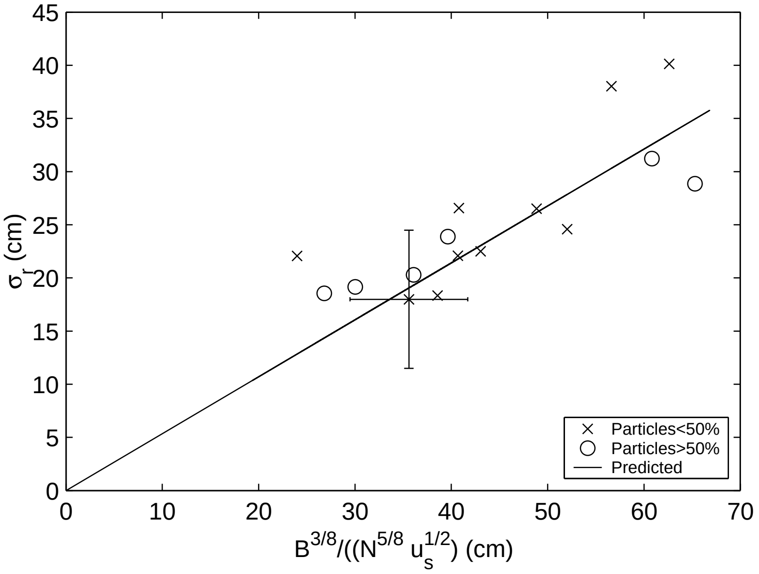

Figure 4-16: Plot of experimental radial sediment spread against $\frac{B^{3/8}}{N^{5/8}U_s^{1/2}}$, based on different experimental conditions. Predicted: $\sigma_r = \sqrt{\frac{c}{\pi}}\frac{B^{3/8}}{N^{5/8}U_s^{1/2}}$, with $c = 0.9$. Top: Effect of N_m on sediment radial spread. Bottom: Plot showing only runs with low initial momentum ($N_m < 4$). Typical error bars shown on bottom plot.

Well mixed intrusion layer

The estimated Peclet number, from Equation 2.46, was proportional to U_N and yielded values in the range of 20 to 40, which corresponded to the transitional regime between a well mixed model and a sediment plug flow (Dhamotharan et al. [22]). The radial sediment distributions obtained from the experiments were closer to Gaussian than to a constant radial concentration. This suggests that the sediment within the intrusion layers in the experiments were well mixed. The exponential decay in sediment fallout from the well mixed intrusion layer with time, combined with the outward advection of the sediment by the intrusion volume flux, resulted in a Gaussian radial distribution predicted in Equation 2.37.

Effect of bottom location

There was no clear trend between the bottom location and the resulting sediment spread, as shown in Figure 4-17. This supported the argument that the particles, after falling out of the intrusion layer that has advected them radially, traveled passively to the bottom, and that there were minimal particle-particle interactions which could have led to the formation of group effects such as lazy plumes.

Effect of initial momentum

The effect of increased momentum would give a plume higher velocity at every point compared to a point in the pure plume. More entrainment would occur, if the entrainment assumption for a dual-phase plume holds, which means a larger intrusion volume when inevitably the plume fluid peels. This results in a higher initial plume intrusion velocity which would propel the sediment further horizontally before allowing them to fall out of the peel layer. This may suggest the higher sediment spread at plume conditions with higher N_m compared to the pure plume, as shown in Figure 4-16.

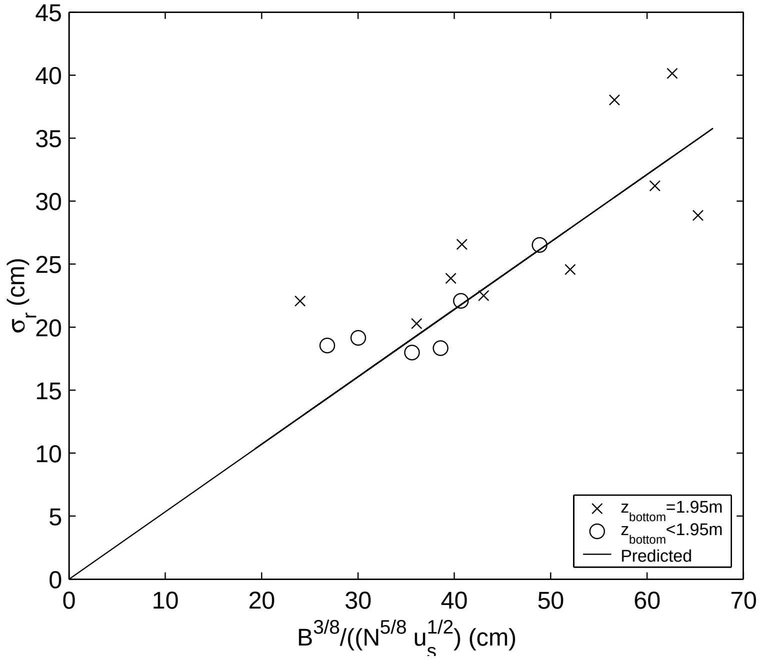

Figure 4-17: Plot of experimental radial sediment spread against $\frac{B^{3/8}}{N^{5/8}U_s^{1/2}}$. The data points are categorized based on location of the bottom collecting tray below the surface, z_{bottom}. Predicted: $\sigma_r = \sqrt{\frac{c}{\pi}}\frac{B^{3/8}}{N^{5/8}U_s^{1/2}}$, with $c = 0.9$.

4.6 Error analysis

Experimental error can be of three main types: measurement error, systemic error and random error. Measurement error depends on the resolution of the equipment and the repeatability of the measurement. Systemic errors, or bias, are due to calibration and observational errors, that are in principle constant and correctable. Finally, random error is caused by unbiased statistical scatter around the measured value, that can be determined by repeating the experiment a number of times.

4.6.1 Errors in measured quantities

Particle Flow Rate

The particle flow rate of glass beads was measured by weighing the flow of beads that land on an analytical balance after a known length of time. The measurement resolution of the scale was (±0.01 g) and the stopwatch (±0.01 s). The standard deviation of the flow rates, obtained for similar experimental conditions, were used as the error of particle flow rate. For polystyrene bead releases, since the beads were submerged before release, the flow rate was measured by timing the duration of the experiment, and weighing the final, dried particle mass left over in the dispensing bottle at the end of the experiment (often zero). This resulted in an average particle flowrate for the duration of the experiment. Several test runs of particle releases in the same manner of the experiments were performed, and the standard deviation of the flowrates were taken as the error for the polystyrene bead flow rate.

Brine Flow Rate

The brine flow rate was measured by measuring the volume leaving the dispensing Mariotte bottle for a timed period. The error was taken to be the standard deviation of the calculated flow rates, after performing the flow rate measurement several times.

Peel Depth

The peel depth measurement depended on the images acquired by the CCD camera and LIF technique. Each image measured 768 (vertical) x 484 (horizontal) pixels, and for most of the experiments covered a height of 1.75 m. This resulted in a measurement error of 0.2 cm. A way to characterize the measurement error in the peel depth measurement was to take the the standard deviation of the depths determined from the different frames within each experimental run images. This was shown to be typically ±2 cm.

Trap Depth

In the fluorometer profiles used to determine the trap depth, the concentration values were only used as to locate the vertical depth at which most of the dye was trapped. Random errors, sometimes with unreasonable (for example negative) temperature depth and fluorescence readings, occurred in situations where the fluorometer sample area contained some air, as was the case when the probe was just placed into the water surface, and they were removed from each profile.

Since each intrusion layer had a finite thickness, and the first moment of the fluorescence profiles were used to determine the trap depth, the error for the trap depth was taken to be the standard deviation of the profiles. For the presentation of data in Chapter 4, the experimental runs in which the standard deviation of the fluorometer profile exceeded 30% of the mean trap depth were omitted.

Sediment spread

The sediment spread, σ_r, was a fitted 2-D Gaussian standard deviation, of 144 different mass measurements at various horizontal coordinates. The center of the distribution and the variance were picked out so as to yield the least squares difference with the recorded sediment masses.

Some of the experimental radial distributions, though Gaussian in shape, appeared to have a different spread in different directions, suggesting an azimuthal variation. This may be due to the plume meandering, or the improper centering, or direction of the initial plume source. Or, it may be caused by the fact that the experiments were performed in a confined tank, potentially introducing secondary circulation, while the modeled physical scenario is an unconfined ambient. All of these factors would have caused a deviation of the resulting sediment distribution from a Gaussian or axisymmetric distribution.

The error can be estimated as the least square difference between the measured and Gaussian distribution, multiplied by the aspect ratio of the plot, since the horizontal variations were visually on the order of the vertical variations from the Gaussian curve. Figure 4-18 shows the estimation method in more detail, and Figure 4-19 plots the error for each experimental run.

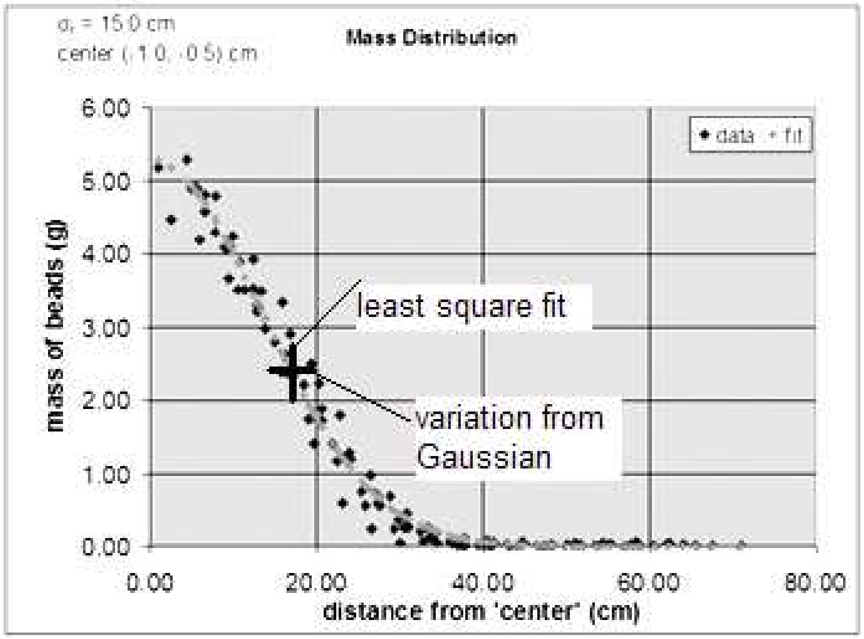

Figure 4-18: Method used to estimate error of σ_r. The dark vertical line represents the mean least square difference, obtained from fitting the Gaussian curve to the data. The horizontal variation is taken to be identical visually as the vertical variation, and thus the error in σ_r is obtained by multiplying by the aspect ratio of the plot.

4.6.2 Errors in calculated quantities

Errors in calculated quantities stem from the measured quantities: if a calculated quantity F, is calculated from n measurements, i.e.

$$F = f(x_1, x_2, ..., x_n), \tag{4.9}$$

then, with each error δx_n, the total error in F, δF, is calculated using the measurement error equation:

$$\delta F = \sqrt{\sum_{i=1}^{n} \left(\left(\frac{\partial f}{\partial x_i} \right) \delta x_i \right)^2} \tag{4.10}$$

The calculated quantities in an experiment are B_s the brine buoyancy flux, B_b, the particle buoyancy flux, N, u_s.

$$\delta N = \sqrt{\frac{g(\delta\rho)^2}{4\rho(\rho_1 - \rho_2)(z_1 - z_2)} + \frac{g(\rho_1 - \rho_2)(\delta z)^2}{4\rho(z_1 - z_2)^3}} \tag{4.11}$$

$$\delta B_b = \sqrt{\left(\frac{g(\rho - \rho_b)}{\rho}\delta Q_b\right)^2 + \left(\frac{gQ_b}{\rho}\delta \rho_b\right)^2} \tag{4.12}$$

Similarly for the brine flow,

$$\delta B_s = \sqrt{\left(\frac{g(\rho - \rho_s)}{\rho}\delta Q_s\right)^2 + \left(\frac{gQ_s}{\rho}\delta \rho_s\right)^2} \tag{4.13}$$

The propagated errors in each of these values are calculated for each experiment, and are shown in Table 4.6.2 Typical errors are shown in the Table 4.6.2. Also Figures 4-19 and 4-21 illustrate the errors for each data point.

Quantity	Mean	±	Error	
u_s	2E-03	±	3E-04	m/s
B_b	7.2E-07	±	2E-08	m^4/s^3
B_s	4.3E-06	±	2E-07	m^4/s^3
N	0.27	±	0.1	$1/s$

Table 4.3: Typical error of calculated values

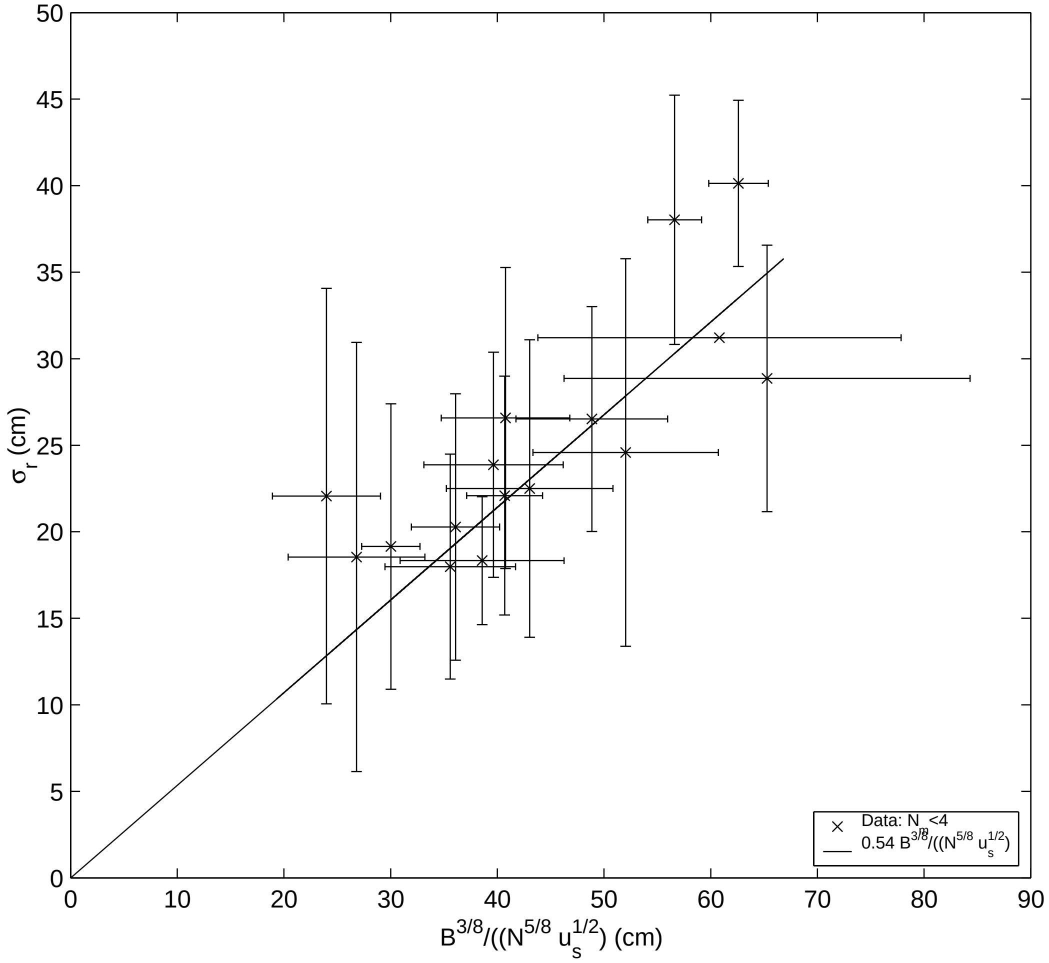

Figure 4-19: Plot of radial sediment spread, showing error bars for each data point.

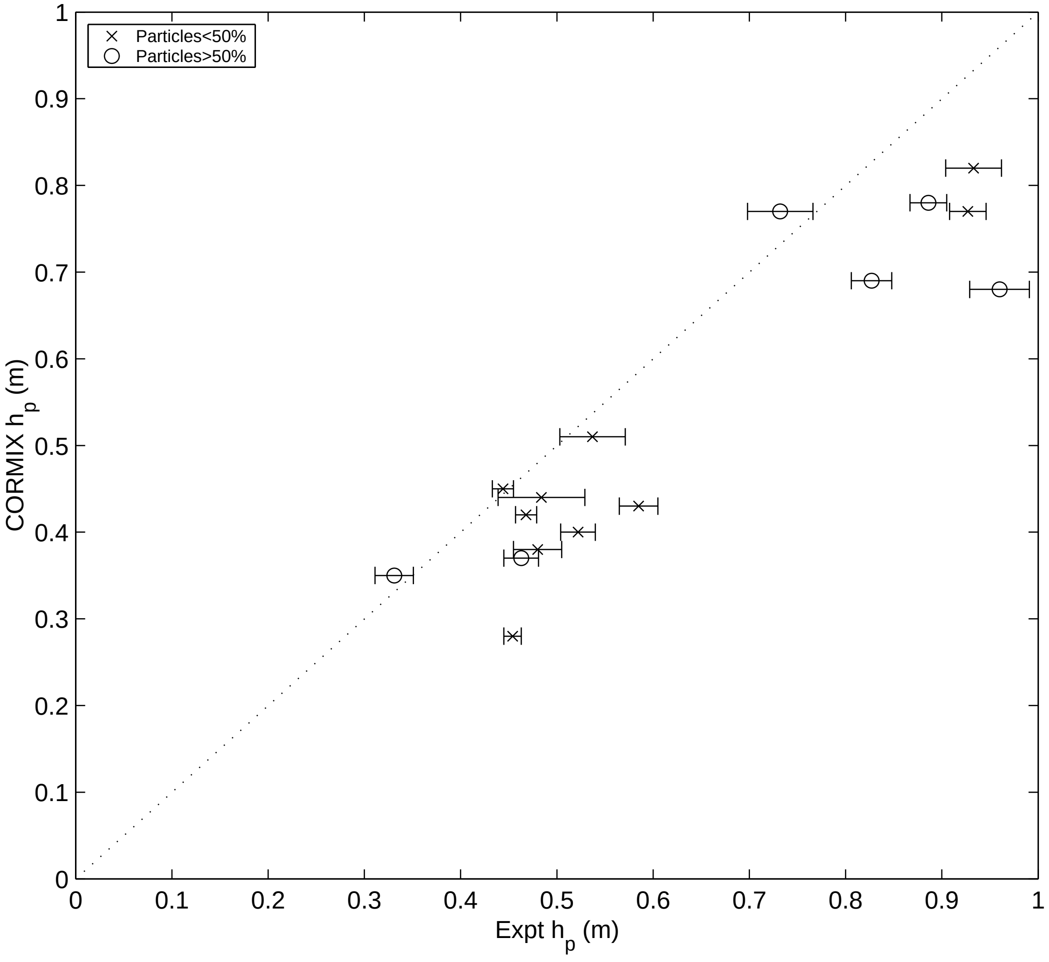

Figure 4-20: Plot of CORMIX simulation of the experimental runs against experimentally measured peel depths, showing error bars for each data point. Only one of the three models is presented here for clarity.

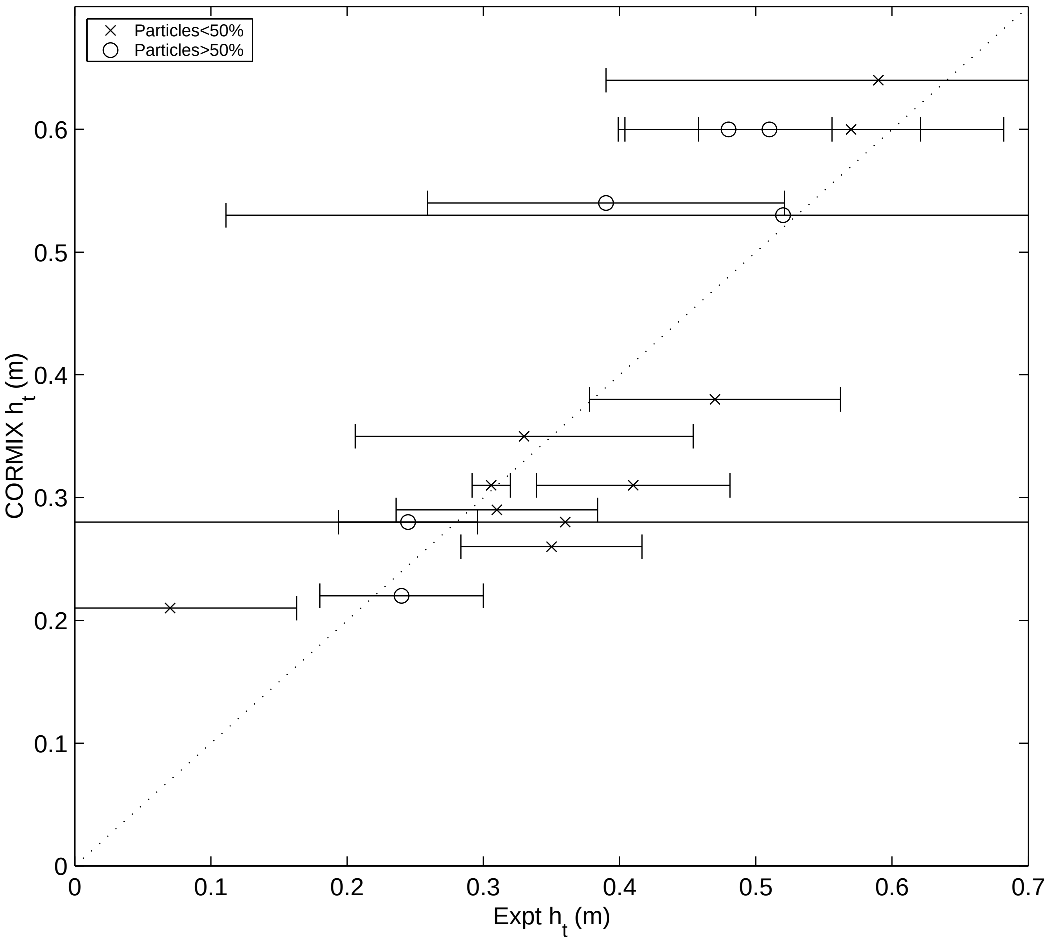

Figure 4-21: Plot of CORMIX simulation of the experimental runs against experimentally measured trap depths, showing error bars for each data point. Only one of the three models is presented here for clarity.

Slip Velocity

An empirical relation (Equation 3.6) is used to relate slip velocity to the diameter and density of the particles used. Assuming negligible error of the equation itself and of the density, the source of error will be from the particle diameters. To apply Equation 4.10 for the slip velocity relation would be too lengthy. Therefore the error was estimated by applying Equation 3.6 to each size distribution obtained by sieve analysis, and in particular to diameters one standard deviation from the mean diameter used. The resulting slip velocity errors were shown earlier in Chapter 4, Table 4.6.2.

Run	u_s (m/s)	δu_s (m/s)	B_b (m^4/s^3)	δB_b (m^4/s^3)	B_s (m^4/s^3)	δB_s (m^4/s^3)	N (1/s)	δN
040503	4.91E-03	2.43E-03	3.4E-05	8.2E-08	0.0E+00	NA	0.33	0.10
042203	4.91E-03	2.43E-03	1.7E-05	4.8E-08	1.4E-05	6.6E-07	0.27	0.09
041803	4.91E-03	2.43E-03	5.8E-16	NA	3.4E-05	5.9E-07	0.28	0.09
120503	6.26E-03	5.50E-04	1.3E-05	3.9E-08	1.6E-05	3.6E-07	0.27	0.003
121003	6.26E-03	5.50E-04	1.5E-05	4.3E-08	2.3E-05	4.5E-07	0.27	0.003
071603	2.08E-03	3.02E-04	1.4E-06	5.7E-08	0.0E+00	NA	0.29	0.10
072803	2.09E-03	3.03E-04	1.4E-06	5.1E-08	1.9E-06	3.7E-07	0.31	0.08
081103	2.10E-03	3.04E-04	1.7E-07	9.5E-09	7.1E-07	2.1E-07	0.32	0.13
081903	2.18E-03	3.15E-04	6.4E-07	1.8E-08	0.0E+00	NA	0.36	0.08
082103	2.02E-03	2.94E-04	7.2E-07	2.1E-08	4.3E-06	2.7E-07	0.27	0.09
082903	2.04E-03	2.96E-04	7.0E-07	4.2E-08	2.2E-06	5.1E-07	0.26	0.09
090303	2.04E-03	2.97E-04	5.4E-07	1.4E-08	2.7E-06	2.5E-07	0.29	0.08
091703	2.19E-03	3.16E-04	7.8E-07	3.2E-08	1.7E-07	4.1E-07	0.27	0.10
091903	2.07E-03	3.00E-04	7.7E-07	1.9E-08	0.0E+00	NA	0.26	0.08
092303	1.98E-03	2.87E-04	8.7E-07	2.4E-08	0.0E+00	NA	0.25	0.09
100103	2.11E-03	3.05E-04	1.0E-07	4.0E-09	5.8E-06	1.3E-06	0.32	0.07
100803	2.13E-03	3.09E-04	1.0E-07	4.8E-09	2.3E-06	5.4E-07	0.30	0.09
101503	2.08E-03	3.01E-04	1.0E-07	4.9E-09	2.3E-06	5.7E-07	0.28	0.10
111203	2.20E-03	3.18E-04	5.5E-07	3.3E-08	1.8E-07	5.2E-07	0.26	0.01
111703	2.12E-03	3.07E-04	6.1E-07	1.2E-08	1.9E-07	1.4E-07	0.27	0.005
111903	2.13E-03	3.08E-04	9.3E-07	2.5E-08	3.3E-07	1.8E-07	0.27	0.003
112203	2.11E-03	3.05E-04	7.6E-07	2.0E-08	2.3E-06	3.9E-07	0.29	0.00
071403	2.13E-03	3.09E-04	4.4E-17	NA	3.8E-06	7.7E-07	0.27	0.01
042103	1.22E-02	2.15E-03	2.4E-05	5.9E-08	NA	3.9E-07	0.30	0.05
042503	1.22E-02	2.15E-03	1.4E-05	4.1E-08	1.1E-05	3.4E-07	0.26	0.08
050103	1.22E-02	2.15E-03	5.8E-16	NA	2.5E-05	4.7E-07	0.29	0.07

Table 4.4: Detailed error in measured quantities for each experiment

Chapter 5

Conclusions and Further Work

5.1 Conclusions

The effect of initial buoyancy composition on the resulting plume trap and peeling depths for negatively buoyant plumes was studied experimentally, and compared with numerical predictions of three different models, all of which captured the physics of the flow in some ways. Several experimental conditions such as the initial momentum, and the variability in the determination of the trap depth, also affected the measurements of the depths of interest.

It was hypothesized that, since $U_N << 1$, the plumes initially behaved as single phase plumes, and as a result the peeling depth was unaffected by the buoyancy composition. This observation was confirmed in the experiments, by comparing them to single phase plumes, and other models. The numerical models were also used to determine whether initial momentum and volume flux will significantly affect peel and trap depths, using two parameters N_m and N_q.

Qualitatively, the higher the buoyancy due to fine suspended particles (with $U_N << 1$), the smaller the trapping depth, since the particles upon leaving the intrusion layer will make the intrusion positively buoyant (similar to the lift-off phenomenon observed in sediment-laden gravity currents). Generally this prediction was also confirmed in the experiments.

The prediction of the sediment radial distribution vertically downstream of the intrusion was made by modeling the radially spreading intrusion layer as both a vertically descending plug flow and as a well mixed sedimenting layer. For the latter case, it is argued that a radial Gaussian distribution will result. This was confirmed by the experimental measurements of final bottom sediment distributions, implying a well-mixed intrusion layer depositing the sediment to the bottom. The standard deviation of the distribution was predicted as a function of the total initial buoyancy, B, the stratification buoyancy N and the particle slip velocity u_s, namely

$$\sigma_r = \sqrt{\frac{c}{\pi}} \left(\frac{B^3}{N^5} \right)^{1/8} \frac{1}{u_s^{1/2}} \tag{5.1}$$

with $c = 0.9$, based on Socolofsky's [52] prediction of intrusion layer volume flux. Experiments showed a good agreement with Equation 5.1.

5.2 Further Work

While a small trend was established between the final trapping layer depth, and the composition of the buoyancy of the release, further work may involve developing a theory to predict the magnitude of the 'lift-off' effect, directly as a function of buoyancy, and the fraction and relative densities of the particle and continuous phase. The intrusion layer, upon losing its sediment and becoming positively buoyant, may be viewed simply as a large distributed (or lazy) plume, with positive buoyancy equal to the initial bead buoyancy. In this regard, lazy plumes could be further applicable to the study of the sediment-laden flow.

Also, a critical U_N value where particles will begin to travel radially outwards, advected readily by the plume fluid, can be investigated. This may be useful in determining fractionation of different particle sizes by an intrusion that is spreading radially in quiescent situations.

Appendix A

Experimental Raw Data

This section presents in detail the figures and data used for each of the 26 experiments used in the analysis. Each of the experimental runs detail the following:

- Density profile (raw and moving average)
- Stratification parameter or Brunt-Väisälä frequency N
- Buoyancy source
- Selection of pictures from the movie, showing peel height estimates
- Fluorometer profiles, and the trap depth estimate
- Plot of sediment radial mass distribution, and resulting estimate for the spread, σ_r.

A.1 Index of Figures for Experiments

Figures and Tables	Experiment number	Page(s)
Figure A-4 Table A.2 Figure A-5	040503	118-119
Figure A-6 Table A.3 Figure A-7	042203	120-121
Figure A-8 Table A.4 Figure A-9	041803	122-123
Table A.5 Figure A.1.1	120503	124
Table A.6 Figure A.1.1	121003	125
Figure A-12 Table A.7 Figure A-13	071603	126-127
Figure A-14 Table A.8 Figure A-15	072803	128-129
Figure A-16 Table A.9 Figure A-17	081103	130-131
Figure A-18 Table A.10 Figure A-19	081903	132-133
Figure A-20 Table A.11 Figure A-21	082103	134-135
Figure A-22 Table A.12 Figure A-23	082903	136-137
Figure A-24 Table A.13 Figure A-25	090303	138-139
Figure A-26 Table A.14 Figure A-27	091703	140-141
Figure A-28 Table A.15 Figure A-29	091903	142-143
Figure A-30 Table A.16 Figure A-31	092303	144-145
Figure A-32 Table A.17 Figure A-33	100103	146-147
Figure A-34 Table A.18 Figure A-35	100803	148-149
Figure A-36 Table A.19 Figure A-37	101503	150-151
Figure A-38 Table A.20 Figure A-39	111203	152-153
Figure A-40 Table A.21 Figure A-41	111703	154-155
Figure A-42 Table A.22 Figure A-43	111903	156-157
Figure A-44 Table A.23 Figure A-45	112203	158-159
Figure A-46 Table A.24 Figure A-47	071403	160-161
Figure A-48 Table A.25 Figure A-49	042103	162-163
Figure A-50 Table A.26 Figure A-51	042503	164-165
Figure A-52 Table A.27 Figure A-53	050103	166-167

Table A.1: Index of experimental figures.

A.1.1 Graphical Index of Experiments

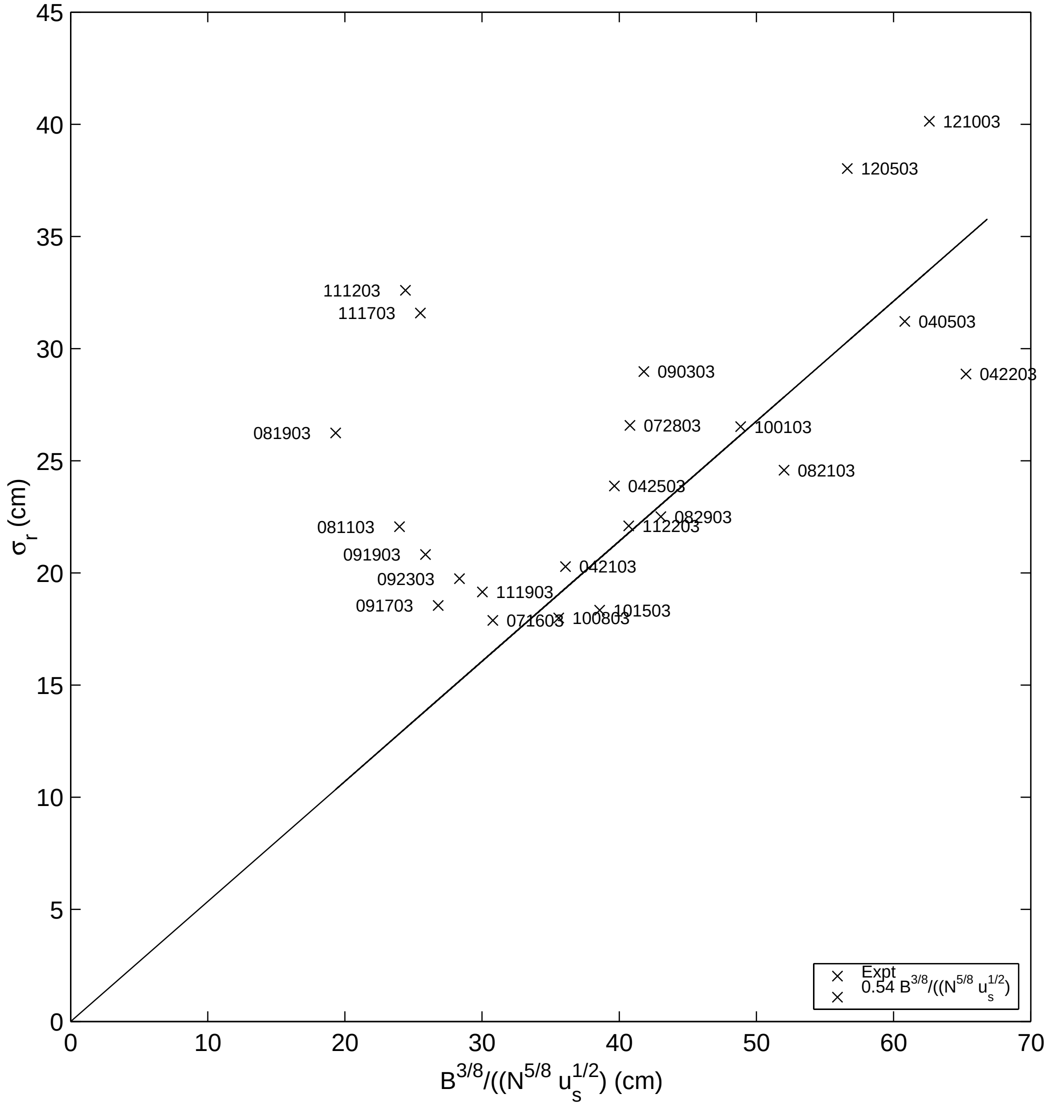

Figure A-1: Plot of σ_r against $\frac{B^{3/8}}{N^{5/8}u_s^{1/2}}$, labeled by experimental run number.

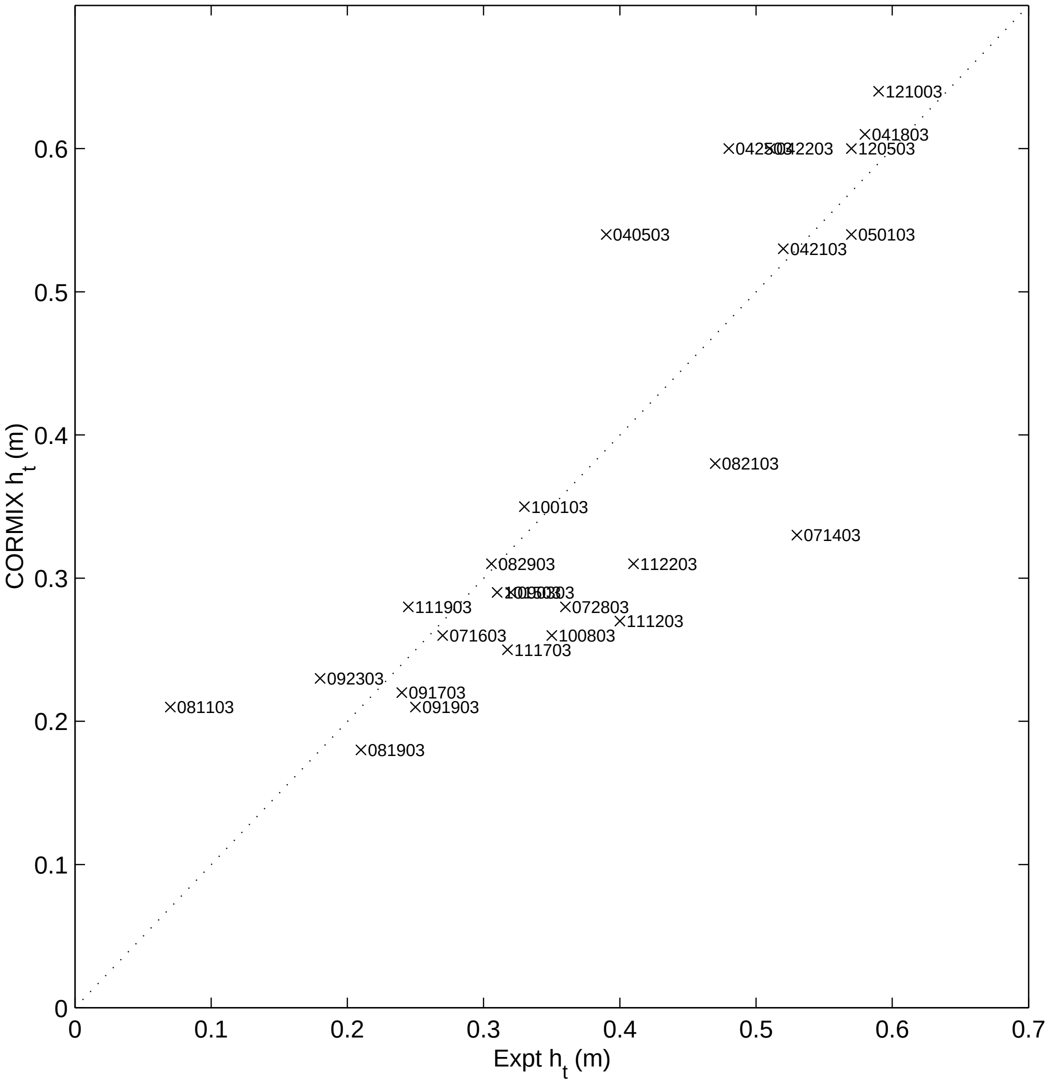

Figure A-2: Plot of h_t against $l_c = \left(\frac{B}{N^3}\right)^{1/4}$, labeled by experimental run number.

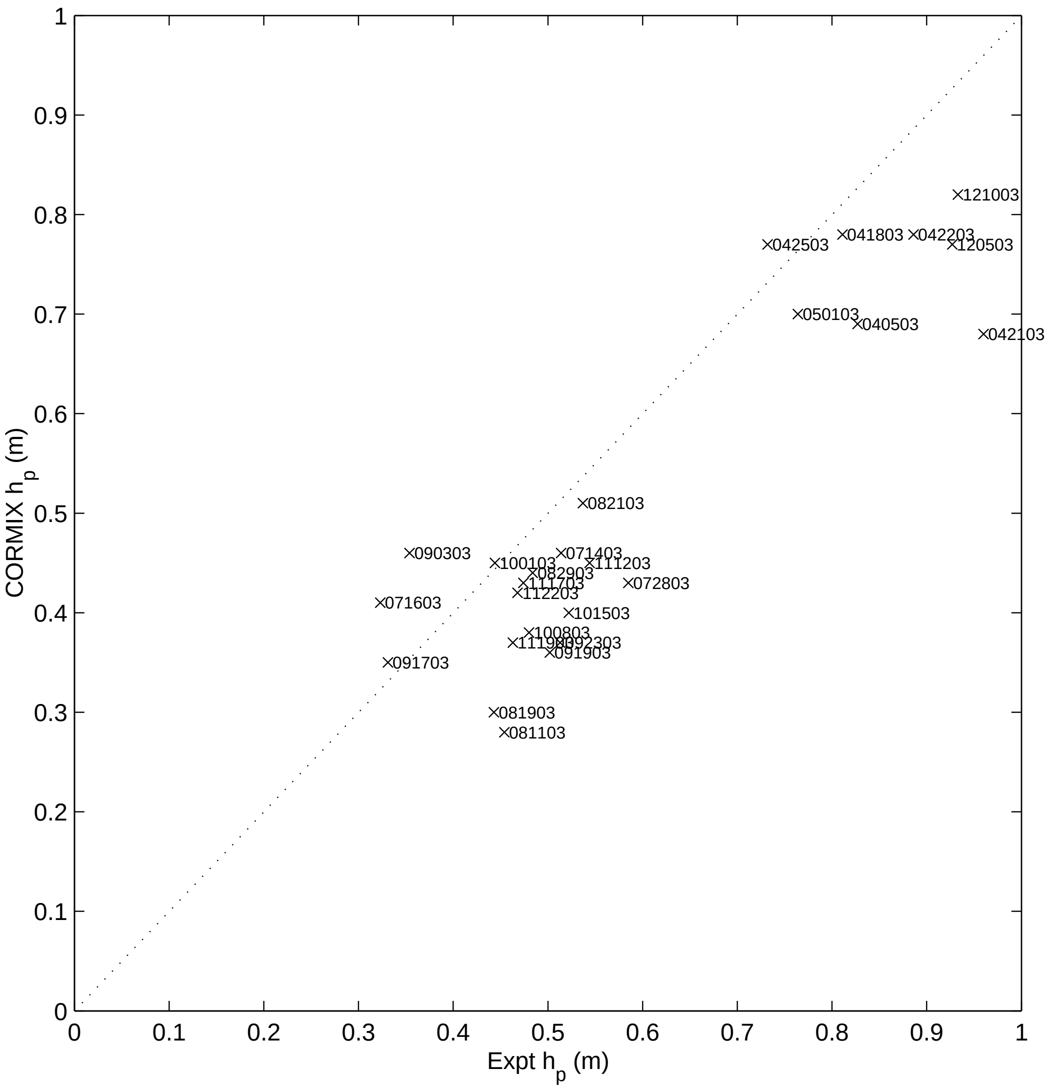

Figure A-3: Plot of h_p against $l_c = \left(\frac{B}{N^3}\right)^{1/4}$, labeled by experimental run number.

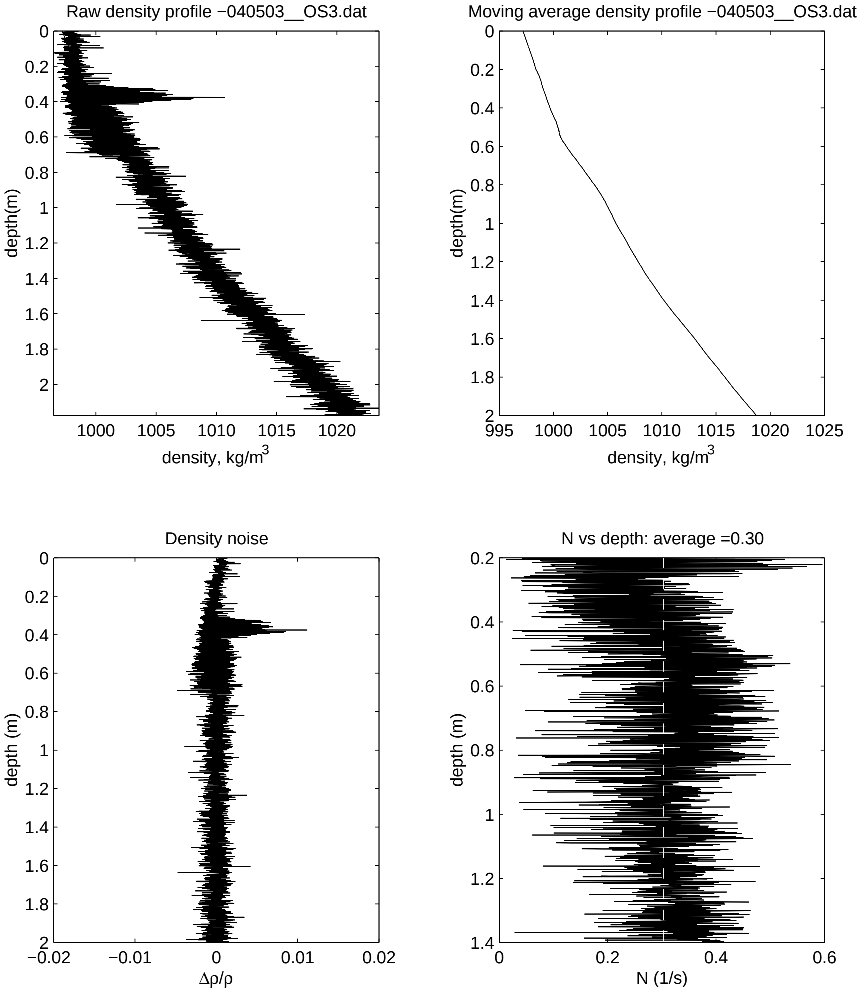

Figure A-4: Density profile for run 040503. Top left: raw density profile. Top right: moving average profile. Bottom left: Density difference between measured and average. Bottom right: Brunt-Väisälä frequency N from data

Run no.		**Time to empty (s)**	**Flow (g/s)**	**Source d (cm)**	**Source depth (m)**	**Bottom depth (m)**	**T** ^oC	S_0 **(g/kg)**	S **(g/kg)**
040503	AH	NA	5.89	**2.5**	**0.29**	1.95	17.0	0.0	0.0

Table A.2: Experimental conditions

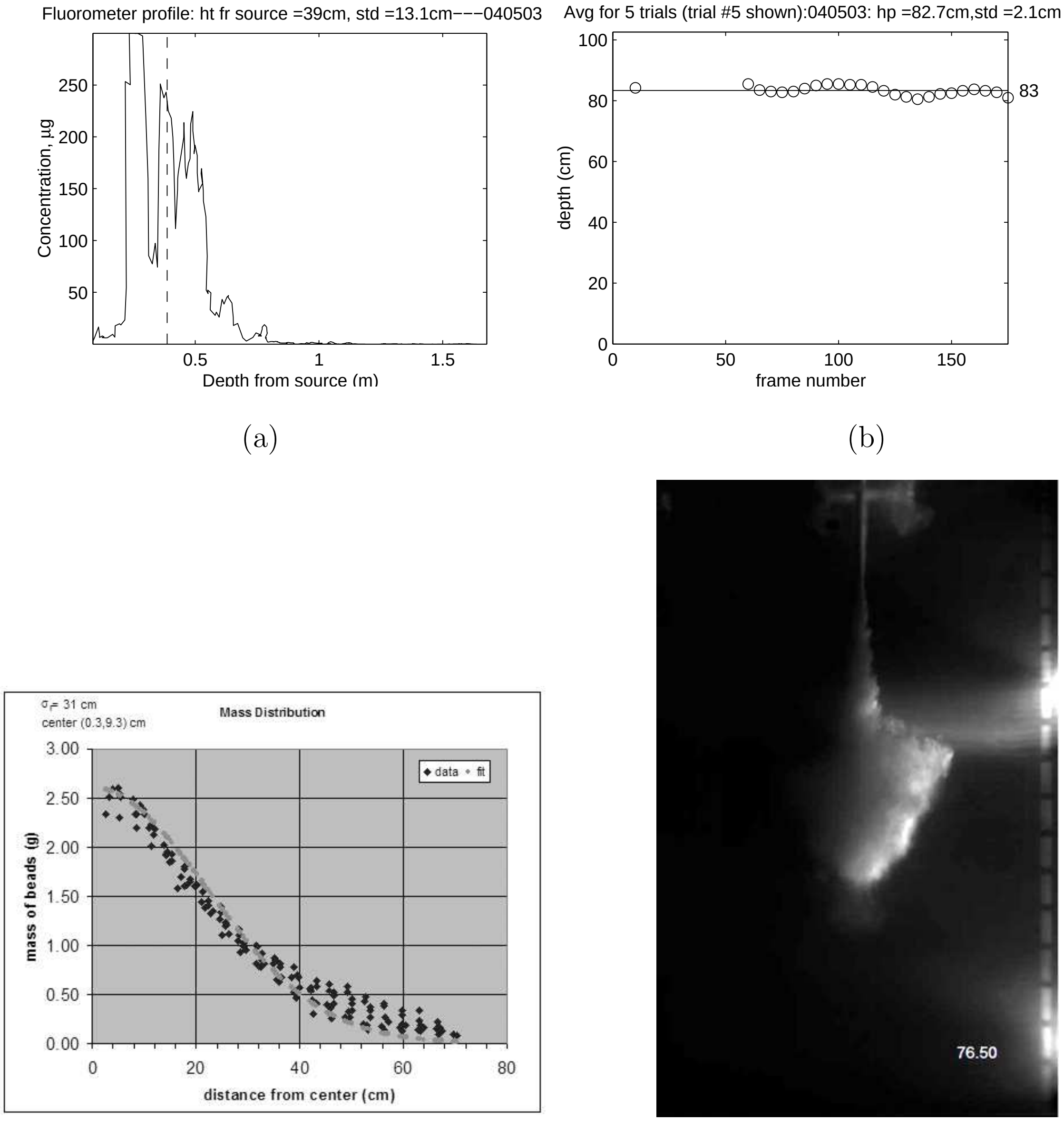

(a) (b)

(c) (d)

Figure A-5: Experimental run 040503: a) Fluorometer profile showing h_t, (b) Peel depths picked at various movie frames, with h_p shown for one example trial, (c) Sediment mass distribution and (d) One image from the experimental run.

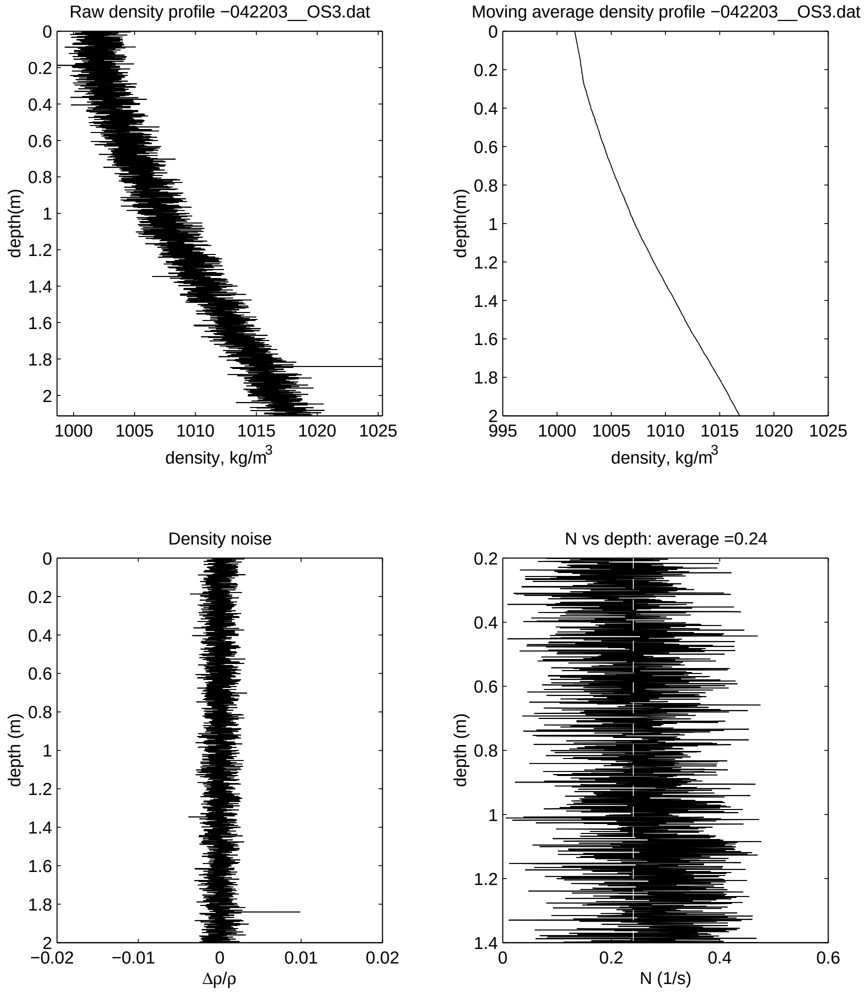

Figure A-6: Density profile for run 042203. Top left: raw density profile. Top right: moving average profile. Bottom left: Density difference between measured and average. Bottom right: Brunt-Väisälä frequency N from data

Run no.		**Time to empty (s)**	**Flow (g/s)**	**Source d (cm)**	**Source depth (m)**	**Bottom depth (m)**	**T** ^oC	S_0 **(g/kg)**	S **(g/kg)**
042203	AH	NA	2.90	**2.5**	**0.29**	1.95	17.0	0.0	36.0

Table A.3: Experimental conditions

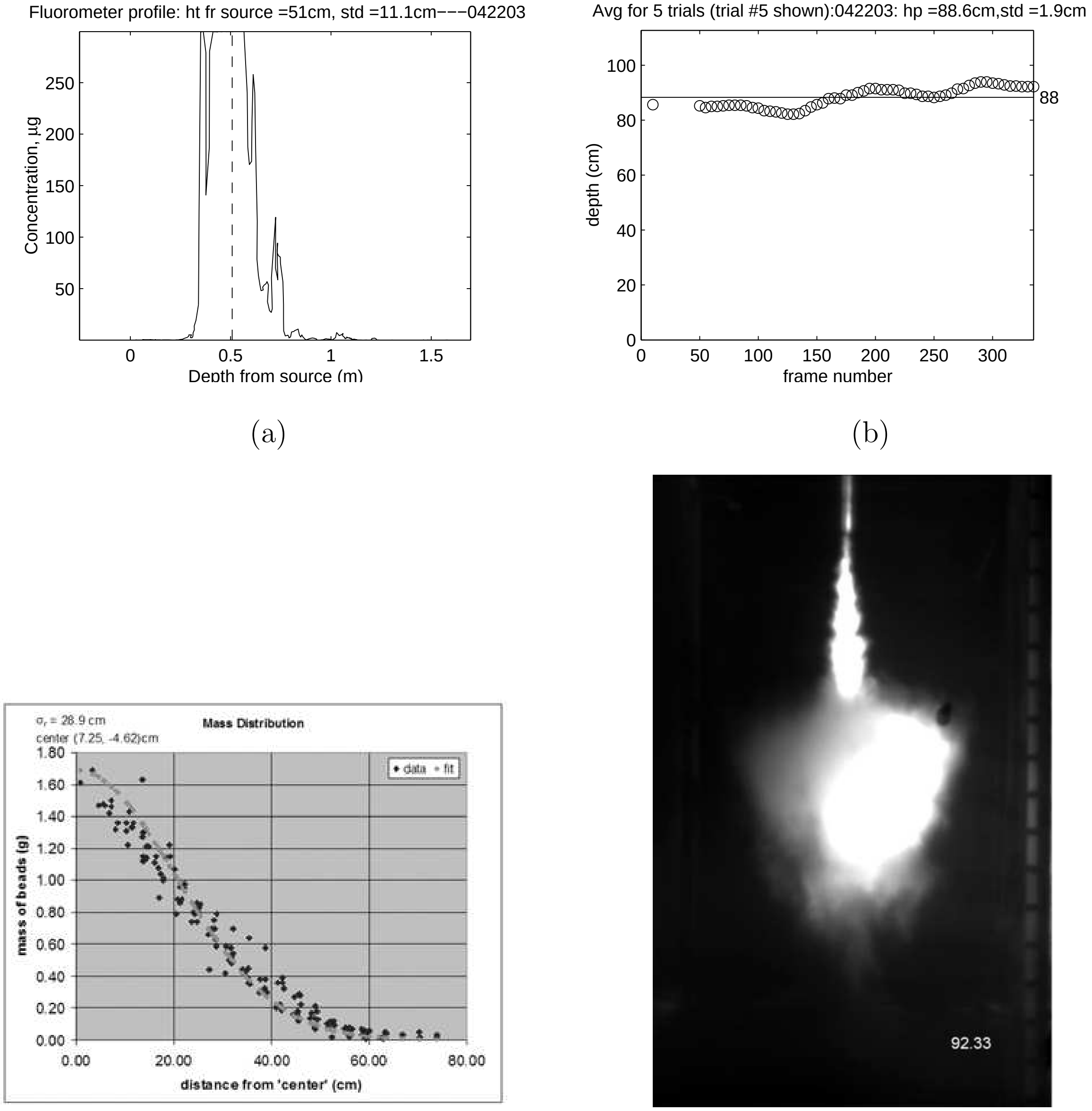

(a) (b)

(c) (d)

Figure A-7: Experimental run 042203: a) Fluorometer profile showing h_t, (b) Peel depths picked at various movie frames, with h_p shown for one example trial, (c) Sediment mass distribution and (d) One image from the experimental run.

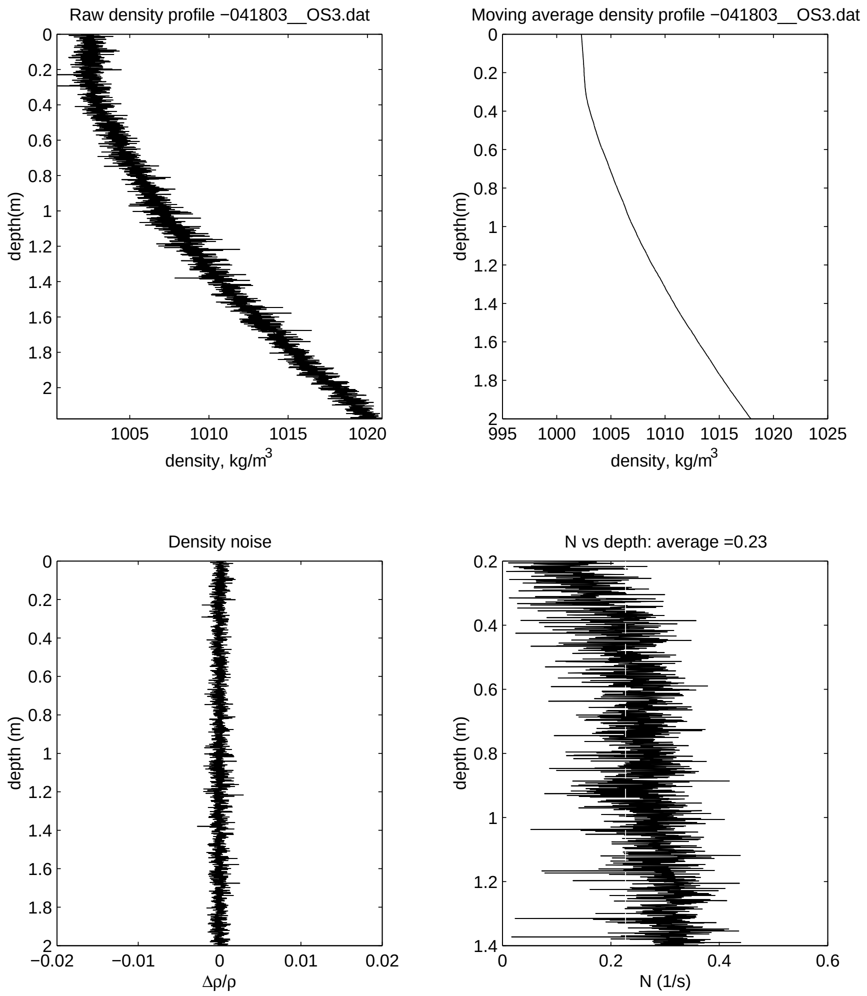

Figure A-8: Density profile for run 041803. Top left: raw density profile. Top right: moving average profile. Bottom left: Density difference between measured and average. Bottom right: Brunt-Väisälä frequency N from data

Run no.		**Time to empty (s)**	**Flow (g/s)**	**Source d (cm)**	**Source depth (m)**	**Bottom depth (m)**	**T** ^oC	S_0 **(g/kg)**	S **(g/kg)**
041803	AH	NA	0.00	**2.5**	**0.29**	1.95	17.0	0.0	88.7

Table A.4: Experimental conditions

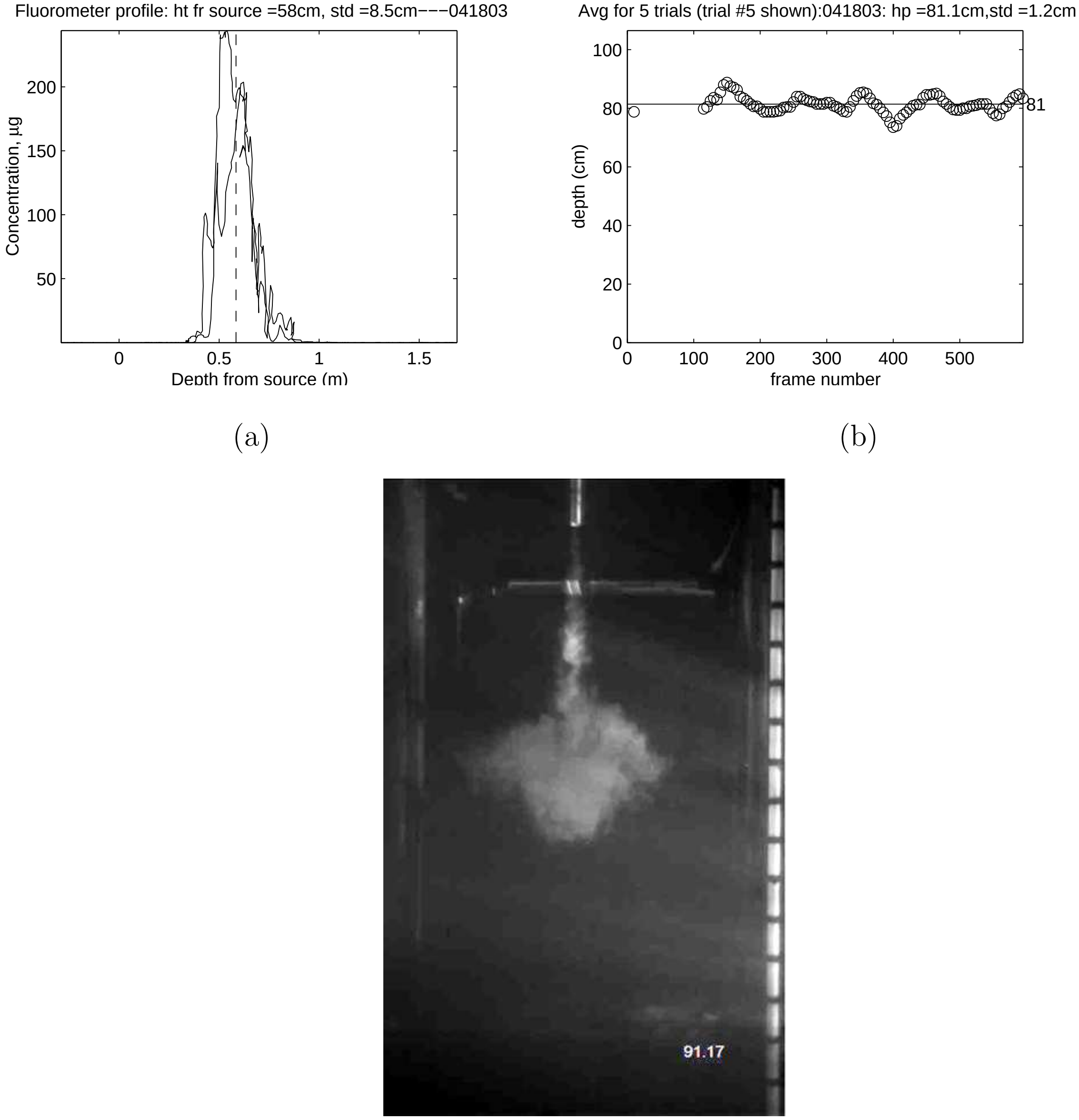

(a) (b)

(c)

Figure A-9: Experimental run 041803: a) Fluorometer profile showing h_t, (b) Peel depths picked at various movie frames, with h_p shown for one example trial, (c) One image from the experimental run.

Note: The density profile used for this run and run 121003 was the same as that used for 112203. (Experiment run after 112203)

Run no.		**Time to empty (s)**	**Flow (g/s)**	**Source d (cm)**	**Source depth (m)**	**Bottom depth (m)**	**T** ^oC	S_0 **(g/kg)**	S **(g/kg)**
120503	AH88	292	2.19	**2.5**	**0.19**	1.95	20.7	5.3	50.0

Table A.5: Experimental conditions

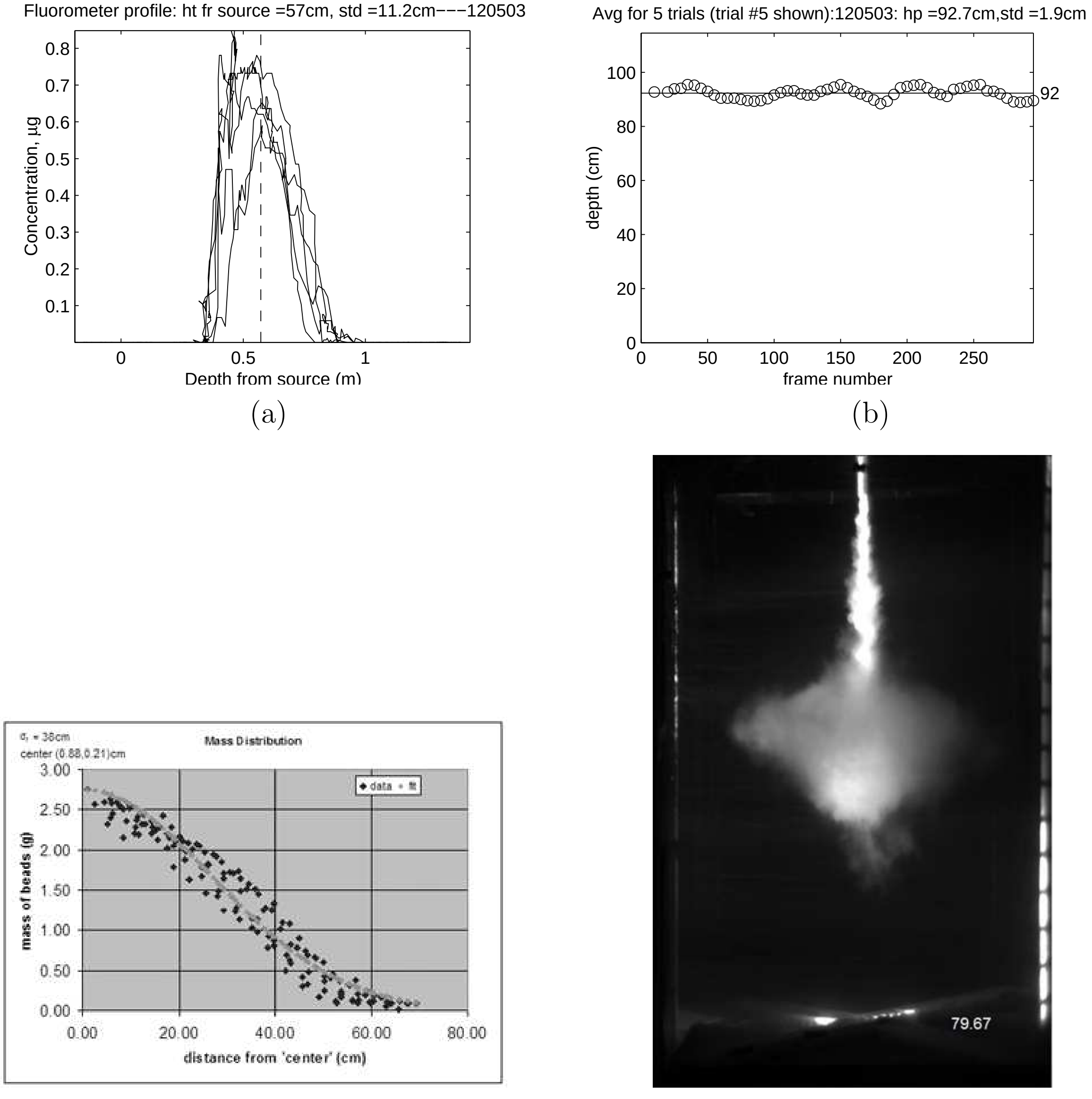

(a) (b)

(c) (d)

Figure A-10: Experimental run 120503: a) Fluorometer profile showing h_t, (b) Peel depths picked at various movie frames, with h_p shown for one example trial, (c) Sediment mass distribution and (d) One image from the experimental run.

Note: The density profile used for this run and run 120503 was the same as that used for 112203. (Experiment run after 112203)

Run no.		Time to empty (s)	Flow (g/s)	Source d (cm)	Source depth (m)	Bottom depth (m)	T ^oC	S_0 (g/kg)	S (g/kg)
121003	AH88	216	2.59	**2.5**	**0.19**	1.95	20.7	5.1	70.0

Table A.6: Experimental conditions

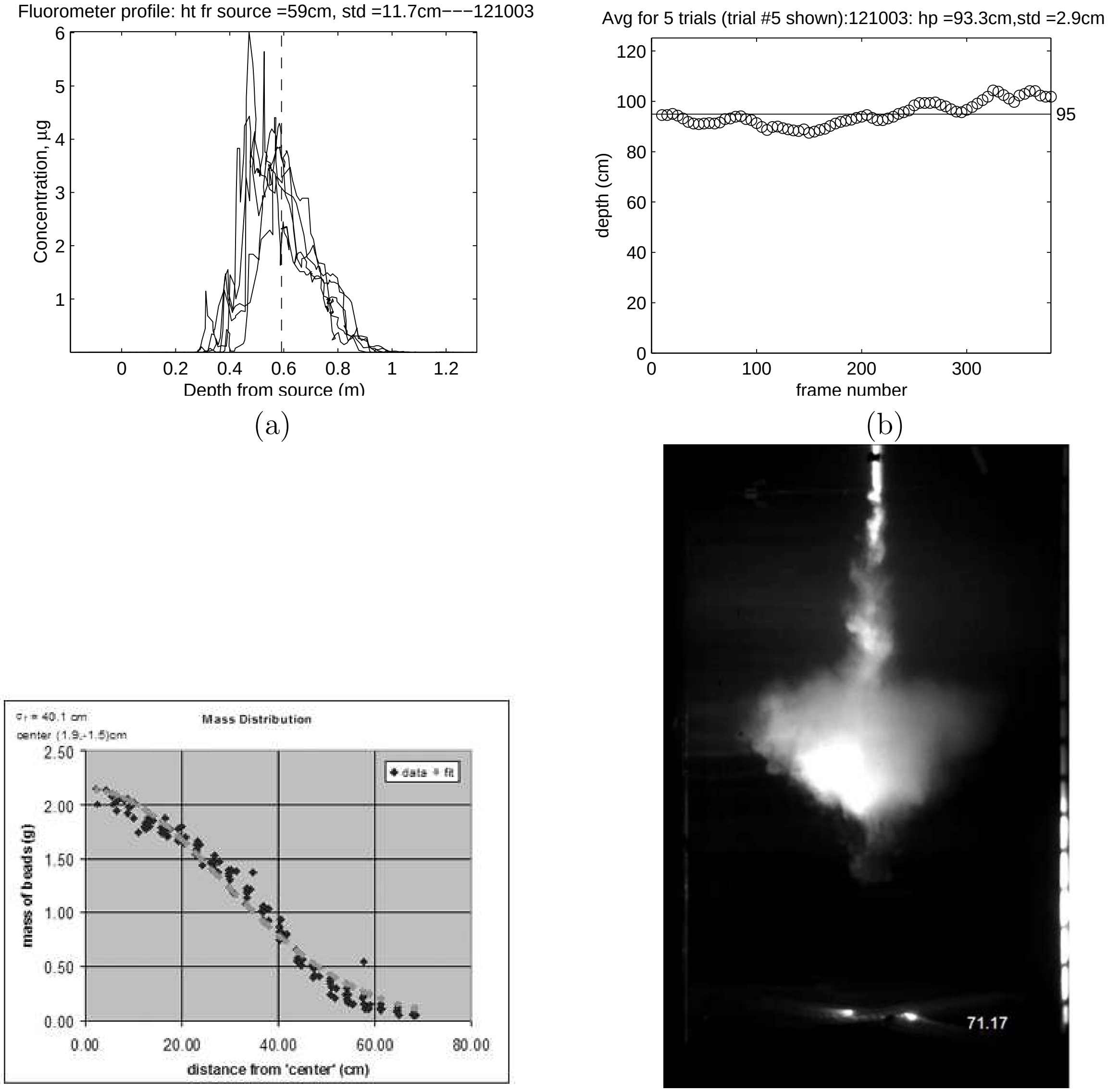

(a) (b)

(c) (d)

Figure A-11: Experimental run 121003: a) Fluorometer profile showing h_t, (b) Peel depths picked at various movie frames, with h_p shown for one example trial, (c) Sediment mass distribution and (d) One image from the experimental run.

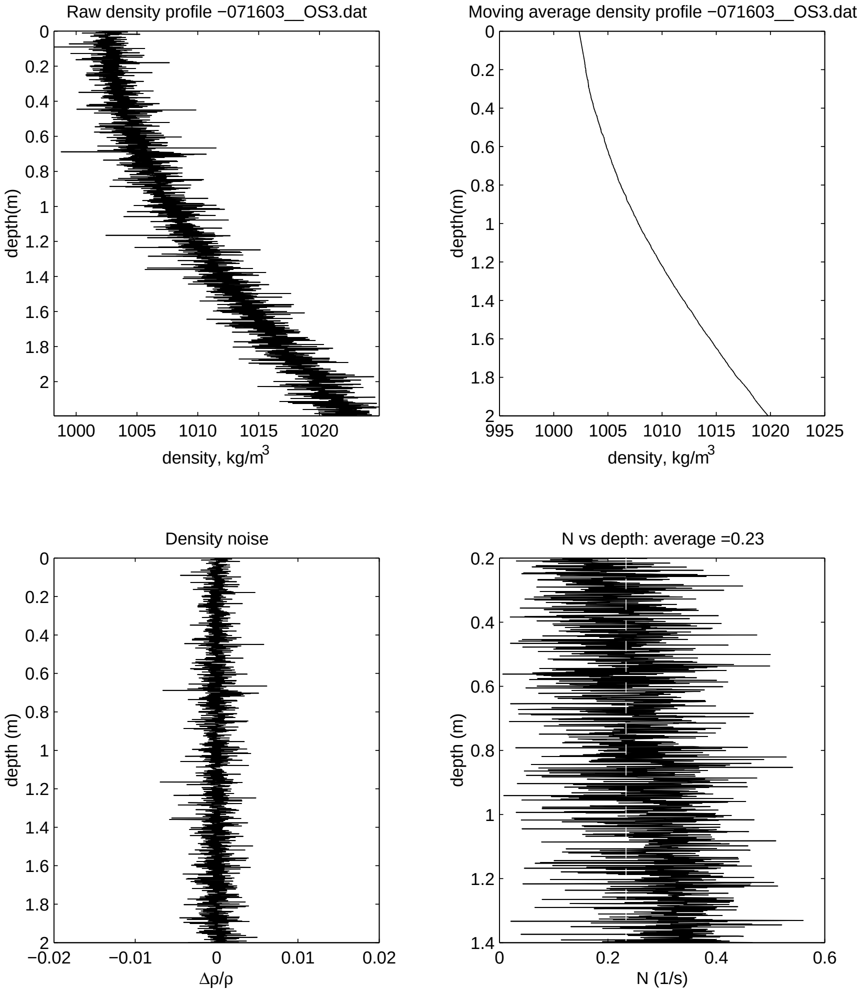

Figure A-12: Density profile for run 071603. Top left: raw density profile. Top right: moving average profile. Bottom left: Density difference between measured and average. Bottom right: Brunt-Väisälä frequency N from data

Run no.		**Time to empty (s)**	**Flow (g/s)**	**Source d (cm)**	**Source depth (m)**	**Bottom depth (m)**	**T** ^oC	S_0 **(g/kg)**	S **(g/kg)**
071603	PS	180	3.33	**0.8**	**0.27**	1.95	22.8	8.5	8.5

Table A.7: Experimental conditions

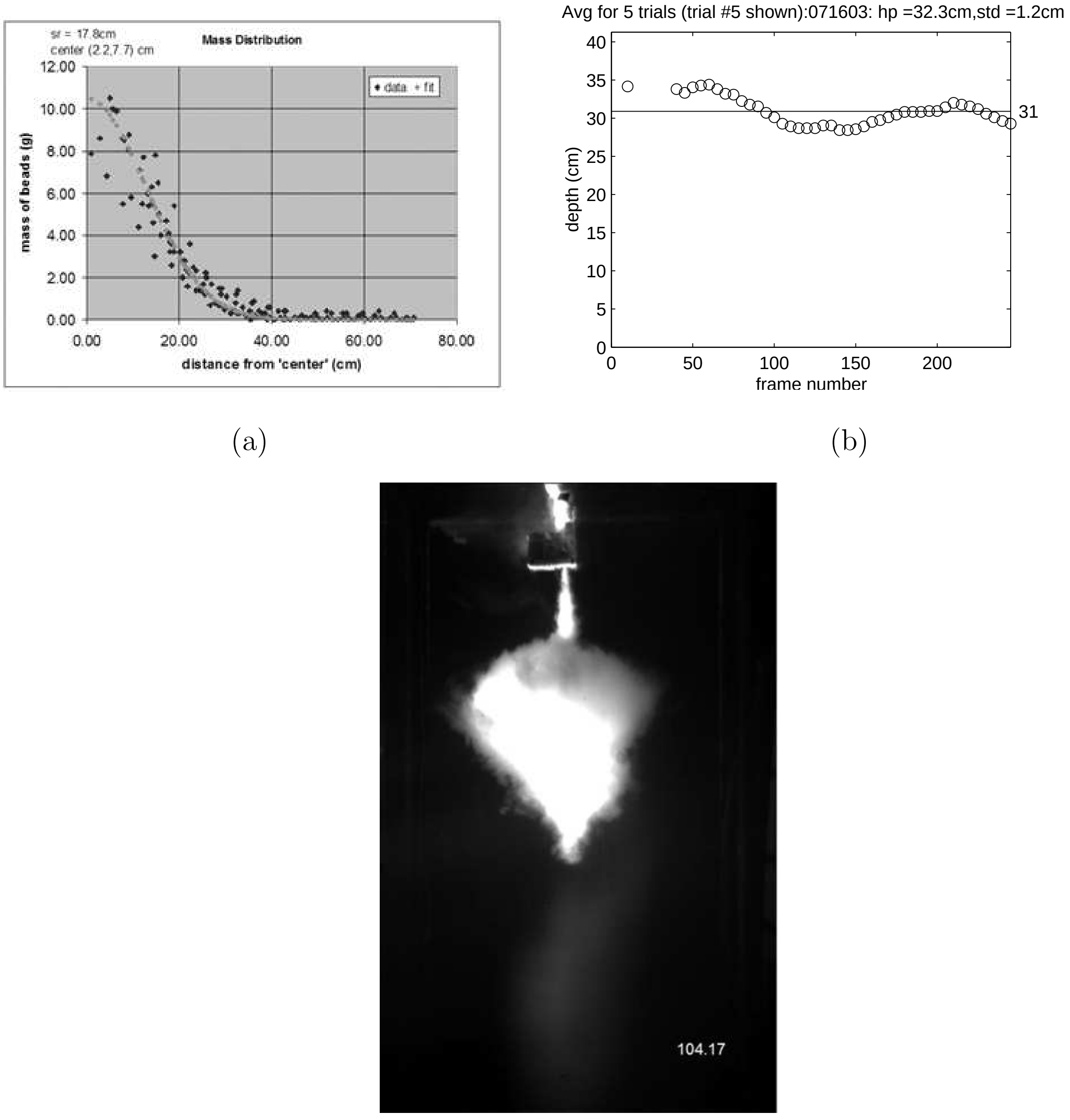

(a)

(b)

(c)

Figure A-13: Experimental run 071603: a) Sediment radial distribution, (b) Peel depths picked at various movie frames, with h_p shown for one example trial, (c) One image from the experimental run. Fluorometer profile was not available, h_t determined from ruler measurements at the time of the experiment

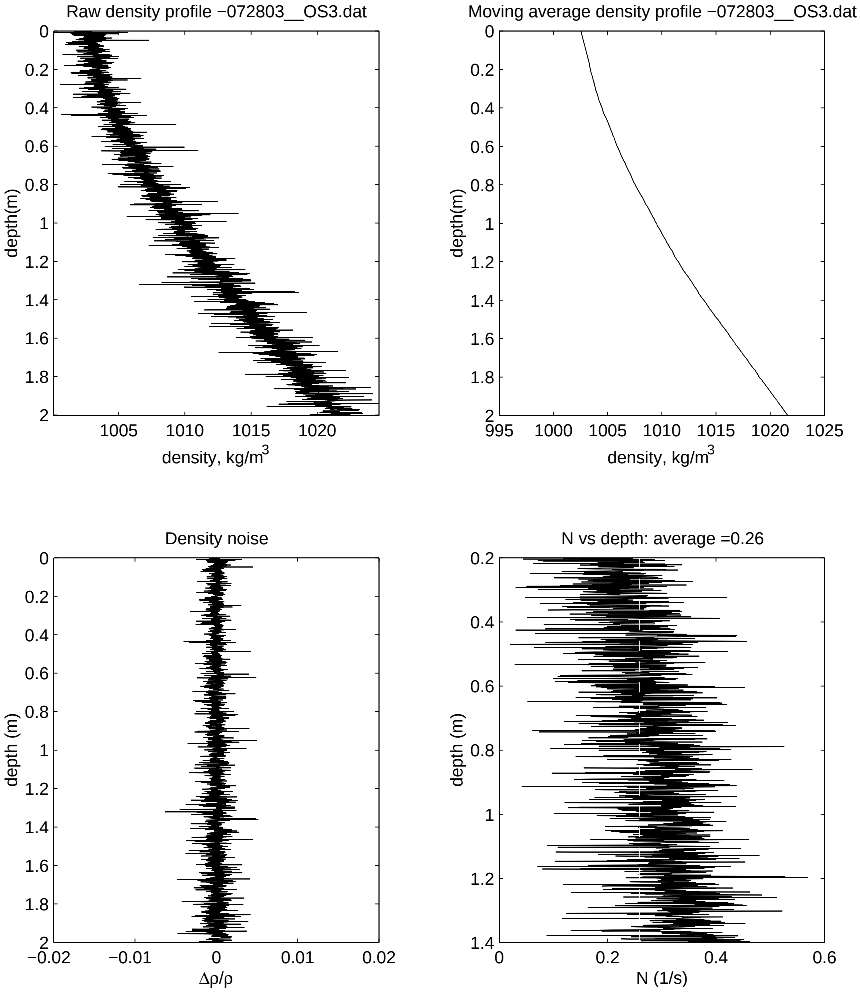

Figure A-14: Density profile for run 072803. Top left: raw density profile. Top right: moving average profile. Bottom left: Density difference between measured and average. Bottom right: Brunt-Väisälä frequency N from data

Run no.		**Time to empty (s)**	**Flow (g/s)**	**Source d (cm)**	**Source depth (m)**	**Bottom depth (m)**	**T** ^oC	S_0 **(g/kg)**	S **(g/kg)**
072803	PS	180	3.33	**0.8**	**0.27**	1.95	23.3	8.4	15.5

Table A.8: Experimental conditions

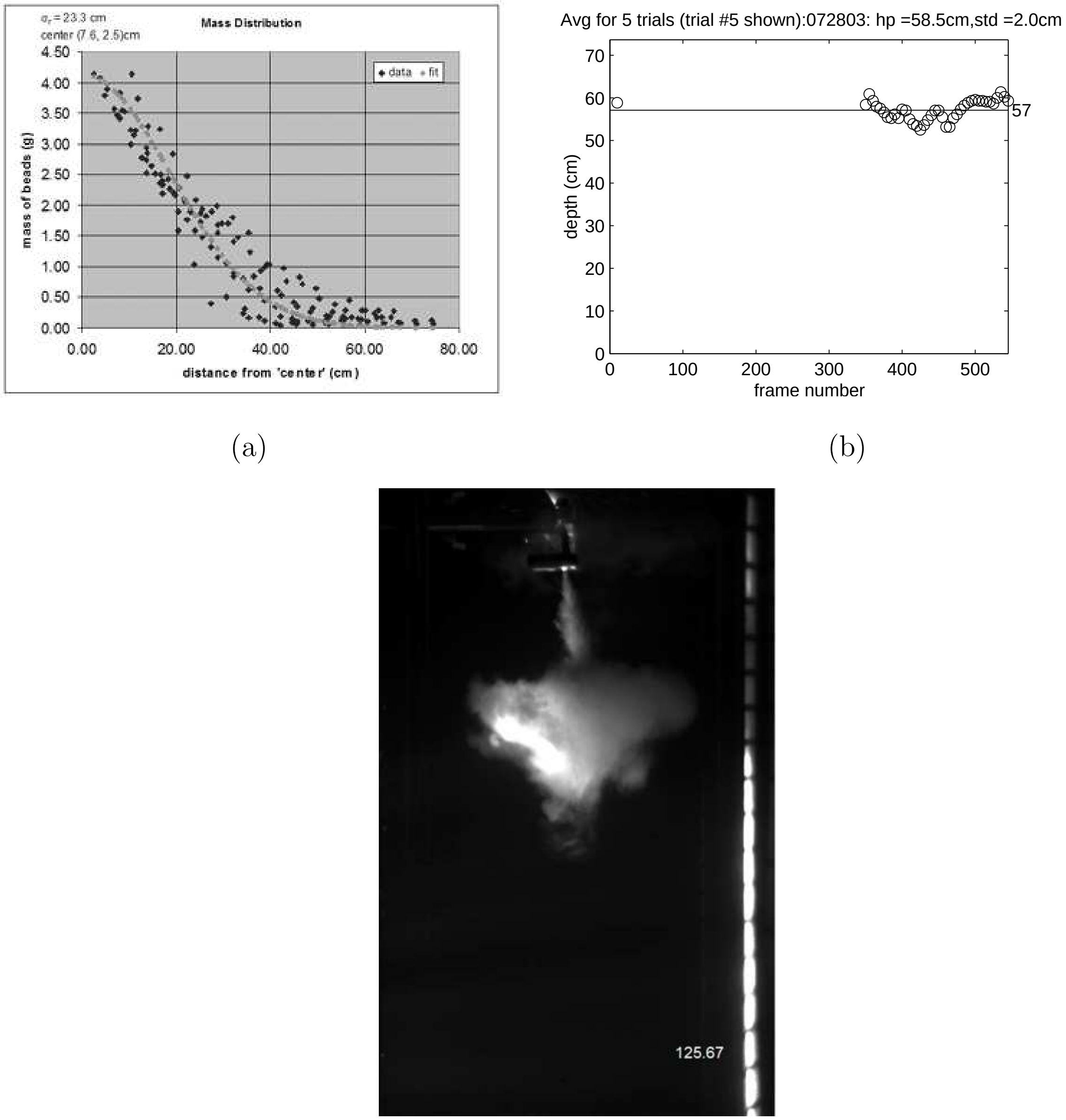

(a)

(b)

(c)

Figure A-15: Experimental run 072803: a) Sediment radial distribution, (b) Peel depths picked at various movie frames, with h_p shown for one example trial, (c) One image from the experimental run. Fluorometer profile was not available, h_t determined from ruler measurements at the time of the experiment

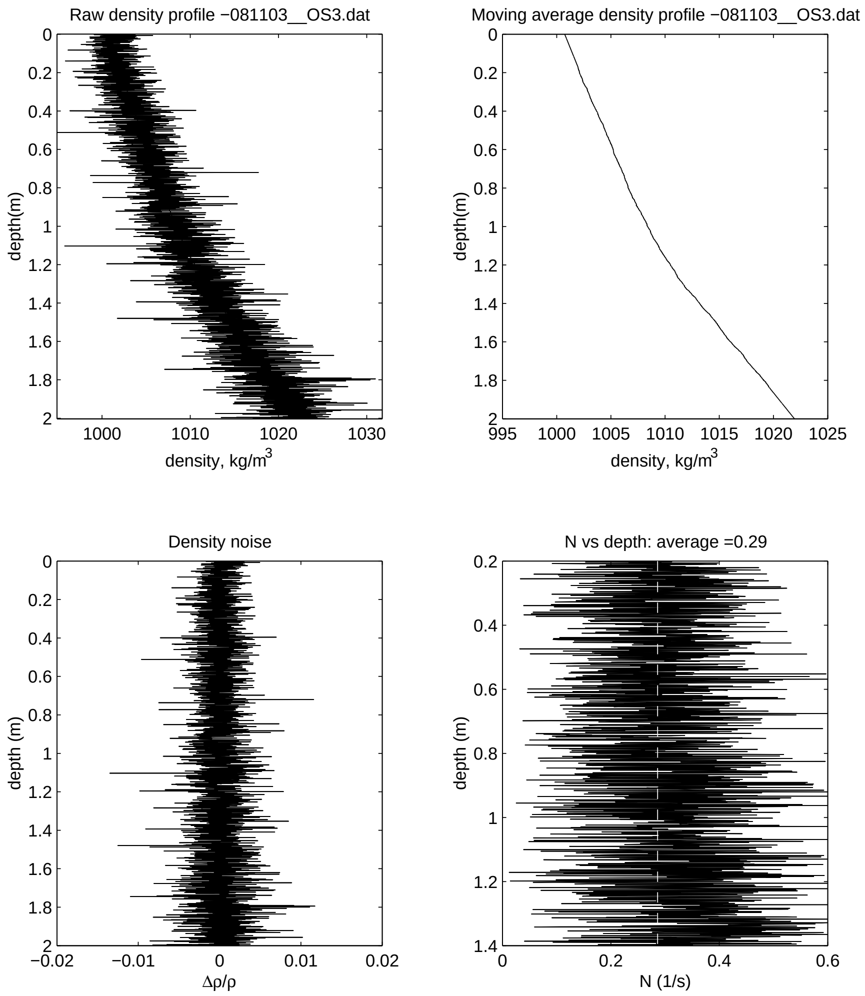

Figure A-16: Density profile for run 081103. Top left: raw density profile. Top right: moving average profile. Bottom left: Density difference between measured and average. Bottom right: Brunt-Väisälä frequency N from data

Run no.		**Time to empty (s)**	**Flow (g/s)**	**Source d (cm)**	**Source depth (m)**	**Bottom depth (m)**	**T** ^oC	S_0 **(g/kg)**	S **(g/kg)**
081103	PS	1560	0.38	**0.4**	**0.27**	1.95	26.1	9.1	30.0

Table A.9: Experimental conditions

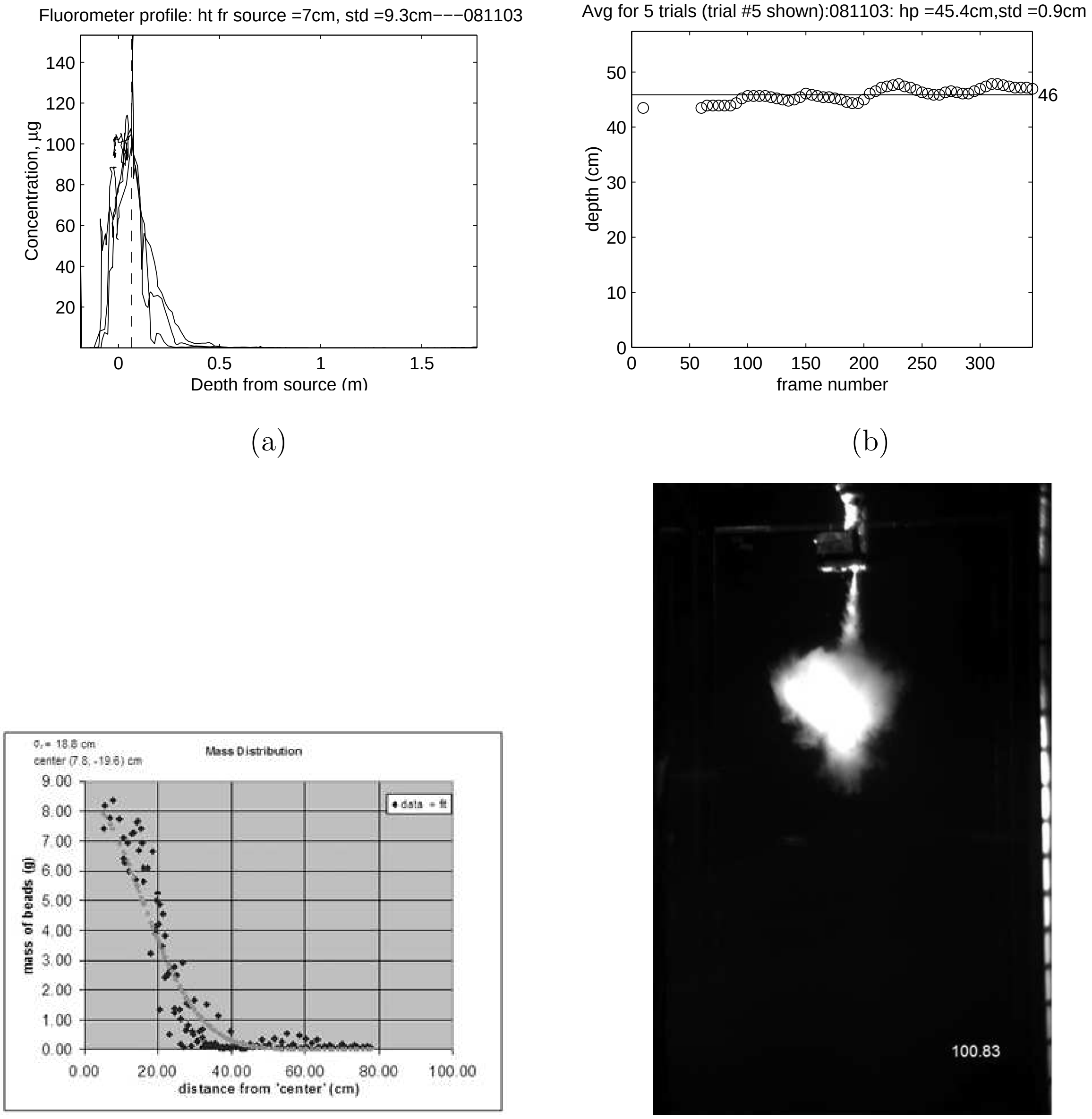

(a)

(b)

(c)

(d)

Figure A-17: Experimental run 081103: a) Fluorometer profile showing h_t, (b) Peel depths picked at various movie frames, with h_p shown for one example trial, (c) Sediment mass distribution and (d) One image from the experimental run.

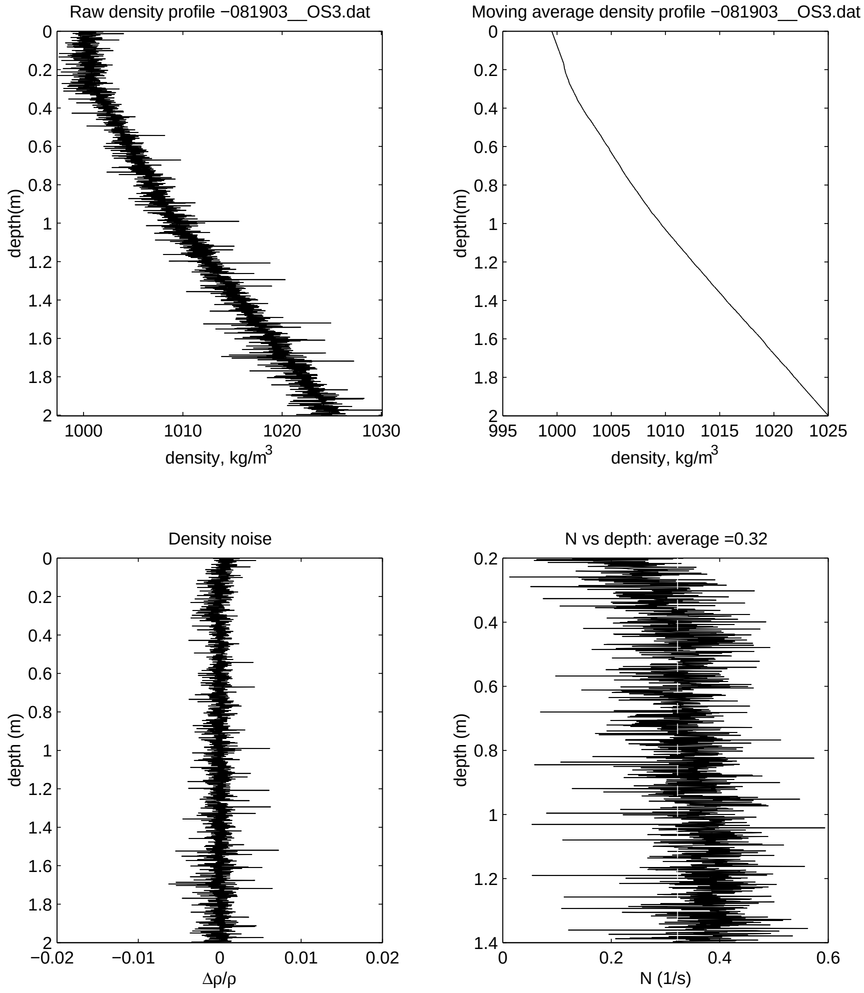

Figure A-18: Density profile for run 081903. Top left: raw density profile. Top right: moving average profile. Bottom left: Density difference between measured and average. Bottom right: Brunt-Väisälä frequency N from data

Run no.		**Time to empty (s)**	**Flow (g/s)**	**Source d (cm)**	**Source depth (m)**	**Bottom depth (m)**	**T** ^oC	S_0 **(g/kg)**	S **(g/kg)**
081903	PS	420	1.43	**0.8**	**0.27**	1.95	22.6	5.4	5.4

Table A.10: Experimental conditions

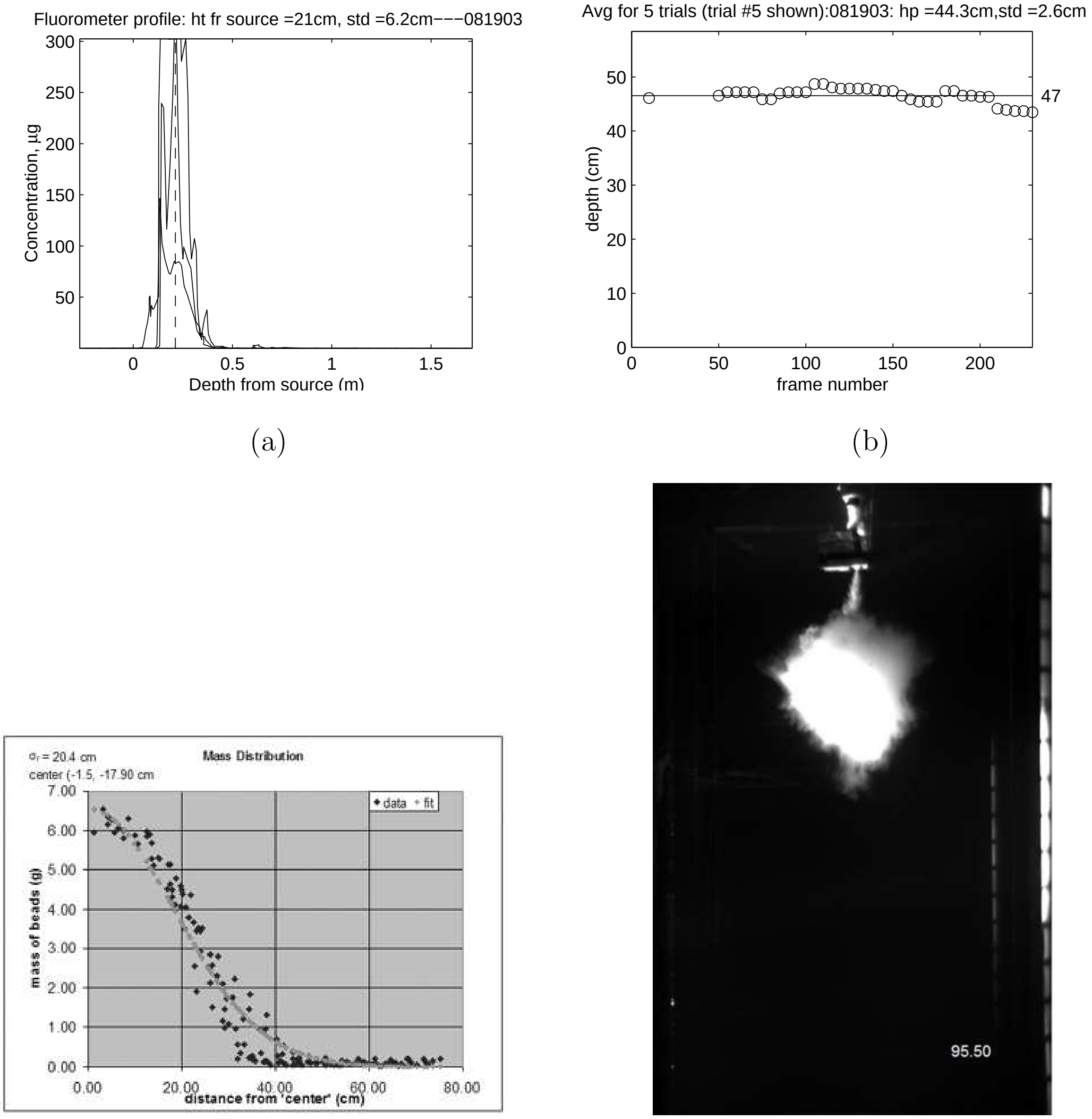

(a) (b)

(c) (d)

Figure A-19: Experimental run 081903: a) Fluorometer profile showing h_t, (b) Peel depths picked at various movie frames, with h_p shown for one example trial, (c) Sediment mass distribution and (d) One image from the experimental run.

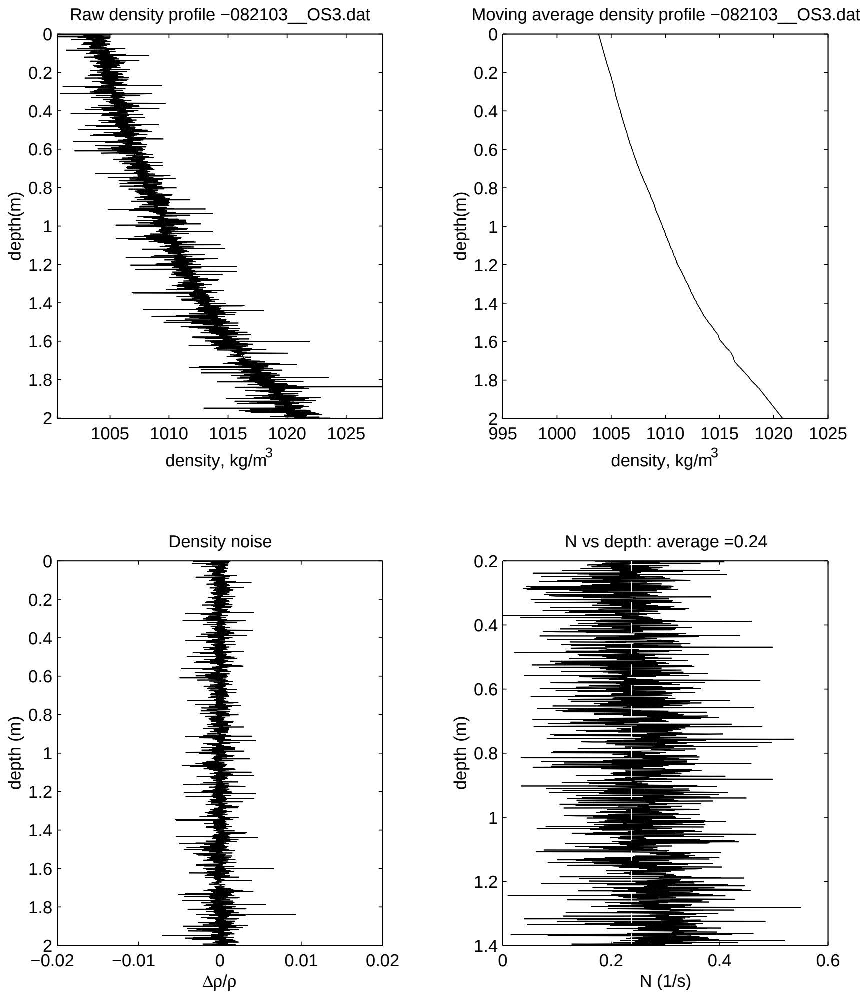

Figure A-20: Density profile for run 082103. Top left: raw density profile. Top right: moving average profile. Bottom left: Density difference between measured and average. Bottom right: Brunt-Väisälä frequency N from data

Run no.		**Time to empty (s)**	**Flow (g/s)**	**Source d (cm)**	**Source depth (m)**	**Bottom depth (m)**	**T** ^oC	S_0 **(g/kg)**	S **(g/kg)**
082103	PS	344	1.74	**0.8**	**0.27**	1.95	22.3	10.2	35.0

Table A.11: Experimental conditions

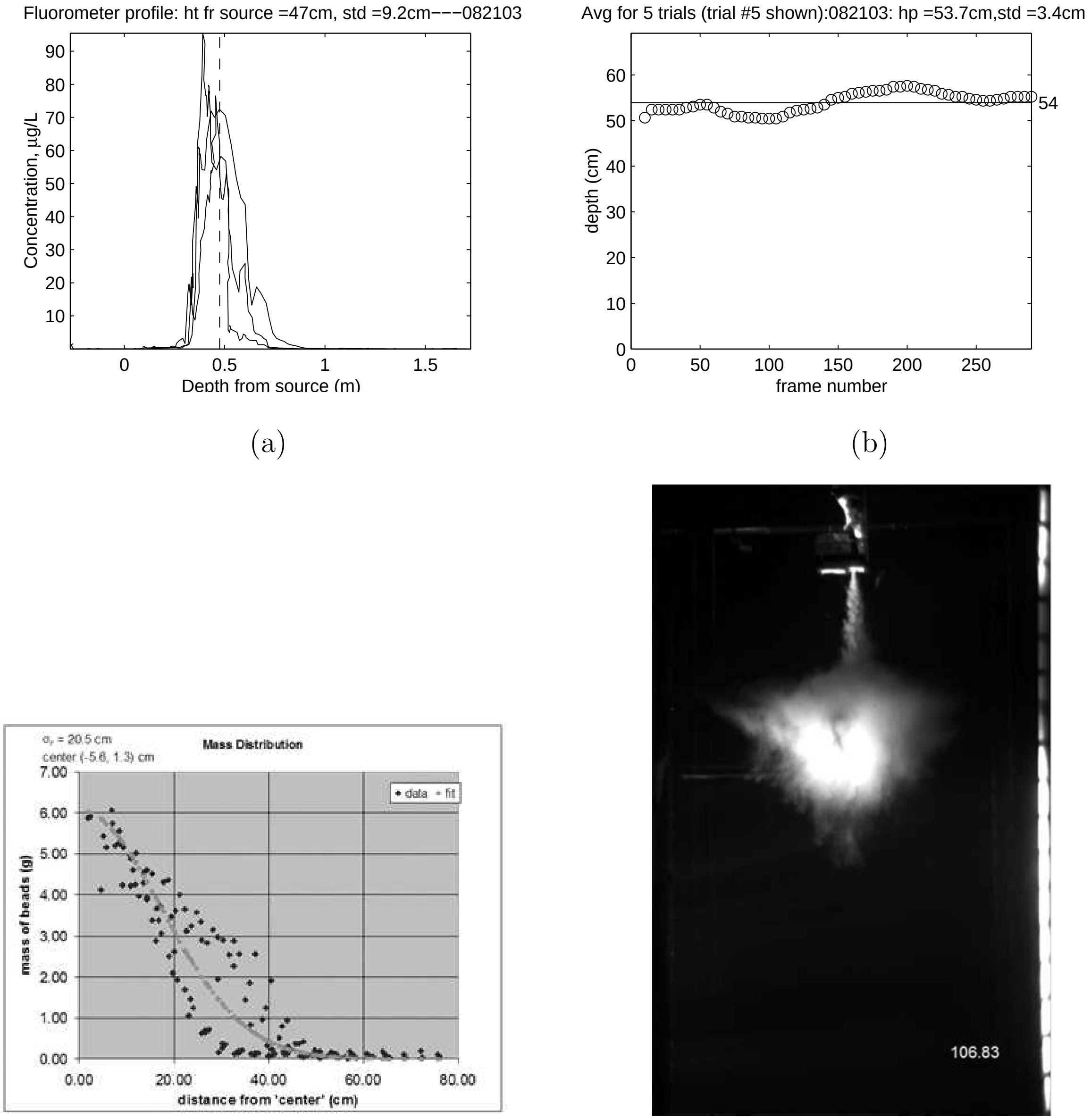

(a) (b)

(c) (d)

Figure A-21: Experimental run 082103: a) Fluorometer profile showing h_t, (b) Peel depths picked at various movie frames, with h_p shown for one example trial, (c) Sediment mass distribution and (d) One image from the experimental run.

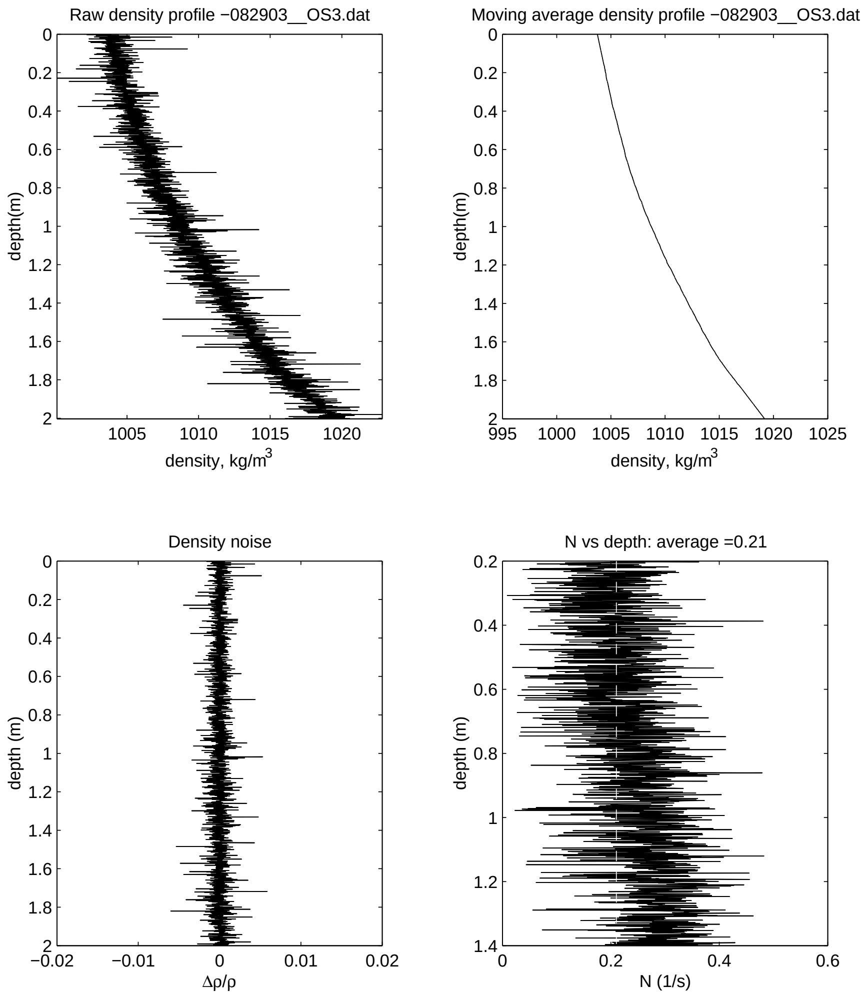

Figure A-22: Density profile for run 082903. Top left: raw density profile. Top right: moving average profile. Bottom left: Density difference between measured and average. Bottom right: Brunt-Väisälä frequency N from data

Run no.		**Time to empty (s)**	**Flow (g/s)**	**Source d (cm)**	**Source depth (m)**	**Bottom depth (m)**	**T** ^oC	S_0 **(g/kg)**	S **(g/kg)**
082903	PS	180	1.67	**0.4**	**0.27**	1.95	21.6	9.4	35.0

Table A.12: Experimental conditions

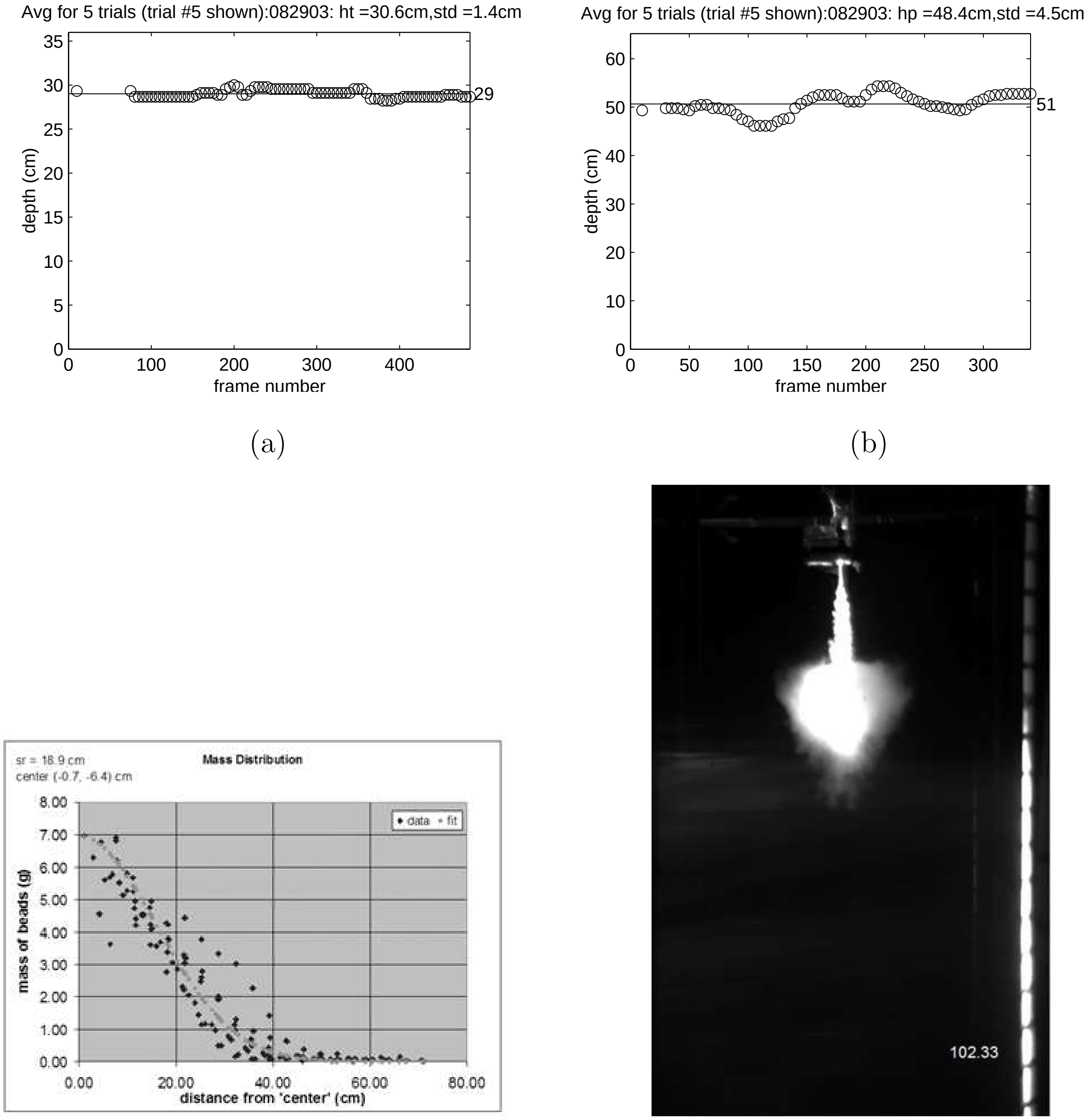

(a)

(b)

(c)

(d)

Figure A-23: Experimental run 082903: a) h_t for this run was determined from the movie file, as the fluorometer profile was unavailable, (b) Peel depths picked at various movie frames, with h_p shown for one example trial, (c) Sediment mass distribution and (d) One image from the experimental run.

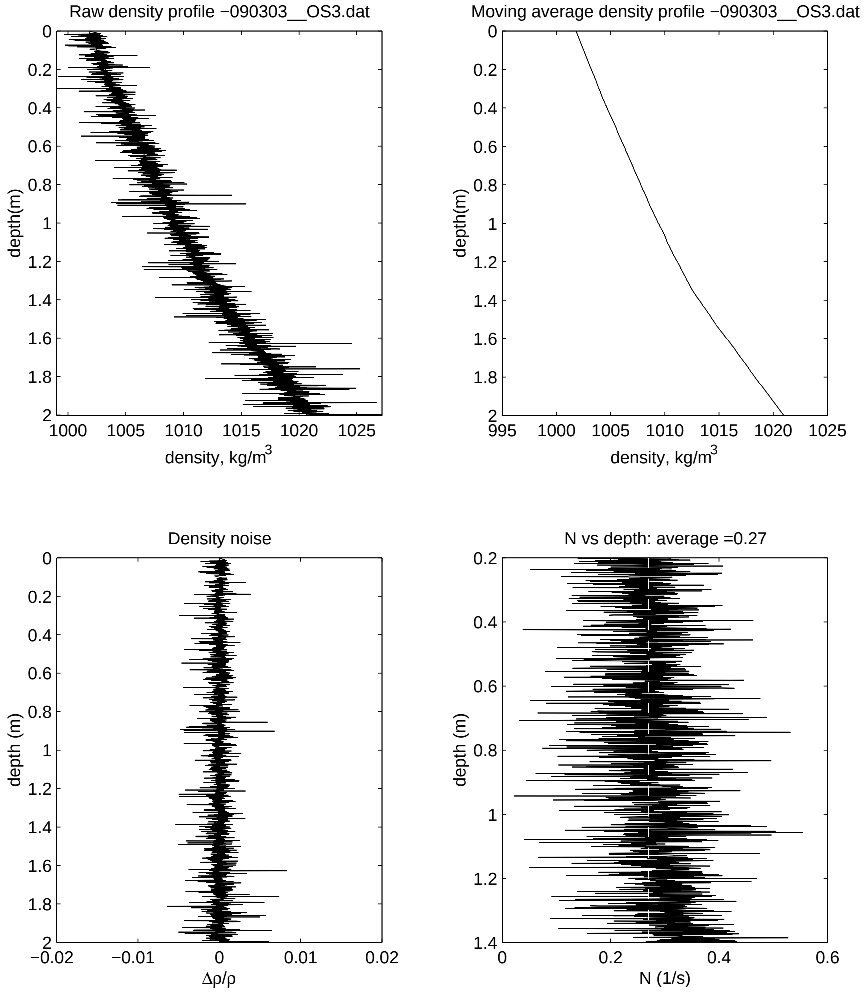

Figure A-24: Density profile for run 090303. Top left: raw density profile. Top right: moving average profile. Bottom left: Density difference between measured and average. Bottom right: Brunt-Väisälä frequency N from data

Run no.		**Time to empty (s)**	**Flow (g/s)**	**Source d (cm)**	**Source depth (m)**	**Bottom depth (m)**	**T** ^oC	S_0 **(g/kg)**	S **(g/kg)**
090303	PS	470	1.28	**0.4**	**0.27**	1.95	22.0	9.4	25.0

Table A.13: Experimental conditions

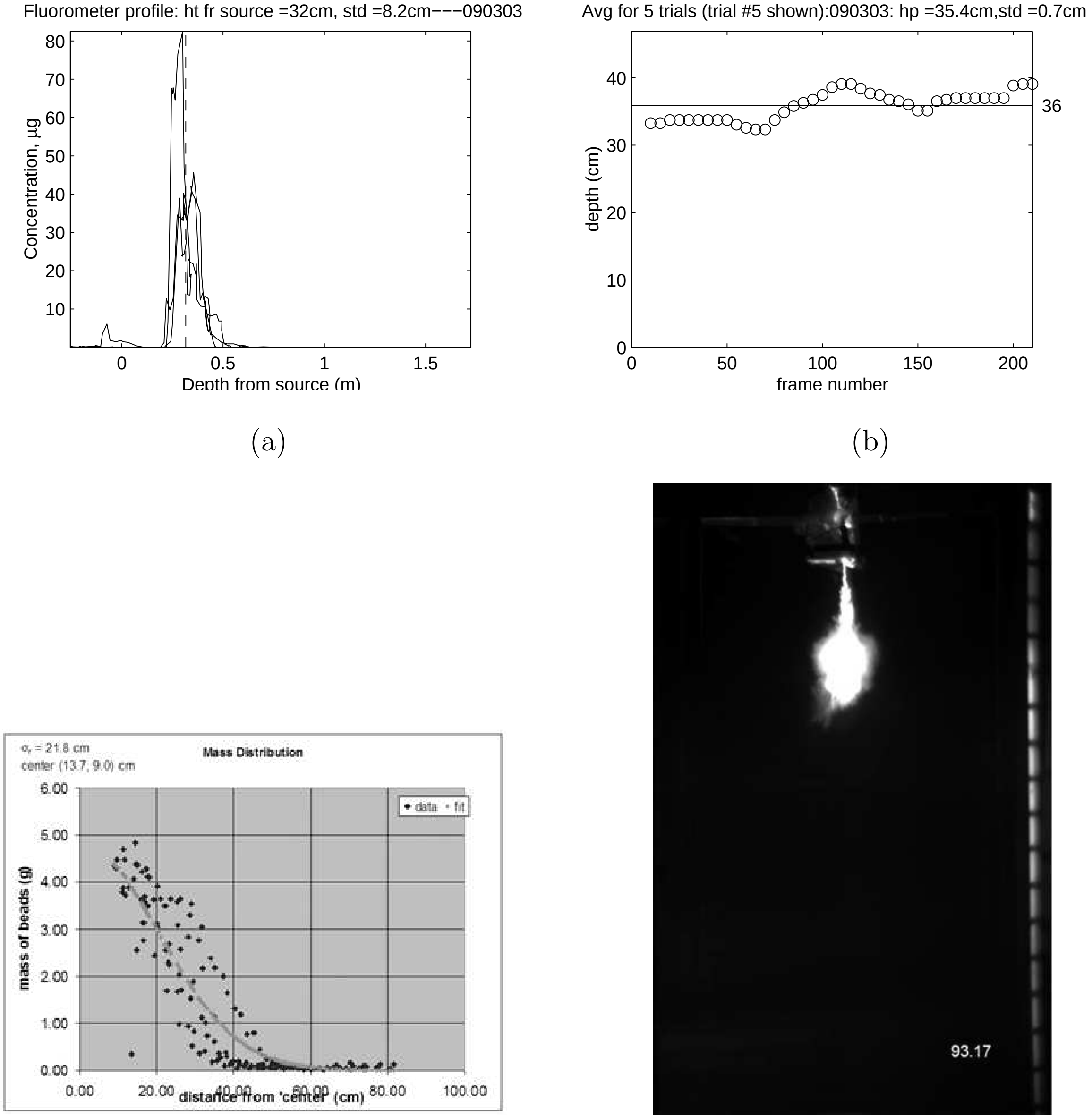

(a)

(b)

(c)

(d)

Figure A-25: Experimental run 090303: a) Fluorometer profile showing h_t, (b) Peel depths picked at various movie frames, with h_p shown for one example trial, (c) Sediment mass distribution and (d) One image from the experimental run.

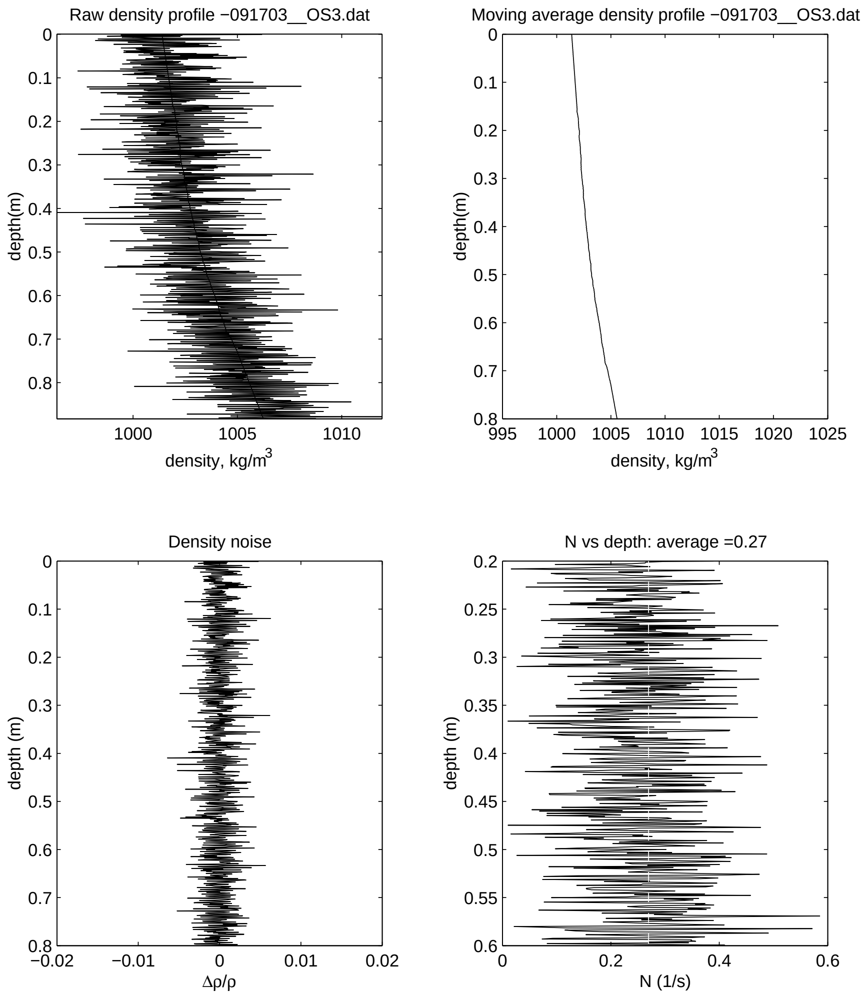
Raw density profile −091703__OS3.dat

Moving average density profile −091703__OS3.dat

Density noise

N vs depth: average =0.27

Figure A-26: Density profile for run 091703. Top left: raw density profile. Top right: moving average profile. Bottom left: Density difference between measured and average. Bottom right: Brunt-Väisälä frequency N from data

Run no.		**Time to empty (s)**	**Flow (g/s)**	**Source d (cm)**	**Source depth (m)**	**Bottom depth (m)**	**T** ^oC	S_0 **(g/kg)**	S **(g/kg)**
091703	PS	347	1.73	**0.8**	**0.27**	1.20	22.0	5.0	6.0

Table A.14: Experimental conditions

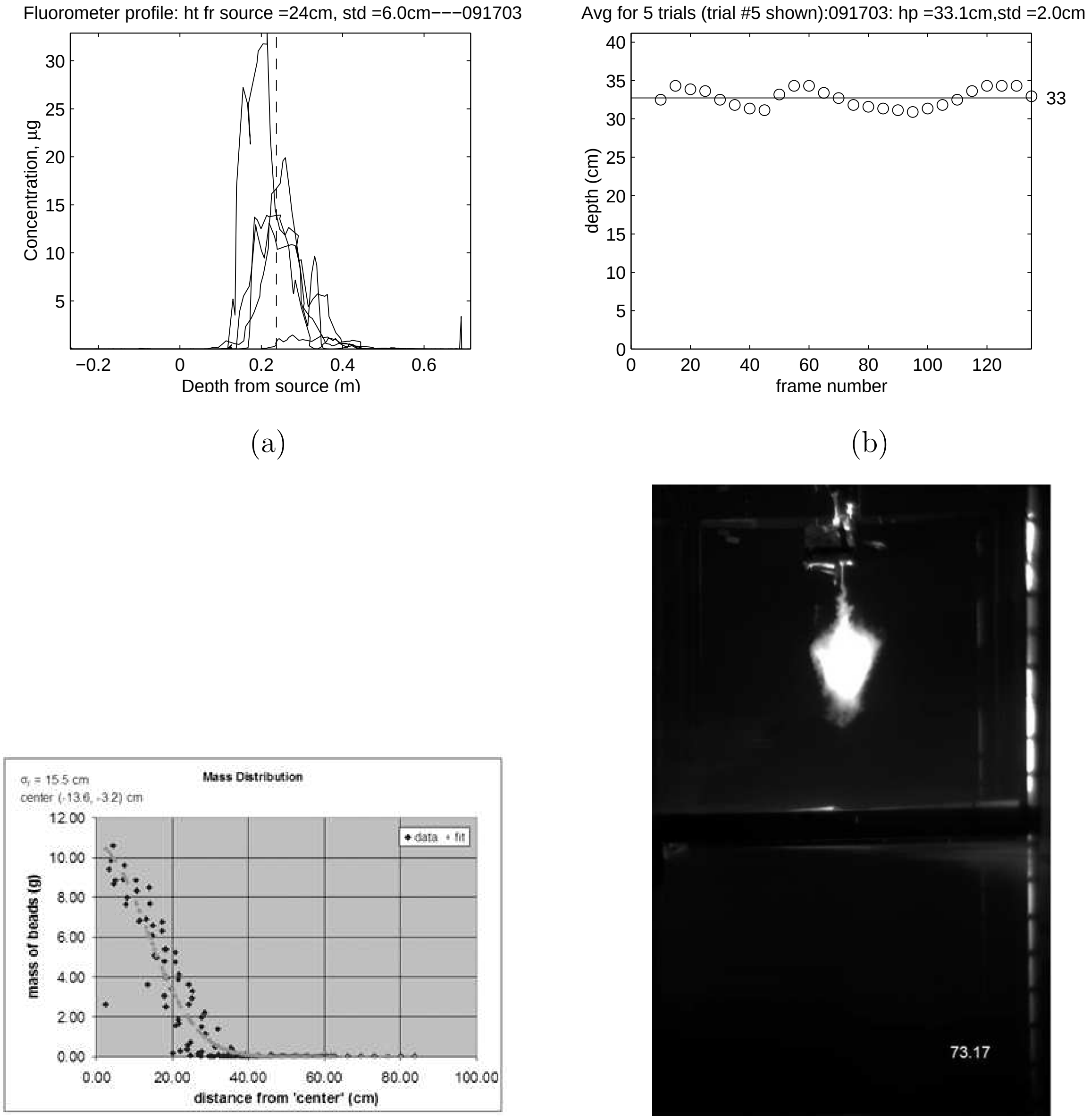

(a)

(b)

(c)

(d)

Figure A-27: Experimental run 091703: a) Fluorometer profile showing h_t, (b) Peel depths picked at various movie frames, with h_p shown for one example trial, (c) Sediment mass distribution and (d) One image from the experimental run.

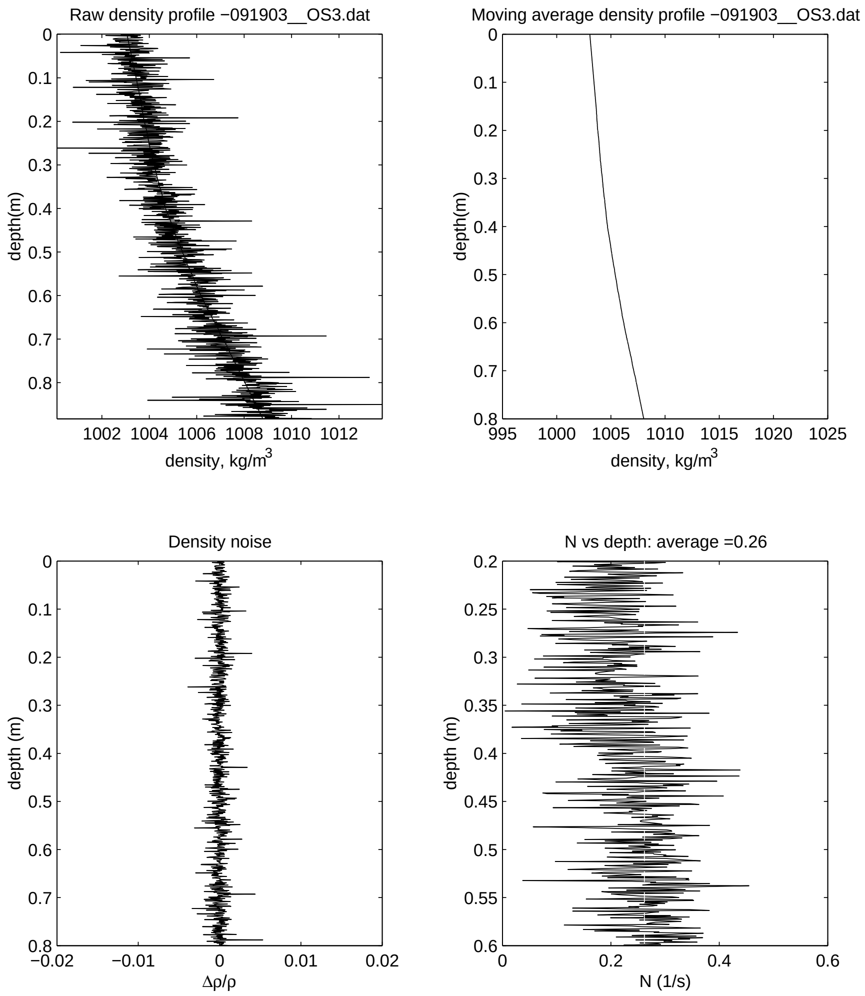

Figure A-28: Density profile for run 091903. Top left: raw density profile. Top right: moving average profile. Bottom left: Density difference between measured and average. Bottom right: Brunt-Väisälä frequency N from data

Run no.		**Time to empty (s)**	**Flow (g/s)**	**Source d (cm)**	**Source depth (m)**	**Bottom depth (m)**	**T** ^oC	S_0 **(g/kg)**	S **(g/kg)**
091903	PS	332	1.81	**0.8**	**0.27**	1.20	22.6	8.8	8.8

Table A.15: Experimental conditions

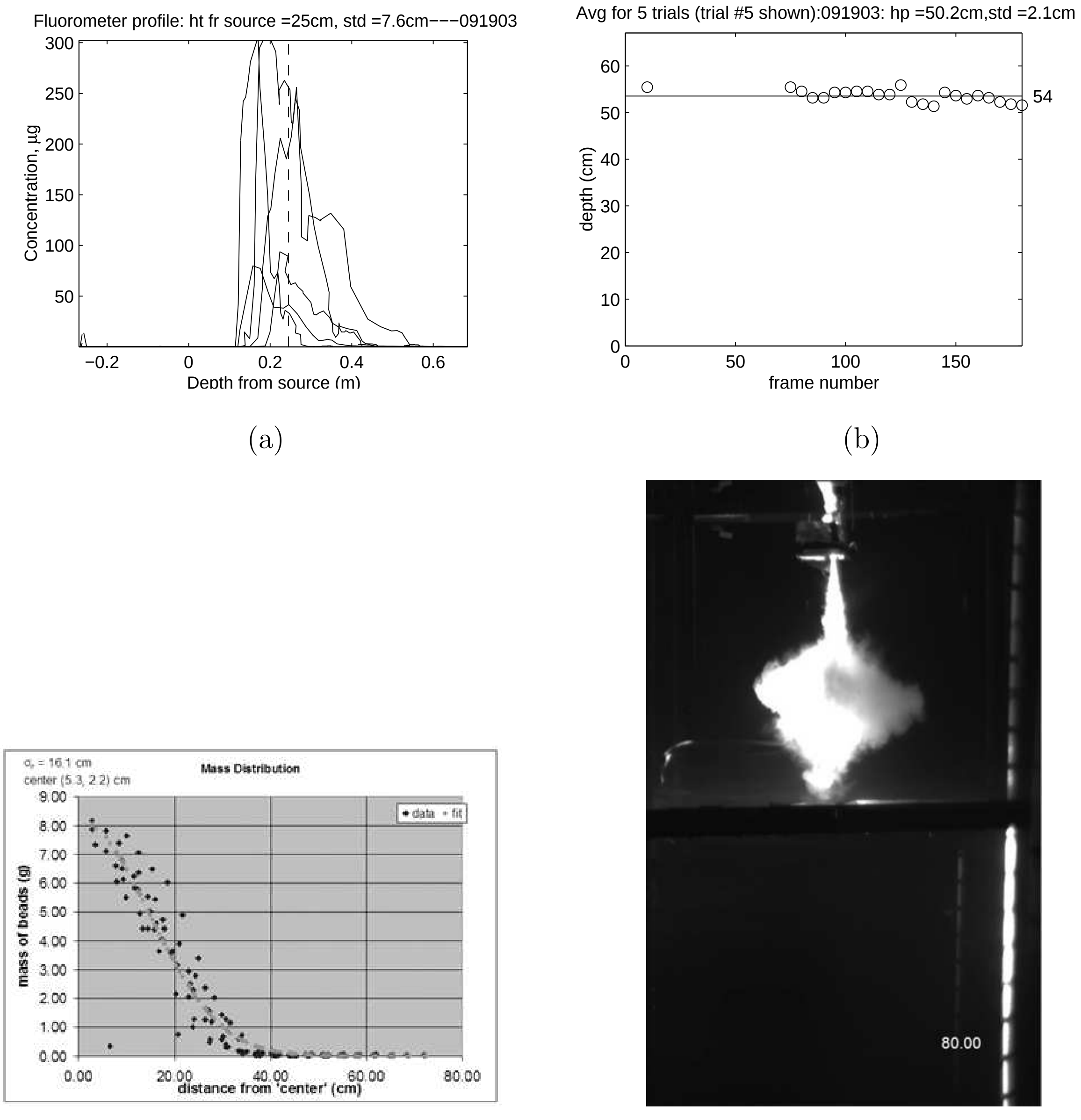

(a) (b)

(c) (d)

Figure A-29: Experimental run 091903: a) Fluorometer profile showing h_t, (b) Peel depths picked at various movie frames, with h_p shown for one example trial, (c) Sediment mass distribution and (d) One image from the experimental run.

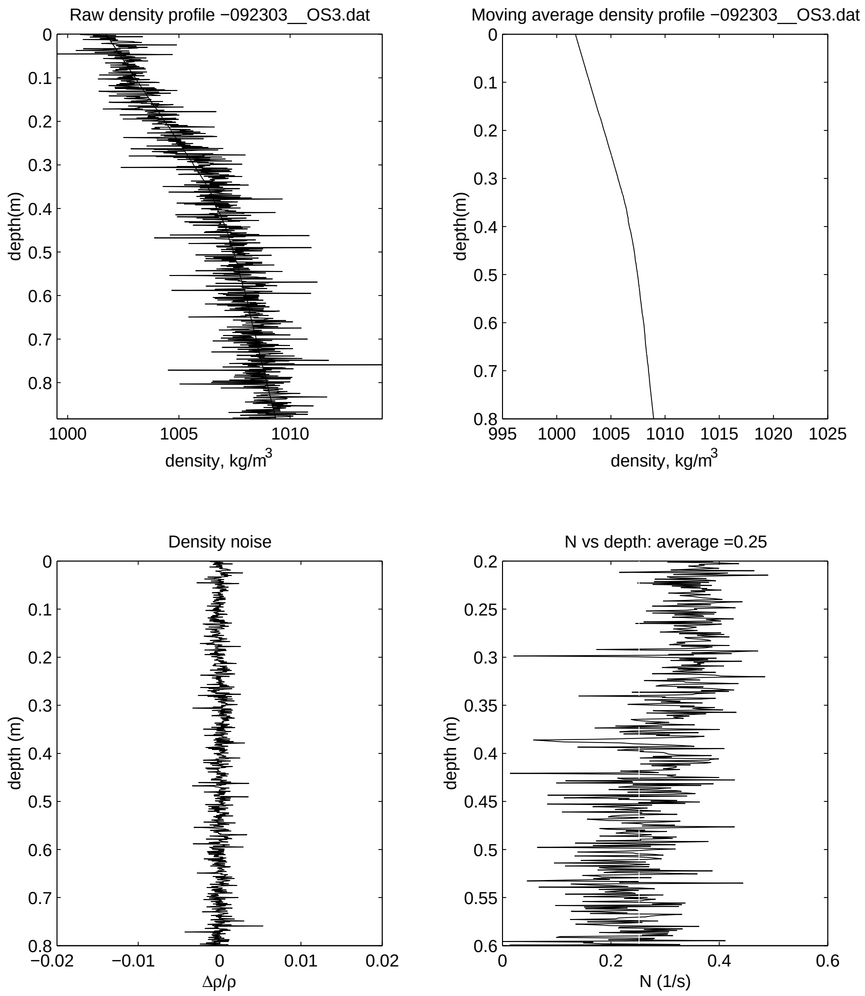

Figure A-30: Density profile for run 092303. Top left: raw density profile. Top right: moving average profile. Bottom left: Density difference between measured and average. Bottom right: Brunt-Väisälä frequency N from data

Run no.		**Time to empty (s)**	**Flow (g/s)**	**Source d (cm)**	**Source depth (m)**	**Bottom depth (m)**	**T** ^oC	S_0 **(g/kg)**	S **(g/kg)**
092303	PS	280	2.14	**0.8**	**0.27**	1.20	23.1	11.9	11.9

Table A.16: Experimental conditions

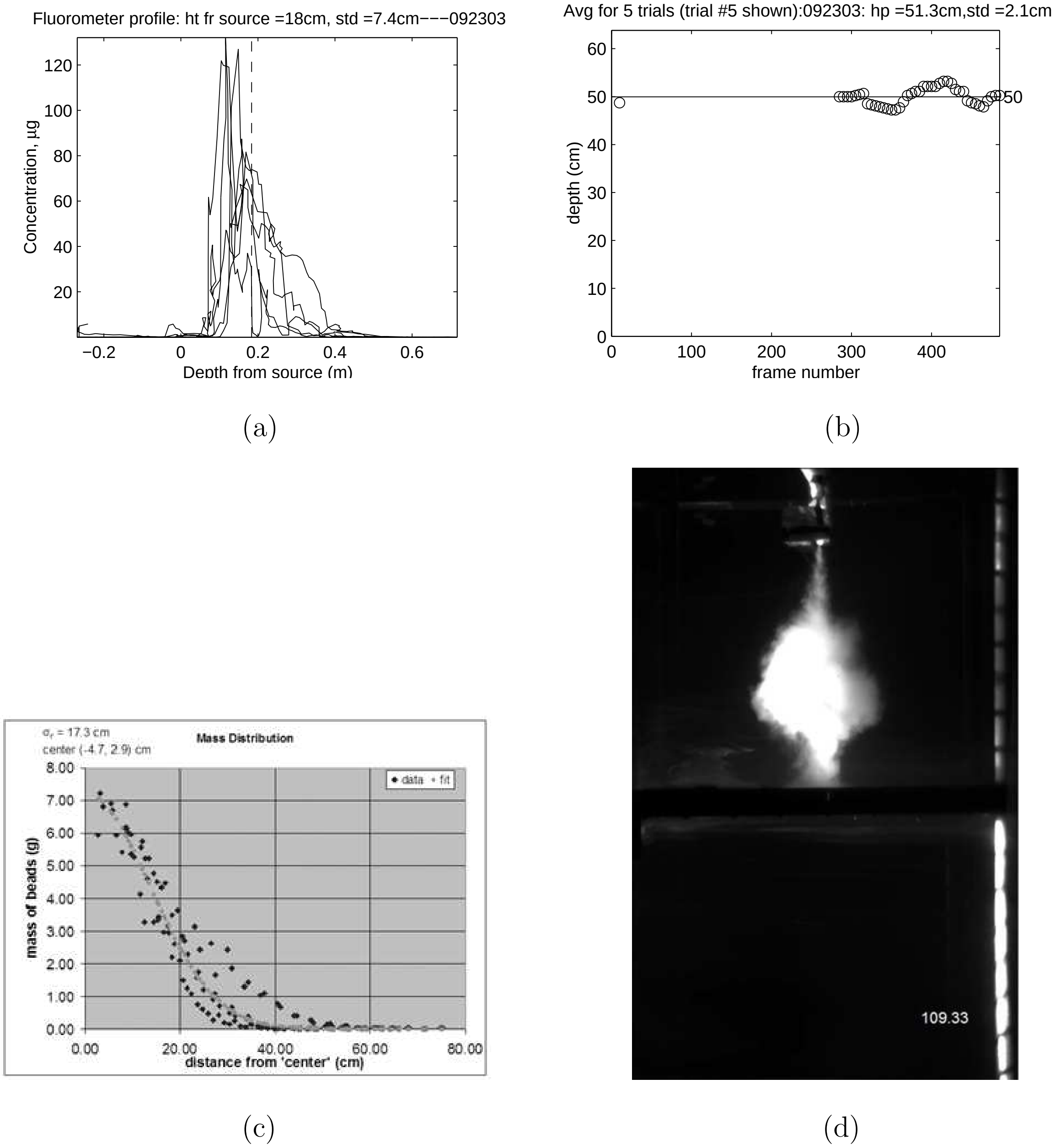

(a) (b)

(c) (d)

Figure A-31: Experimental run 092303: a) Fluorometer profile showing h_t, (b) Peel depths picked at various movie frames, with h_p shown for one example trial, (c) Sediment mass distribution and (d) One image from the experimental run.

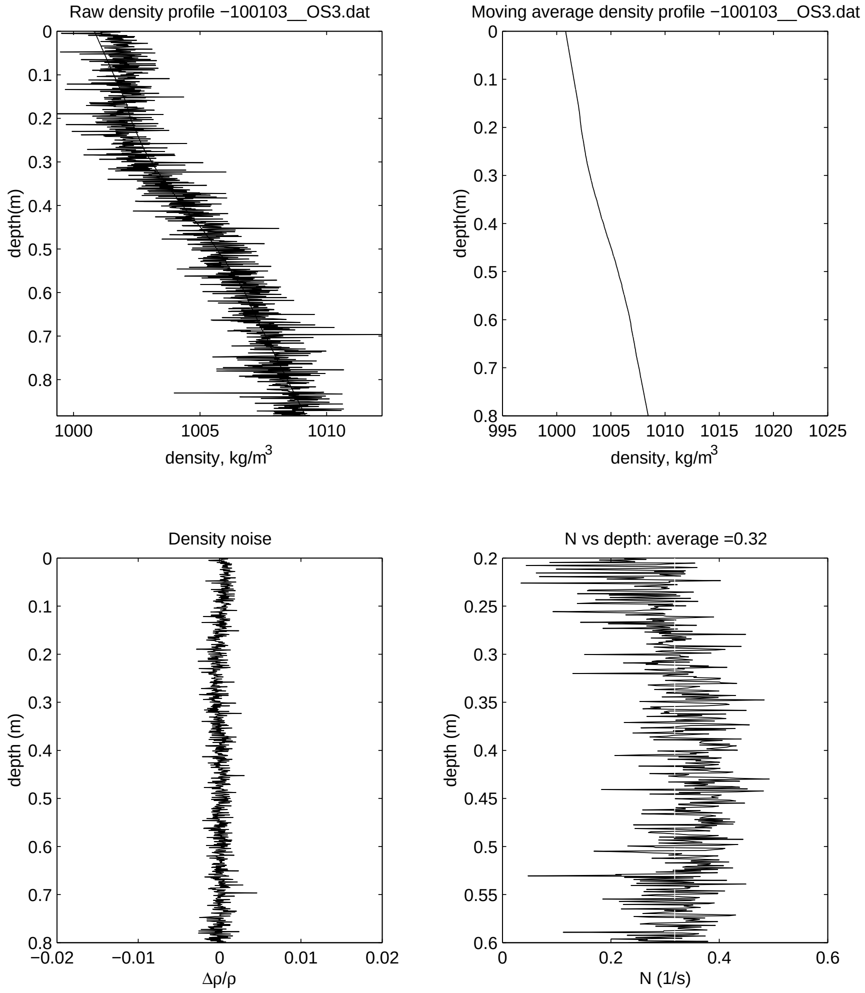

Figure A-32: Density profile for run 100103. Top left: raw density profile. Top right: moving average profile. Bottom left: Density difference between measured and average. Bottom right: Brunt-Väisälä frequency N from data

Run no.		**Time to empty (s)**	**Flow (g/s)**	**Source d (cm)**	**Source depth (m)**	**Bottom depth (m)**	**T** ^oC	S_0 **(g/kg)**	S **(g/kg)**
100103	PS	660	0.24	**0.4**	**0.27**	1.20	21.8	7.4	75.0

Table A.17: Experimental conditions

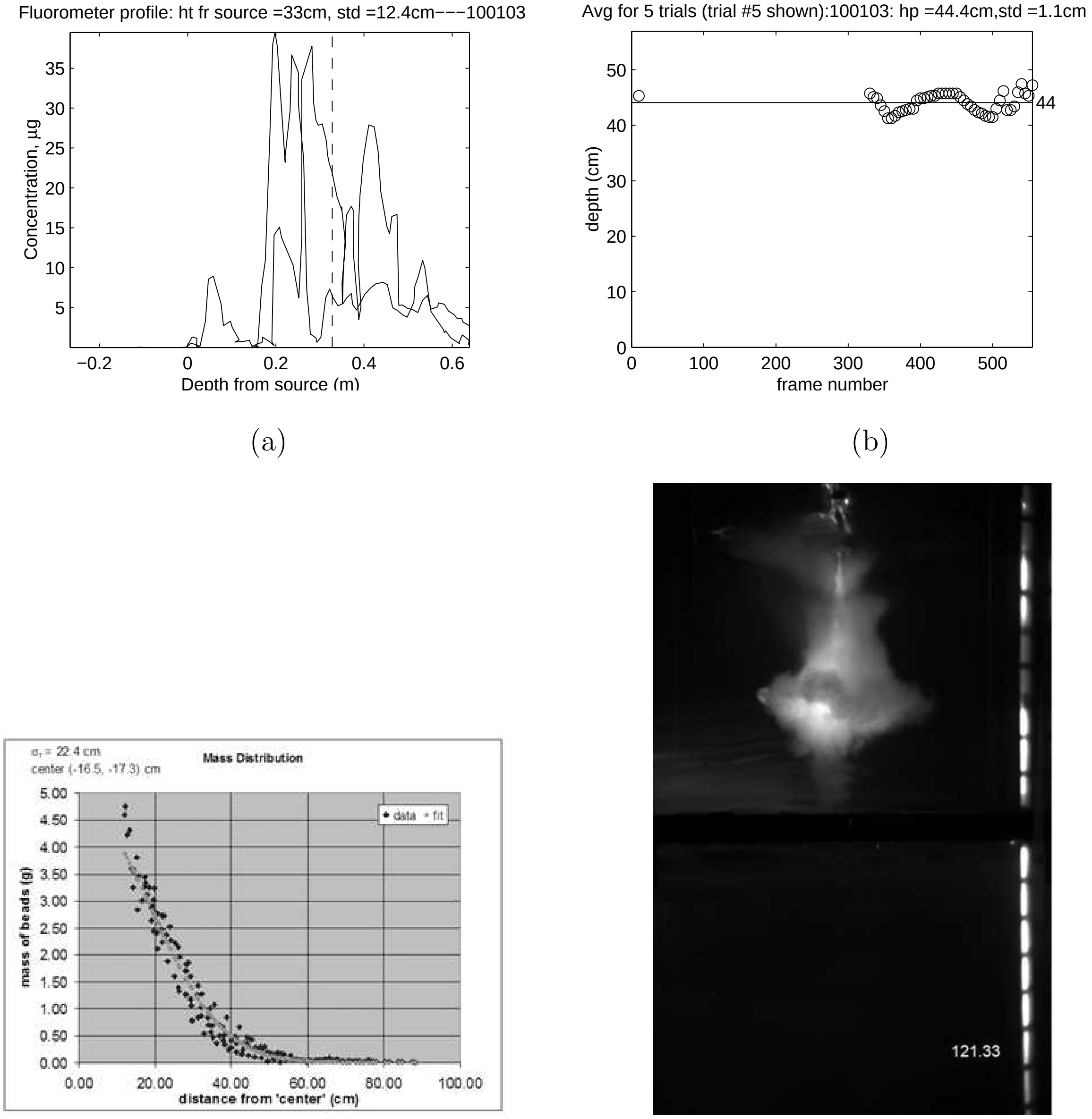

(a) (b)

(c) (d)

Figure A-33: Experimental run 100103: a) Fluorometer profile showing h_t, (b) Peel depths picked at various movie frames, with h_p shown for one example trial, (c) Sediment mass distribution and (d) One image from the experimental run.

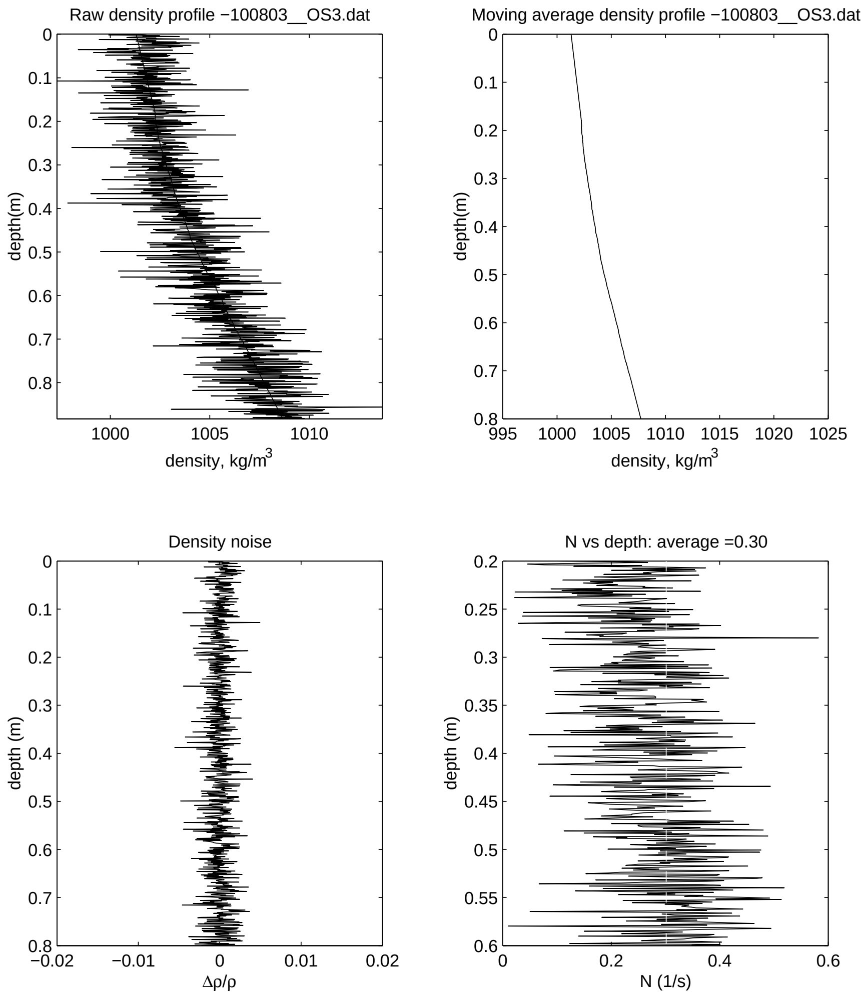

Figure A-34: Density profile for run 100803. Top left: raw density profile. Top right: moving average profile. Bottom left: Density difference between measured and average. Bottom right: Brunt-Väisälä frequency N from data

Run no.		**Time to empty (s)**	**Flow (g/s)**	**Source d (cm)**	**Source depth (m)**	**Bottom depth (m)**	**T** ^oC	S_0 **(g/kg)**	S **(g/kg)**
100803	PS	660	0.24	**0.4**	**0.27**	1.20	21.4	6.4	33.0

Table A.18: Experimental conditions

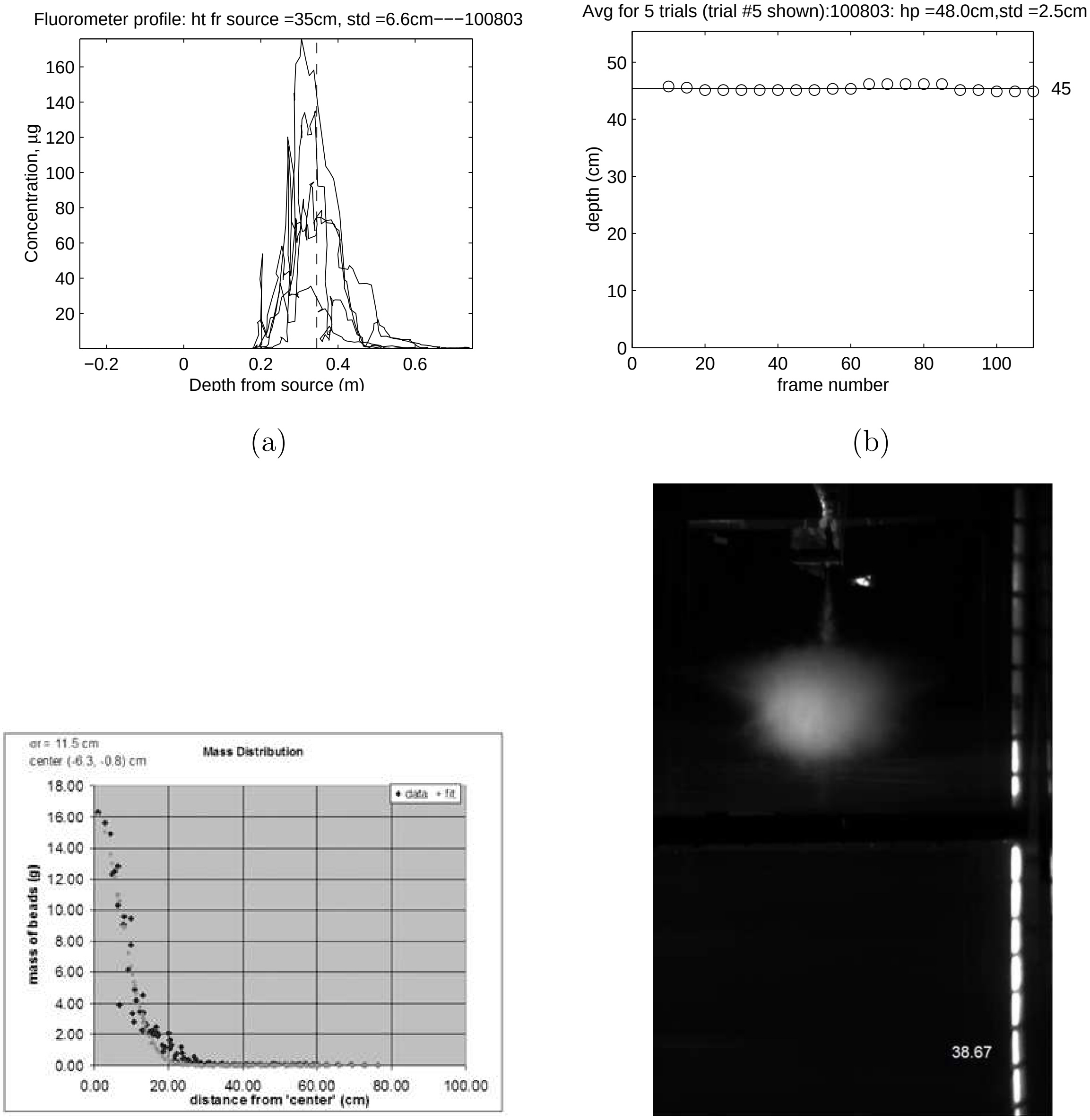

(a)

(b)

(c)

(d)

Figure A-35: Experimental run 100803: a) Fluorometer profile showing h_t, (b) Peel depths picked at various movie frames, with h_p shown for one example trial, (c) Sediment mass distribution and (d) One image from the experimental run.

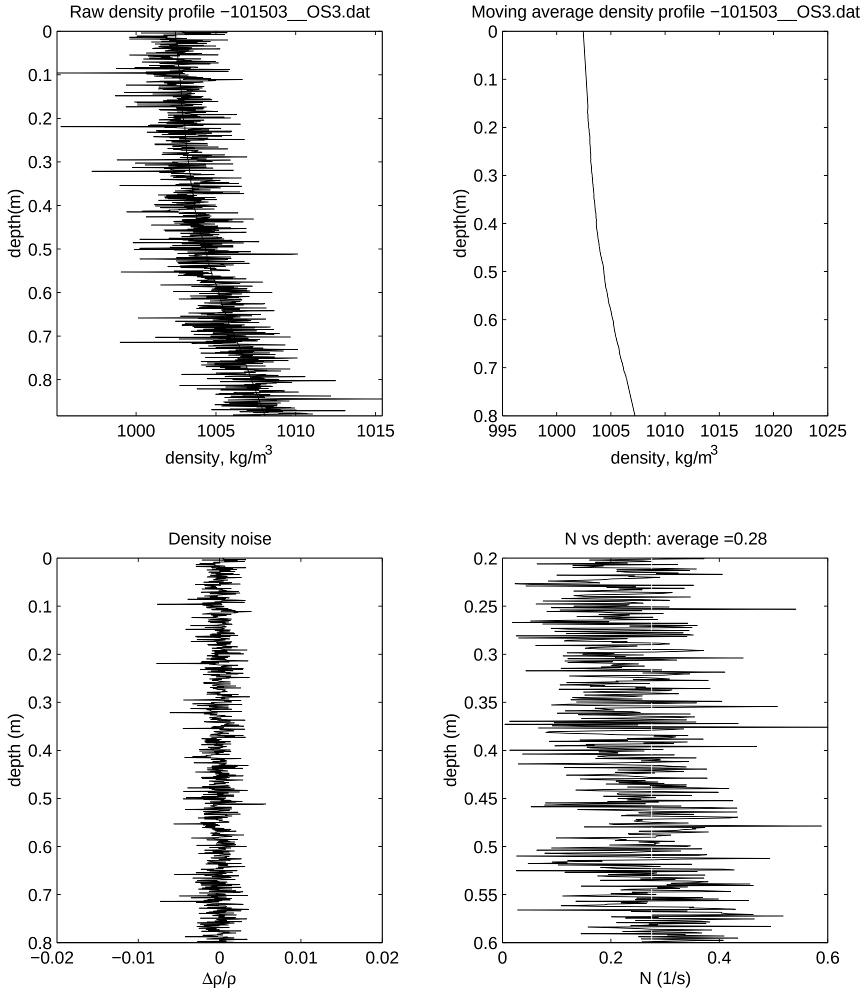

Figure A-36: Density profile for run 101503. Top left: raw density profile. Top right: moving average profile. Bottom left: Density difference between measured and average. Bottom right: Brunt-Väisälä frequency N from data

Run no.		**Time to empty (s)**	**Flow (g/s)**	**Source d (cm)**	**Source depth (m)**	**Bottom depth (m)**	**T** ^oC	S_0 **(g/kg)**	S **(g/kg)**
101503	PS	660	0.24	**0.4**	**0.27**	1.20	22.5	8.5	36.0

Table A.19: Experimental conditions

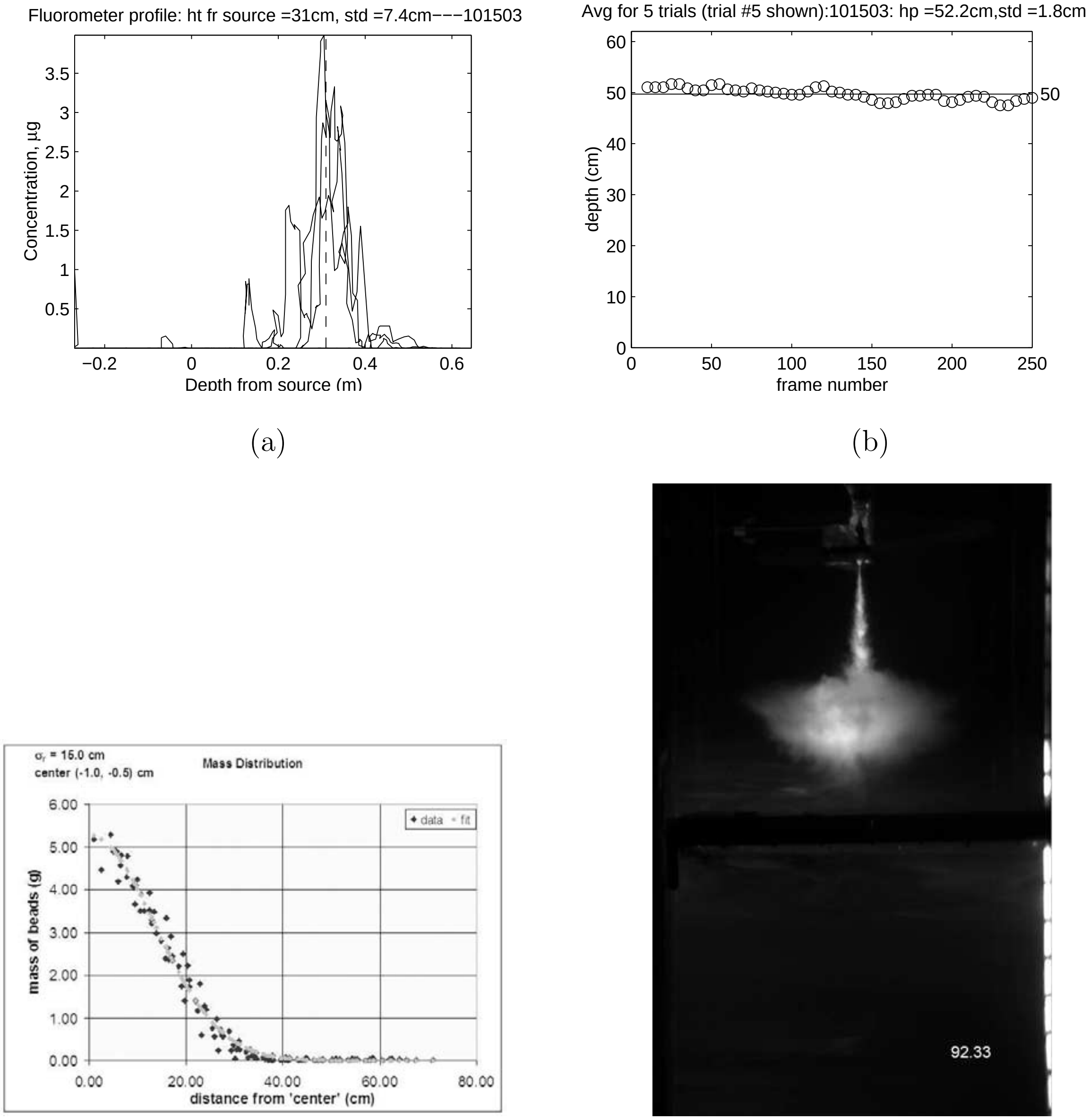

(a) (b)

(c) (d)

Figure A-37: Experimental run 101503: a) Fluorometer profile showing h_t, (b) Peel depths picked at various movie frames, with h_p shown for one example trial, (c) Sediment mass distribution and (d) One image from the experimental run.

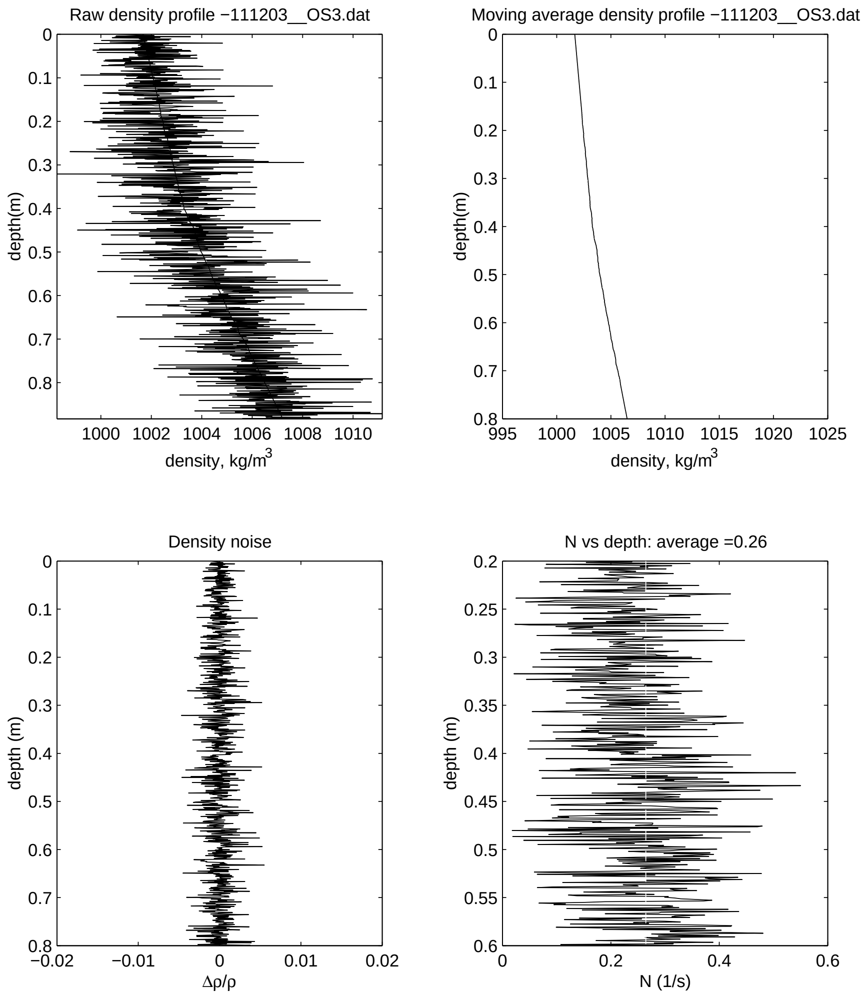

Figure A-38: Density profile for run 111203. Top left: raw density profile. Top right: moving average profile. Bottom left: Density difference between measured and average. Bottom right: Brunt-Väisälä frequency N from data

Run no.		**Time to empty (s)**	**Flow (g/s)**	**Source d (cm)**	**Source depth (m)**	**Bottom depth (m)**	**T** ^oC	S_0 **(g/kg)**	S **(g/kg)**
111203	PS	248	1.20	**0.4**	**0.27**	1.20	20.4	4.0	5.0

Table A.20: Experimental conditions

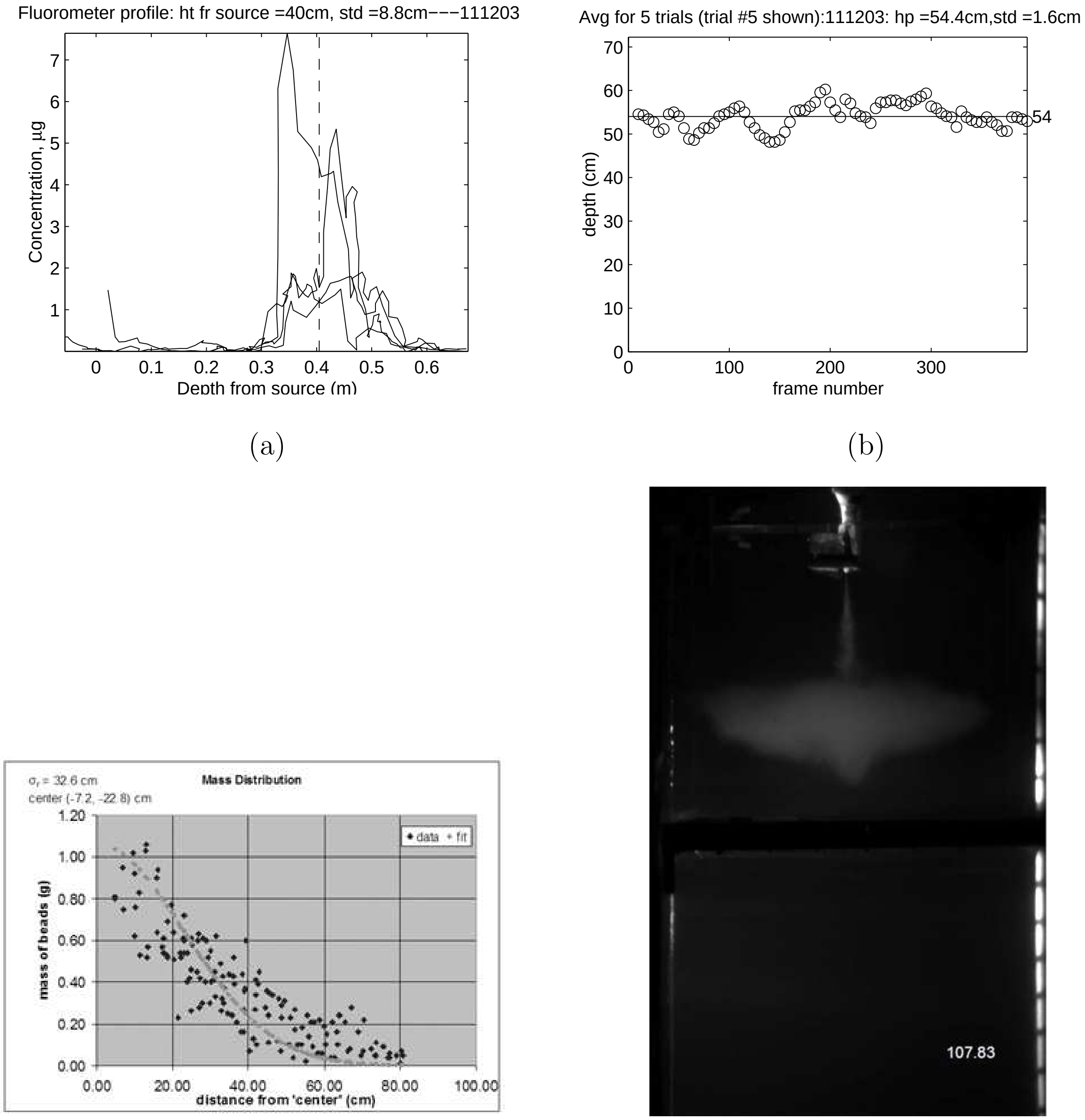

(a)

(b)

(c)

(d)

Figure A-39: Experimental run 111203: a) Fluorometer profile showing h_t, (b) Peel depths picked at various movie frames, with h_p shown for one example trial, (c) Sediment mass distribution and (d) One image from the experimental run.

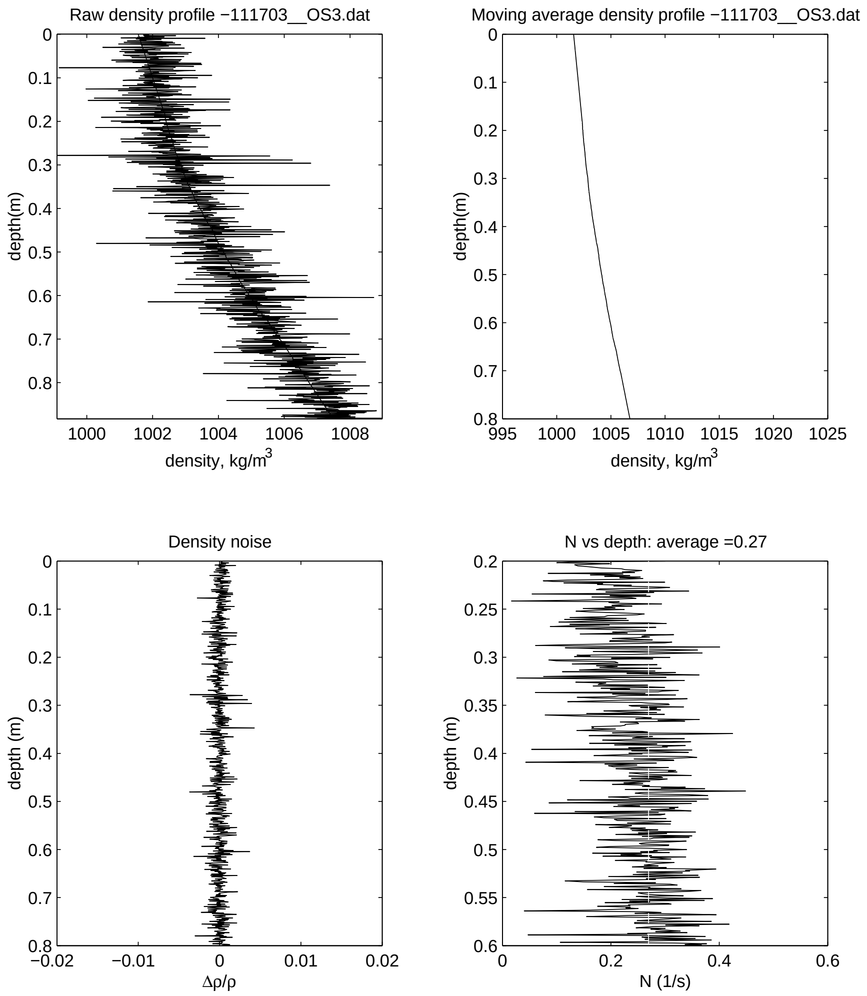

Figure A-40: Density profile for run 111703. Top left: raw density profile. Top right: moving average profile. Bottom left: Density difference between measured and average. Bottom right: Brunt-Väisälä frequency N from data

Run no.		**Time to empty (s)**	**Flow (g/s)**	**Source d (cm)**	**Source depth (m)**	**Bottom depth (m)**	**T** ^oC	S_0 **(g/kg)**	S **(g/kg)**
111703	PS	429	1.40	**0.4**	**0.27**	1.20	20.2	6.5	7.7

Table A.21: Experimental conditions

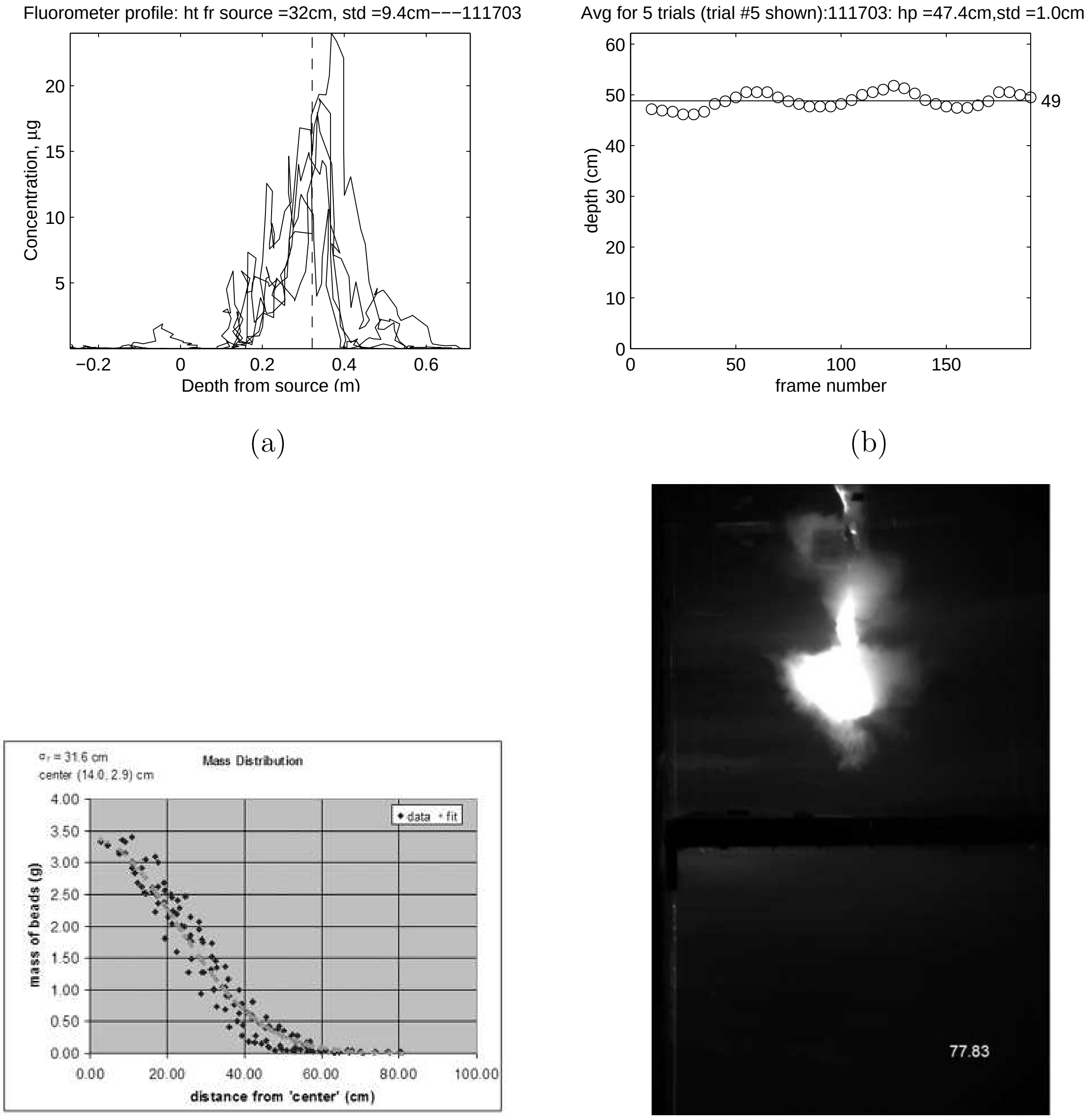

(a)

(b)

(c)

(d)

Figure A-41: Experimental run 111703: a) Fluorometer profile showing h_t, (b) Peel depths picked at various movie frames, with h_p shown for one example trial, (c) Sediment mass distribution and (d) One image from the experimental run.

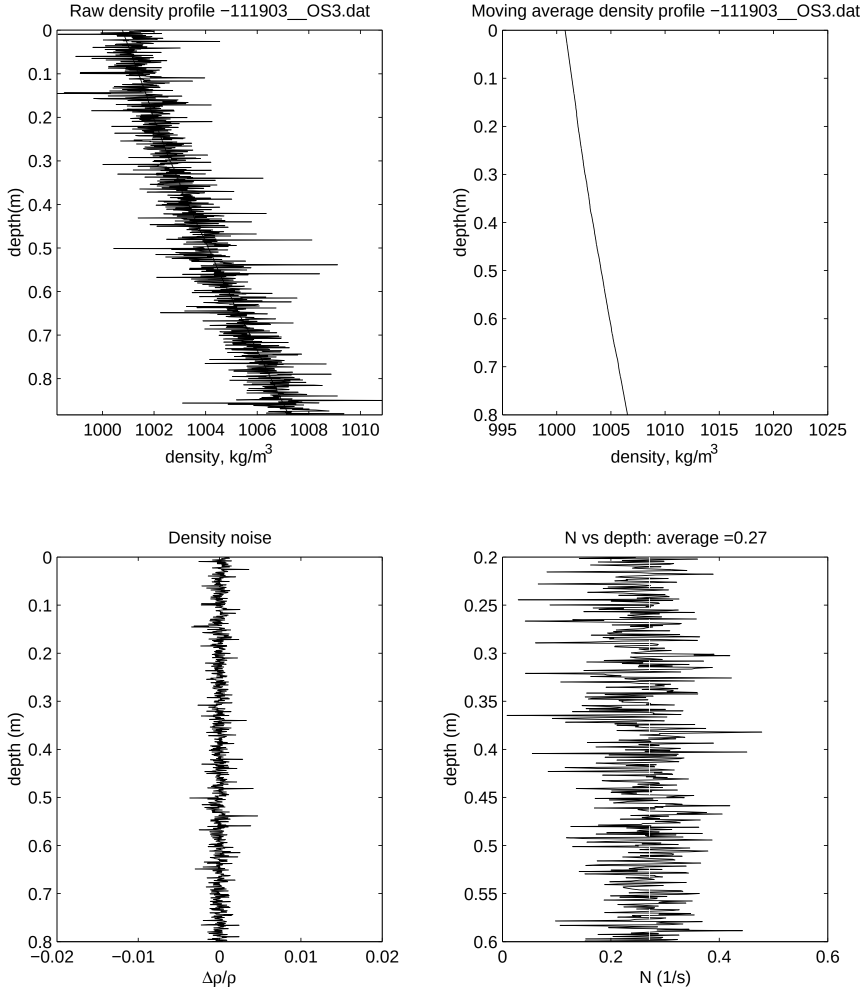

Figure A-42: Density profile for run 111903. Top left: raw density profile. Top right: moving average profile. Bottom left: Density difference between measured and average. Bottom right: Brunt-Väisälä frequency N from data

Run no.		**Time to empty (s)**	**Flow (g/s)**	**Source d (cm)**	**Source depth (m)**	**Bottom depth (m)**	**T** ^oC	S_0 **(g/kg)**	S **(g/kg)**
111903	PS	254	2.12	**0.8**	**0.27**	1.20	20.3	6.3	8.0

Table A.22: Experimental conditions

n

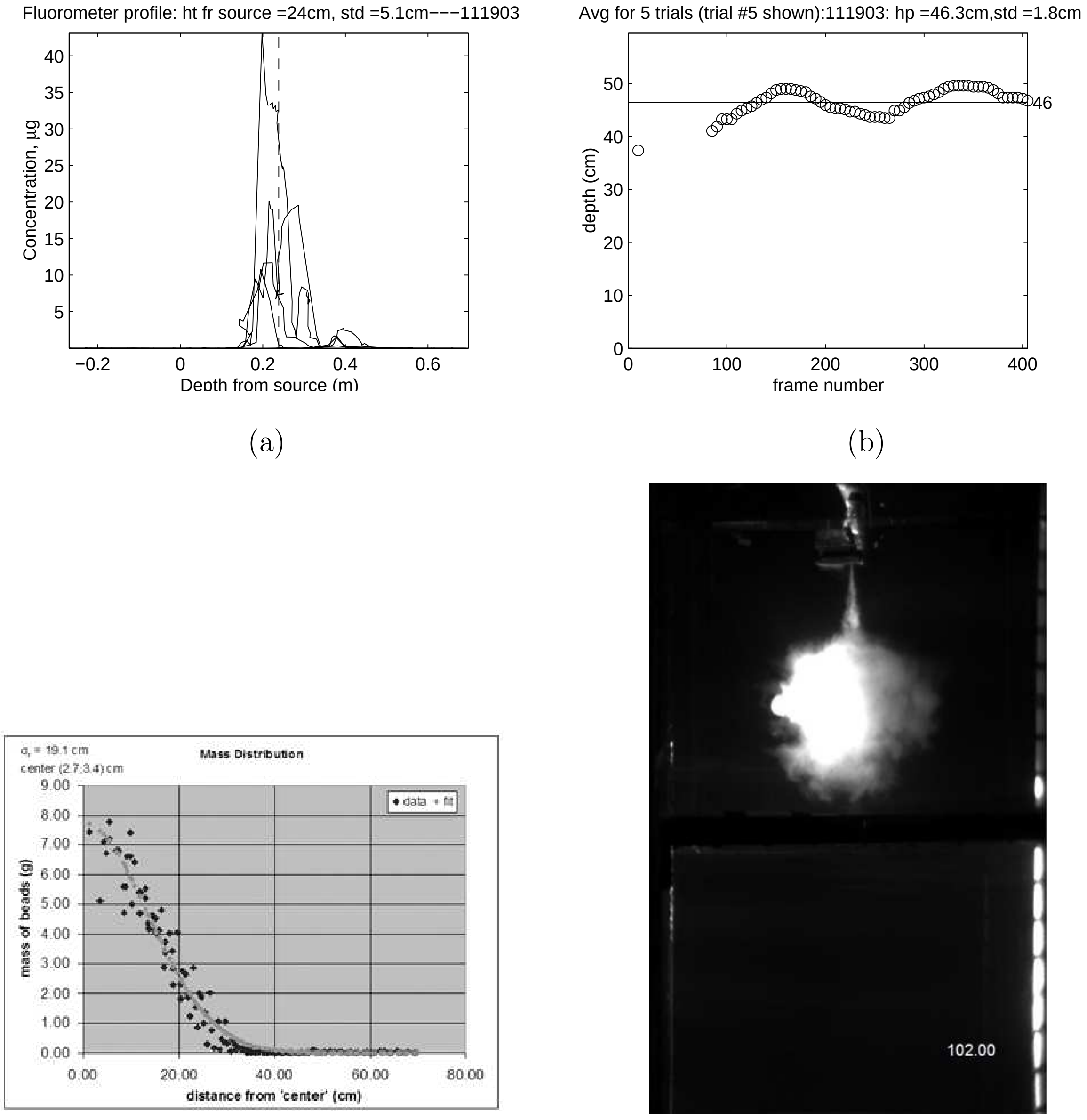

(a) (b)

(c) (d)

Figure A-43: Experimental run 111903: a) Fluorometer profile showing h_t, (b) Peel depths picked at various movie frames, with h_p shown for one example trial, (c) Sediment mass distribution and (d) One image from the experimental run.

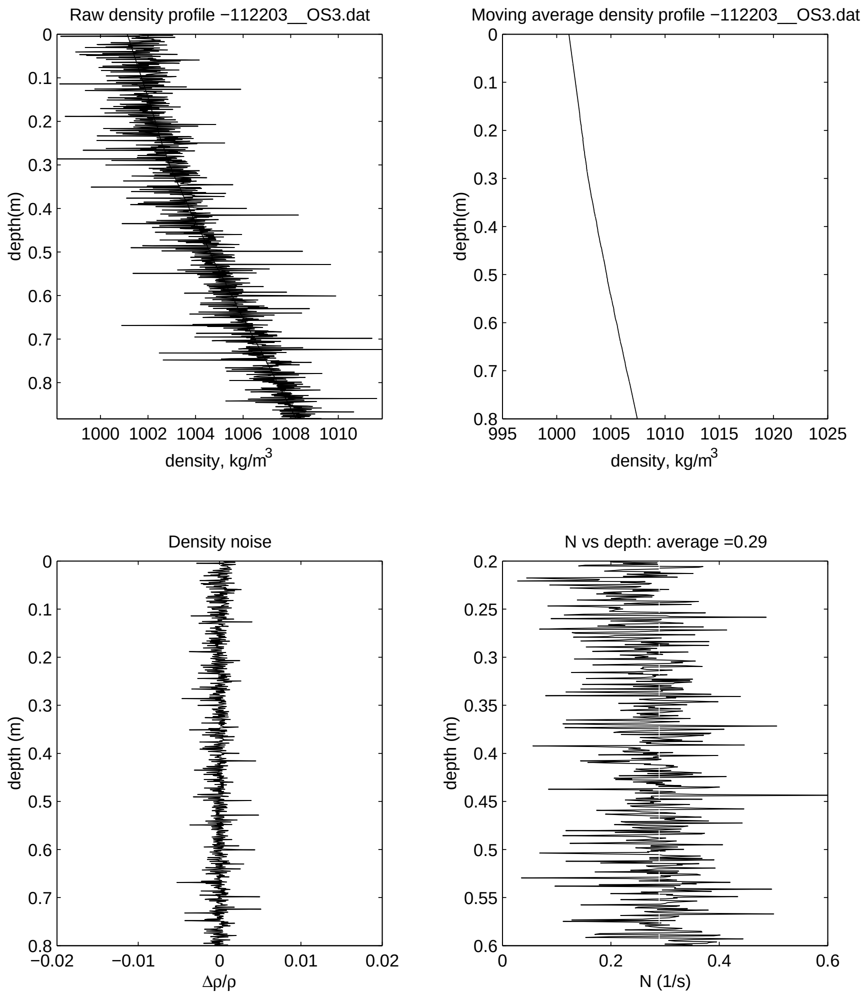

Figure A-44: Density profile for run 112203. Top left: raw density profile. Top right: moving average profile. Bottom left: Density difference between measured and average. Bottom right: Brunt-Väisälä frequency N from data

Run no.		**Time to empty (s)**	**Flow (g/s)**	**Source d (cm)**	**Source depth (m)**	**Bottom depth (m)**	**T** ^oC	S_0 **(g/kg)**	S **(g/kg)**
112203	PS	344	1.75	**0.8**	**0.27**	1.20	20.7	7.0	25.0

Table A.23: Experimental conditions

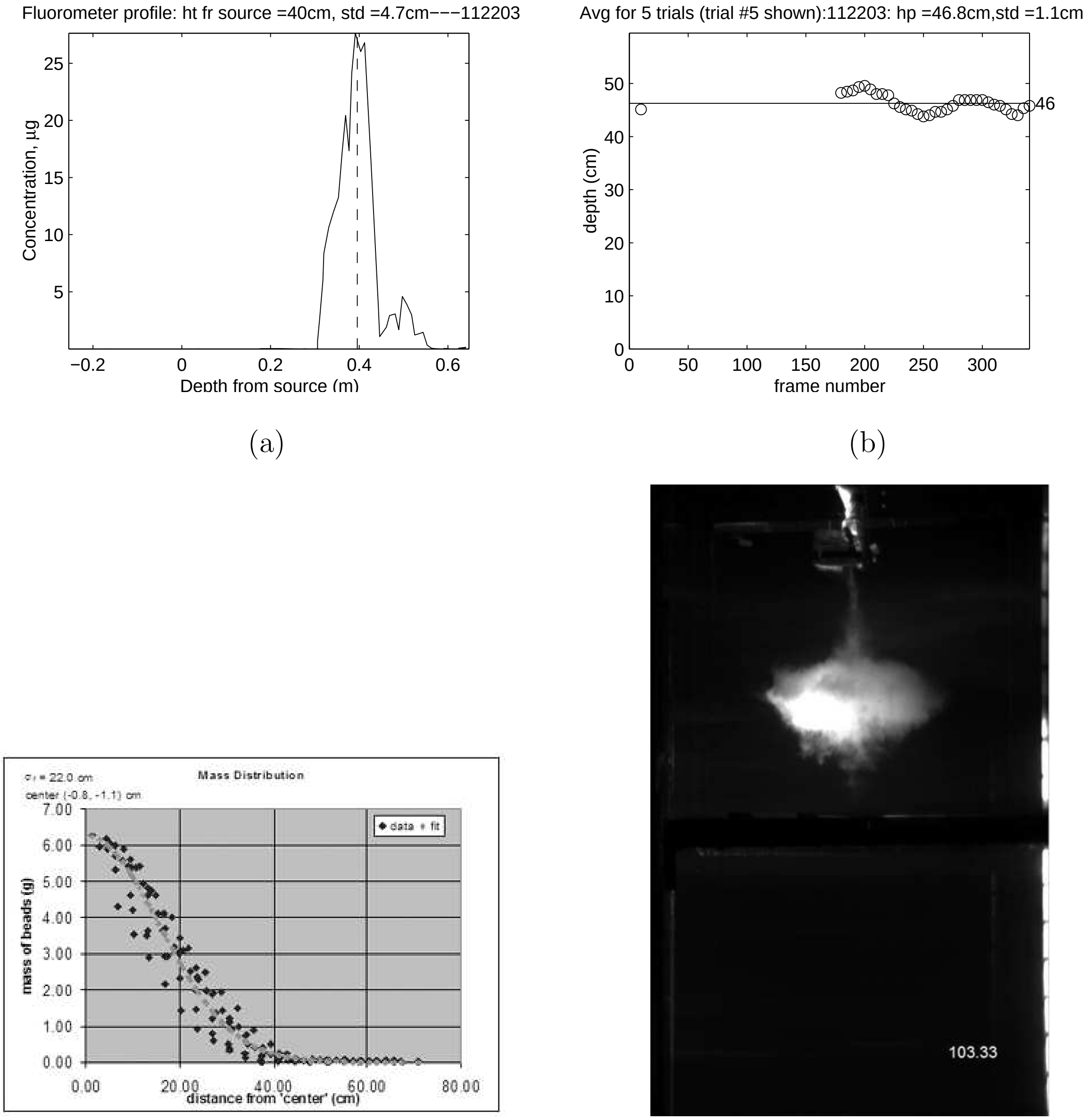

(a) (b)

(c) (d)

Figure A-45: Experimental run 112203: a) Fluorometer profile showing h_t, (b) Peel depths picked at various movie frames, with h_p shown for one example trial, (c) Sediment mass distribution and (d) One image from the experimental run.

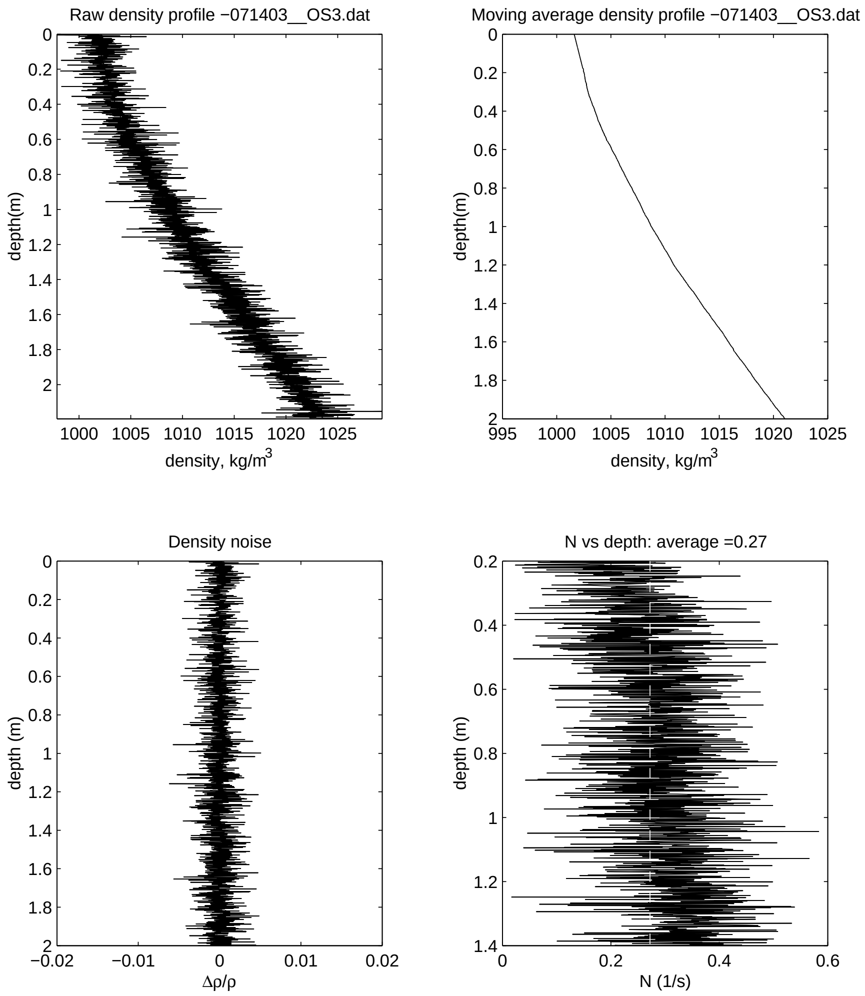

Figure A-46: Density profile for run 071403. Top left: raw density profile. Top right: moving average profile. Bottom left: Density difference between measured and average. Bottom right: Brunt-Väisälä frequency N from data

Run no.		**Time to empty (s)**	**Flow (g/s)**	**Source d (cm)**	**Source depth (m)**	**Bottom depth (m)**	**T** ^oC	S_0 **(g/kg)**	S **(g/kg)**
071403	PS	NA	0.00	**0.8**	**0.27**	1.95	24.0	7.3	21.0

Table A.24: Experimental conditions

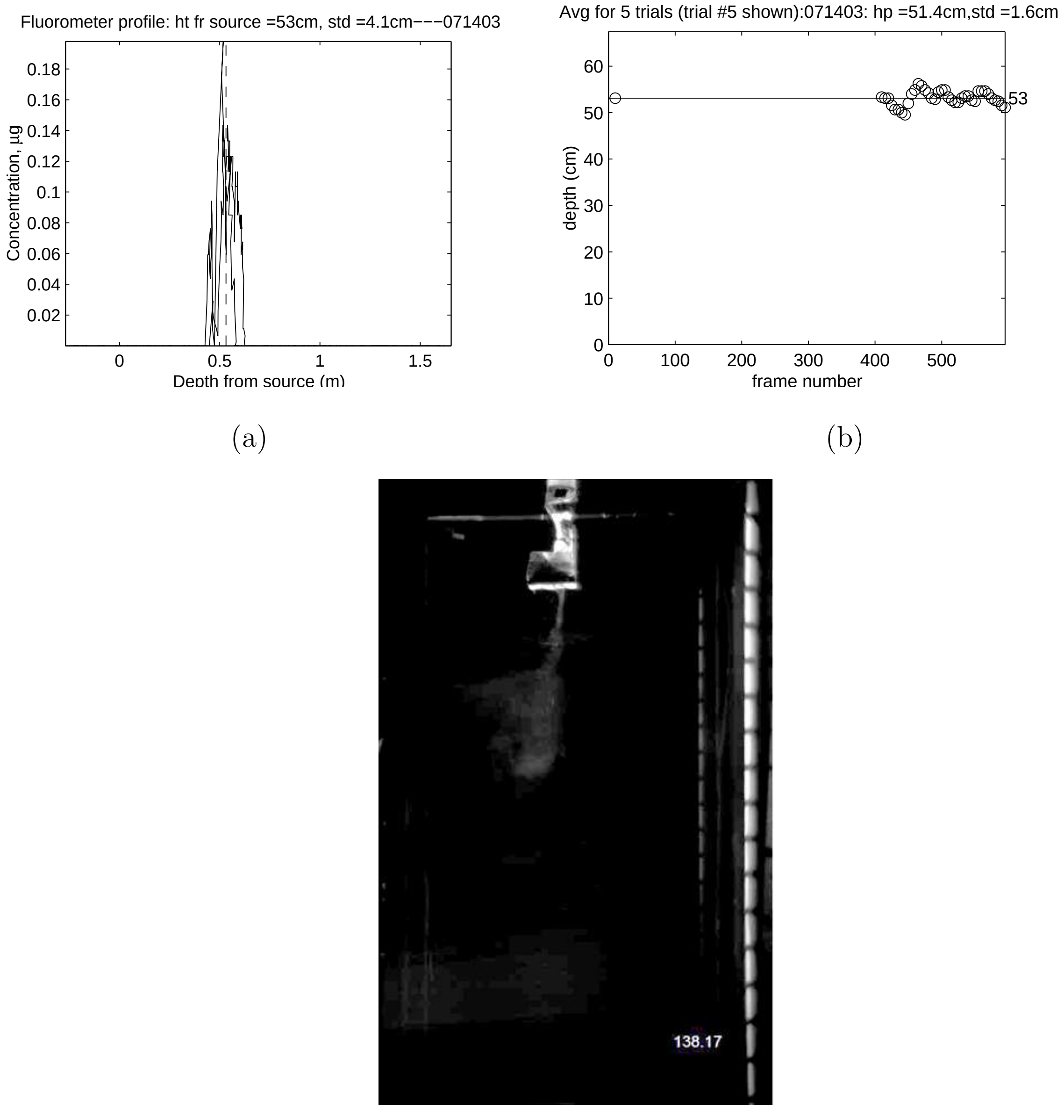

(a) (b)

(c)

Figure A-47: Experimental run 071403: a) Fluorometer profile showing h_t, (b) Peel depths picked at various movie frames, with h_p shown for one example trial, (c) One image from the experimental run.

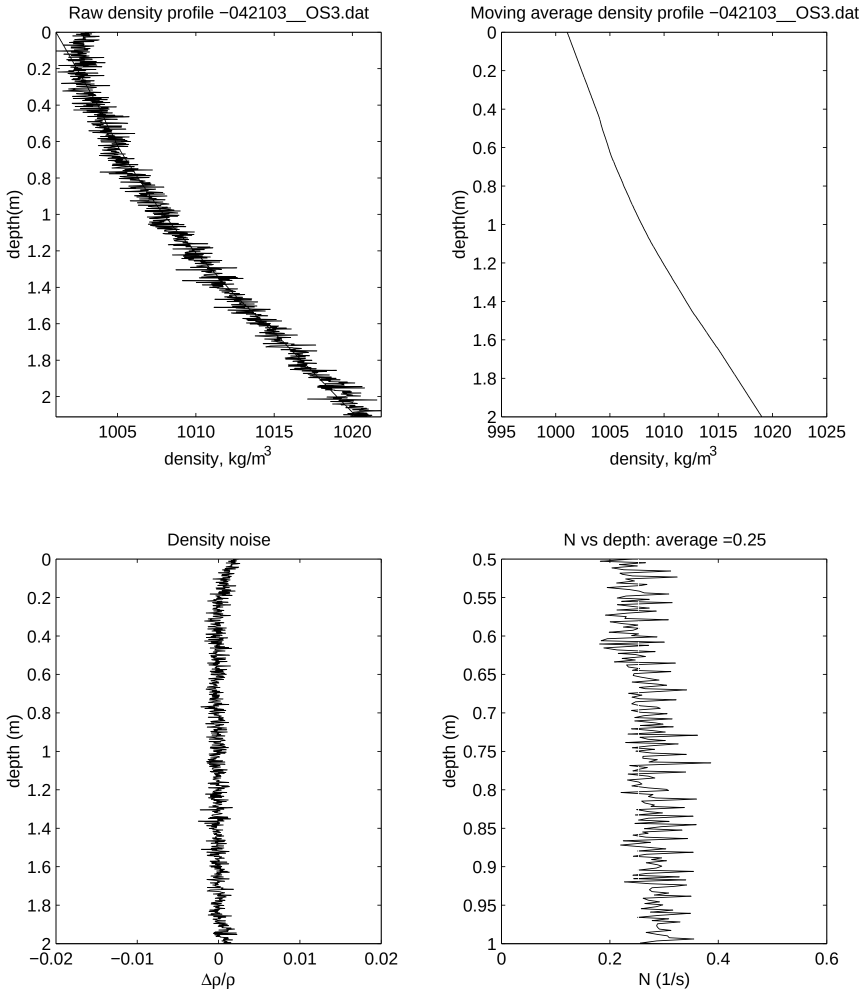

Figure A-48: Density profile for run 042103. Top left: raw density profile. Top right: moving average profile. Bottom left: Density difference between measured and average. Bottom right: Brunt-Väisälä frequency N from data

Run no.		**Time to empty (s)**	**Flow (g/s)**	**Source d (cm)**	**Source depth (m)**	**Bottom depth (m)**	**T** ^oC	S_0 **(g/kg)**	S **(g/kg)**
042103	AE	NA	4.20	**2.5**	**0.29**	1.95	17.0	0.0	0.0

Table A.25: Experimental conditions

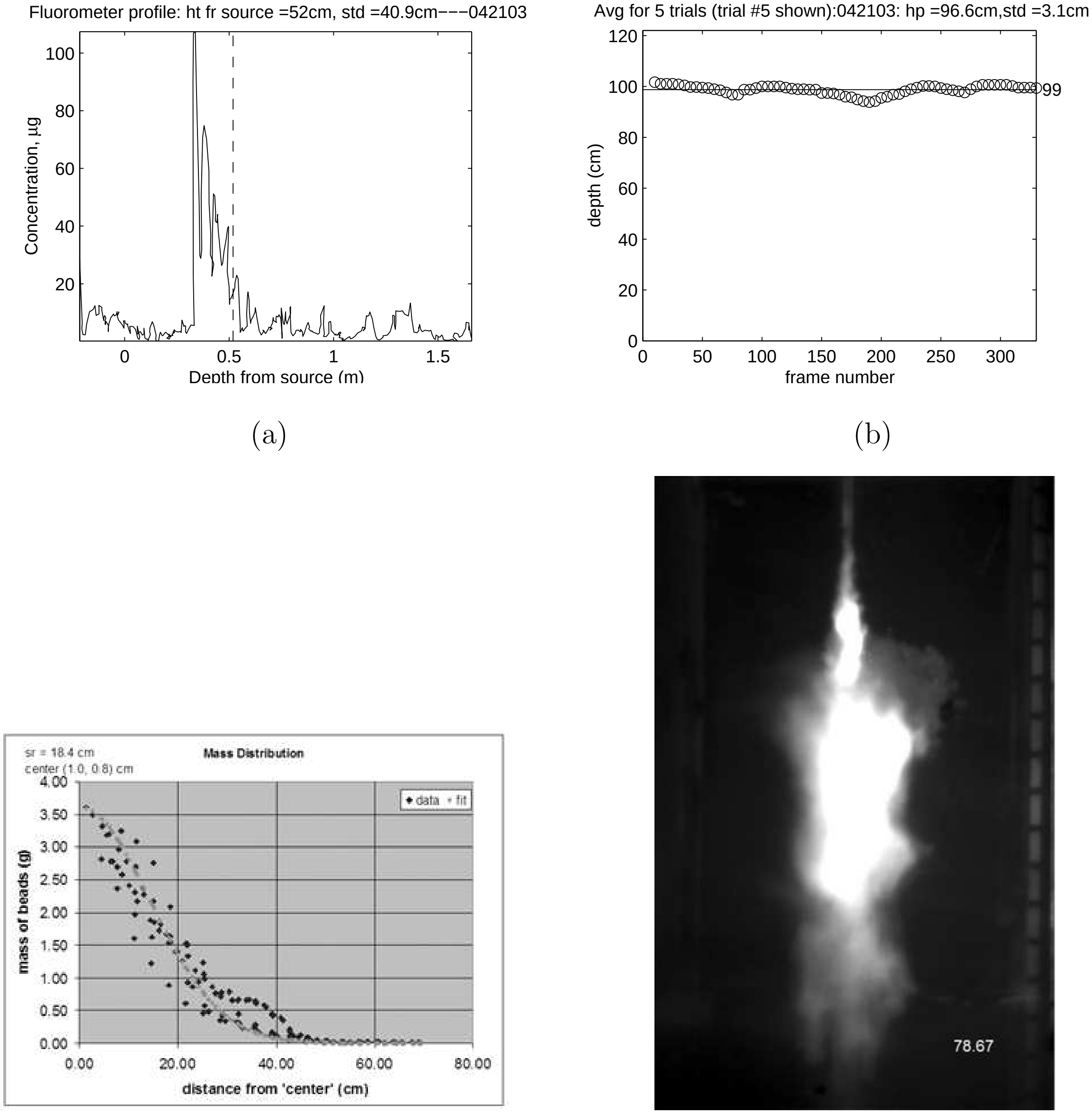

(a)

(b)

(c)

(d)

Figure A-49: Experimental run 042103: a) Fluorometer profile showing h_t, (b) Peel depths picked at various movie frames, with h_p shown for one example trial, (c) Sediment mass distribution and (d) One image from the experimental run.

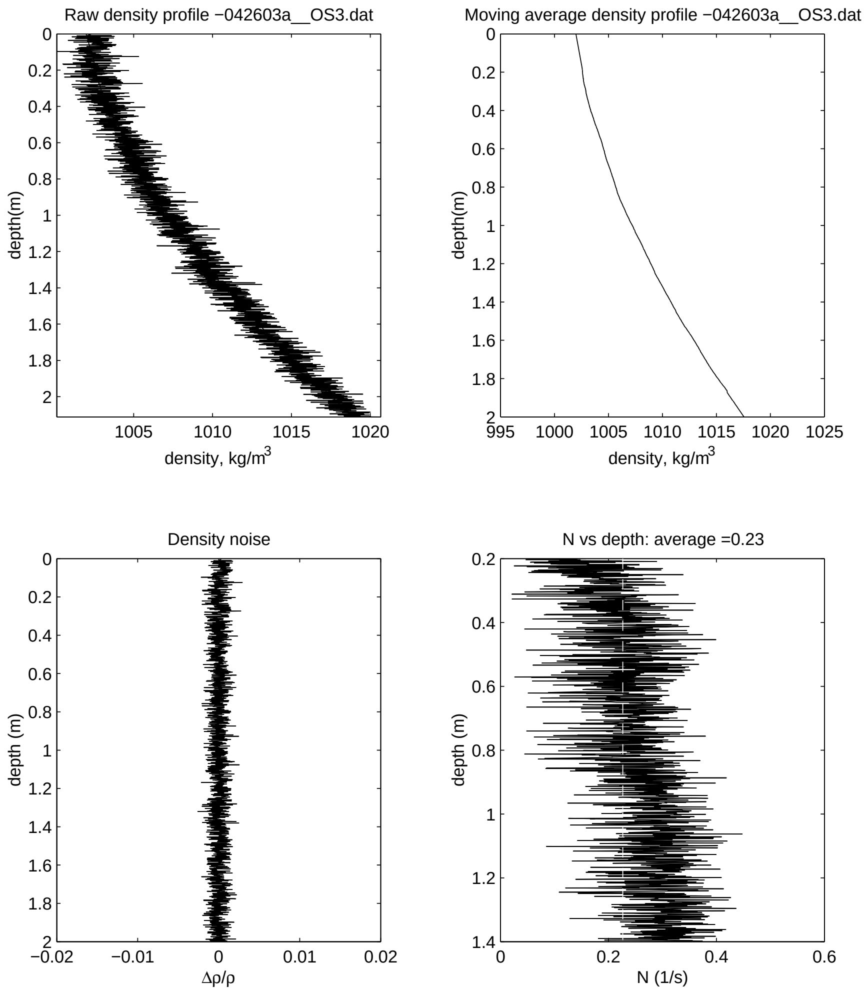

Figure A-50: Density profile for run 042503. Top left: raw density profile. Top right: moving average profile. Bottom left: Density difference between measured and average. Bottom right: Brunt-Väisälä frequency N from data

Run no.		**Time to empty (s)**	**Flow (g/s)**	**Source d (cm)**	**Source depth (m)**	**Bottom depth (m)**	**T** ^oC	S_0 **(g/kg)**	S **(g/kg)**
042503	AE	NA	2.40	**2.5**	**0.29**	1.95	17.0	0.0	29.0

Table A.26: Experimental conditions

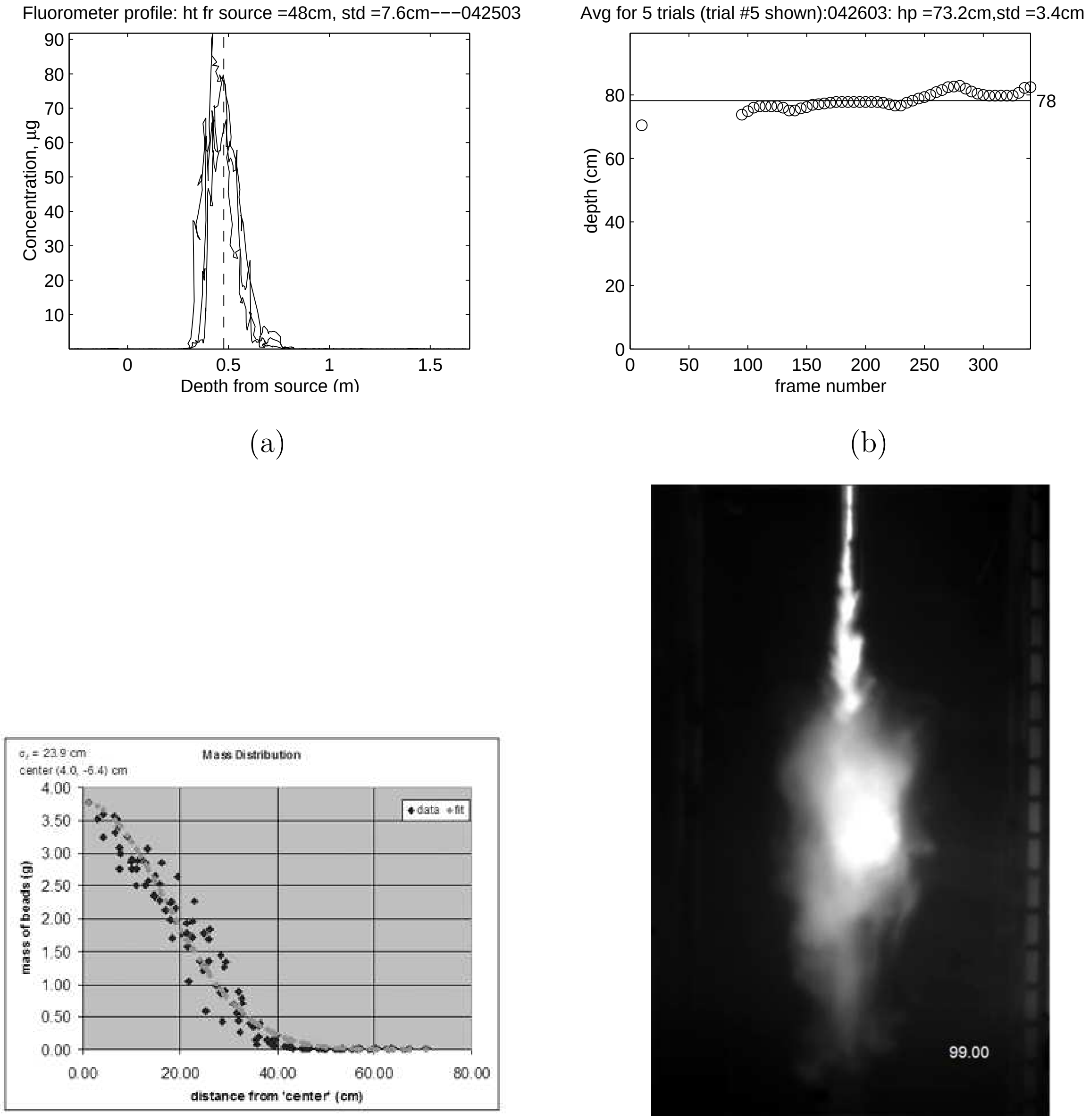

(a) (b)

(c) (d)

Figure A-51: Experimental run 042503: a) Fluorometer profile showing h_t, (b) Peel depths picked at various movie frames, with h_p shown for one example trial, (c) Sediment mass distribution and (d) One image from the experimental run.

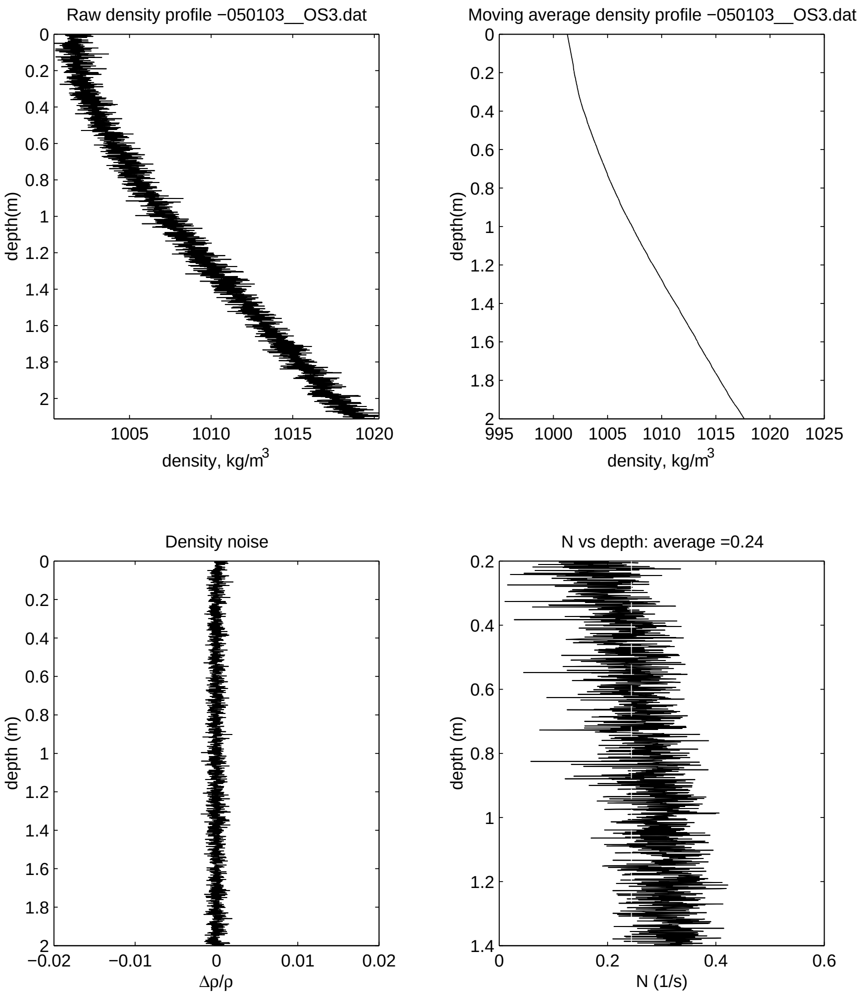

Figure A-52: Density profile for run 050103. Top left: raw density profile. Top right: moving average profile. Bottom left: Density difference between measured and average. Bottom right: Brunt-Väisälä frequency N from data

Run no.		**Time to empty (s)**	**Flow (g/s)**	**Source d (cm)**	**Source depth (m)**	**Bottom depth (m)**	**T** ^oC	S_0 **(g/kg)**	S **(g/kg)**
050103	AE	NA	0.00	**2.5**	**0.29**	1.95	17.0	0.0	65.0

Table A.27: Experimental conditions

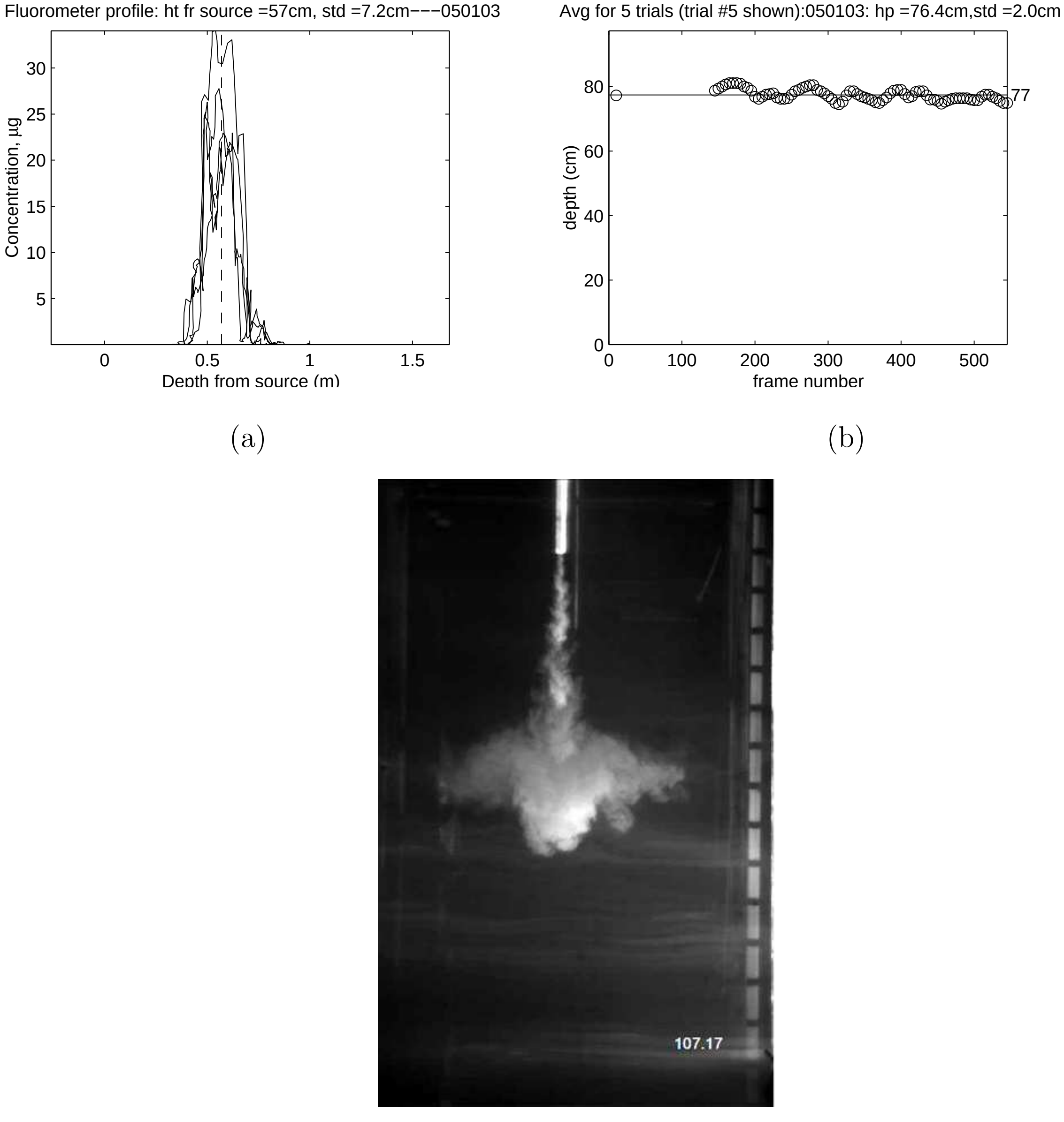

(a)

(b)

(c)

Figure A-53: Experimental run 050103: a) Fluorometer profile showing h_t, (b) Peel depths picked at various movie frames, with h_p shown for one example trial, (c) One image from the experimental run.

A.2 CORMIX inputs

Table A.28 shows the model inputs for the CORMIX model for simulating the experimental conditions.

Run	H (m)	ρ_{bottom} (kg/m^3)	N (1/s)	ρ_{top} (kg/m^3)	ρ_0 (kg/m^3)	Port d (m)	h_t (m)	h_p (m)	Flow Type	N_m
040503	1.66	1015	0.33	996.71	947.35	0.025	0.54	0.69	S5	0.00
042203	1.66	1015	0.27	1002.38	953.57	0.025	0.60	0.78	S5	0.00
041803	1.66	1015	0.28	1001.72	945.19	0.025	0.61	0.78	S5	0.00
120503	1.76	1015	0.27	1001.62	946.96	0.025	0.60	0.77	S5	0.00
121003	1.76	1015	0.27	1001.62	926.36	0.025	0.64	0.82	S5	0.00
071603	1.68	1015	0.29	1000.78	1011.35	0.008	0.26	0.41	S2	42.71
072803	1.68	1015	0.31	998.83	1006.37	0.008	0.28	0.43	S2	8.66
081103	1.76	1015	0.32	996.69	996.91	0.004	0.21	0.28	S5	0.53
081903	1.68	1015	0.36	992.46	1012.55	0.008	0.18	0.30	S2	67.08
082103	1.68	1015	0.27	1002.55	994.37	0.008	0.38	0.51	S5	0.44
082903	1.68	1015	0.26	1003.35	992.31	0.004	0.31	0.44	S2	1.52
090303	1.68	1015	0.29	1000.43	1001.44	0.004	0.29	0.46	S2	18.55
091703	0.93	1015	0.27	1008.01	1011.04	0.008	0.22	0.35	S2	12.22
091903	0.93	1015	0.26	1008.41	1012.11	0.008	0.21	0.36	S2	26.17
092303	0.93	1015	0.25	1008.89	1011.78	0.008	0.23	0.37	S2	20.03
100103	0.93	1015	0.32	1005.28	962.84	0.004	0.35	0.45	S5	0.35
100803	0.93	1015	0.30	1006.26	994.14	0.004	0.26	0.38	S2	1.95
101503	0.93	1015	0.28	1007.70	993.49	0.004	0.29	0.40	S2	1.53
111203	0.93	1015	0.26	1008.27	1012.04	0.004	0.27	0.45	S2	346.72
111703	0.93	1015	0.27	1008.02	1011.32	0.004	0.25	0.43	S2	185.47
111903	0.93	1015	0.27	1007.93	1010.31	0.008	0.28	0.37	S2	10.83
112203	0.93	1015	0.29	1006.96	998.34	0.008	0.31	0.42	S5	0.47
071403	1.68	1015	0.27	1002.13	1004.59	0.008	0.33	0.46	S2	4.03
042103	1.66	1015	0.30	999.90	966.11	0.025	0.53	0.68	S5	0.00
042503	1.66	1015	0.26	1003.61	964.60	0.025	0.60	0.77	S5	0.00
050103	1.66	1015	0.29	1000.47	964.21	0.025	0.54	0.70	S5	0.00

Table A.28: CORMIX inputs and outputs of trap and peel heights, for each experimental run condition.

A.3 Integral Model Inputs

Table A.29 shows the main inputs to the SBPM model. Some of these input values were calibrated with experiments by Socolofsky [52], using the same experimental tank but with bubble plumes.

Run	d(cm) or file	port d(m)	z_0 (m)	z_{max} (m)	m_0 (kg/s)	Q_s (L/min)	$\delta\rho$ (kg/m^3)
040503	AHGlass.dat	0.0250	0.29	1.95	0.0059	3.00	0
041803	AHGlass.dat	0.0250	0.29	1.95	1e-005	3.00	69
042103	AEGlass.dat	0.0250	0.29	1.95	0.0042	3.00	0
042203	AHGlass.dat	0.0250	0.29	1.95	0.0029	3.00	28
042503	AEGlass.dat	0.0250	0.29	1.95	0.0024	3.00	22
050103	AEGlass.dat	0.0250	0.29	1.95	1e-005	3.00	50
071603	PS.dat	0.0080	0.27	1.95	0.0033	2.24	0
072803	PS.dat	0.0080	0.27	1.95	0.0033	2.24	5
073103	PS.dat	0.0040	0.27	1.95	0.00042	2.25	0
081103	PS.dat	0.0080	0.27	1.95	0.00038	0.28	16
081903	PS.dat	0.0080	0.27	1.95	0.0014	1.55	0
082103	PS.dat	0.0080	0.27	1.95	0.0017	1.40	19
082903	PS.dat	0.0040	0.27	1.95	0.0017	0.69	19
090303	PS.dat	0.0040	0.27	1.95	0.0013	1.40	12
091703	PS.dat	0.0080	0.27	0.85	0.0017	1.40	1
091903	PS.dat	0.0080	0.27	0.85	0.0018	1.55	0
092303	PS.dat	0.0080	0.27	0.85	0.0021	1.55	0
100103	PS.dat	0.0040	0.27	0.85	0.00024	0.69	52
100803	PS.dat	0.0040	0.27	0.85	0.00024	0.69	20
101503	PS.dat	0.0040	0.27	0.85	0.00024	0.69	21
111203	PS.dat	0.0040	0.27	0.85	0.0012	1.45	1
111703	PS.dat	0.0040	0.27	0.85	0.0014	1.27	1
111903	PS.dat	0.0080	0.27	0.85	0.0021	1.54	1
112203	PS.dat	0.0080	0.27	0.85	0.0018	1.06	14
120503	0.00483	0.0250	0.19	1.60	0.0022	2.57	34
121103	0.00483	0.0250	0.19	1.60	0.0026	2.57	50

Table A.29: Model inputs for integral plume model, by experiment. Note that "*.dat" files refer to the distribution of sizes from sieve analysis (Table 3-6)

A.4 Model Outputs vs Experiments: Full data set

Figures A-54 and A-55 show all of the model outputs compared with the experimental data points for trap and peel depths.

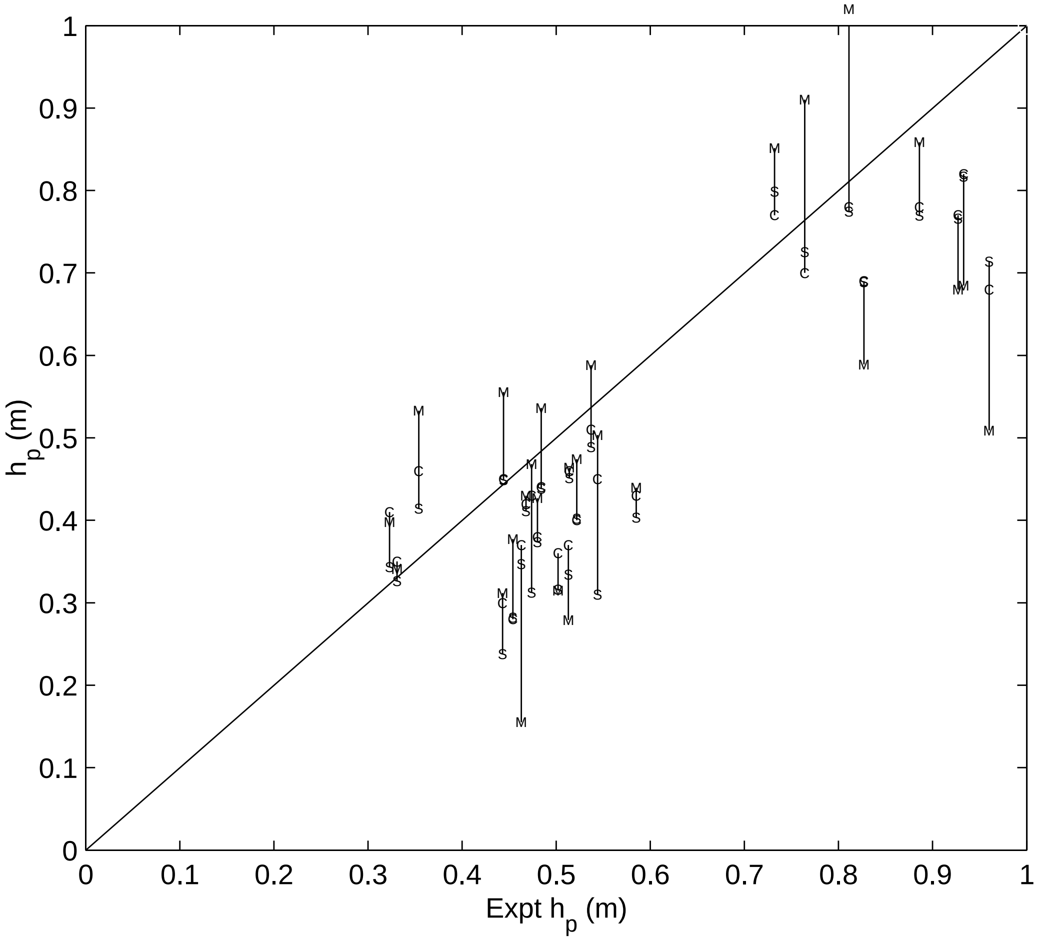

Figure A-54: Comparison between experimental and model predictions for h_p. Data points: S = Equation 2.23; C = CORMIX; M = Integral Model. Lines join the numerical predictions for the same experimental run.

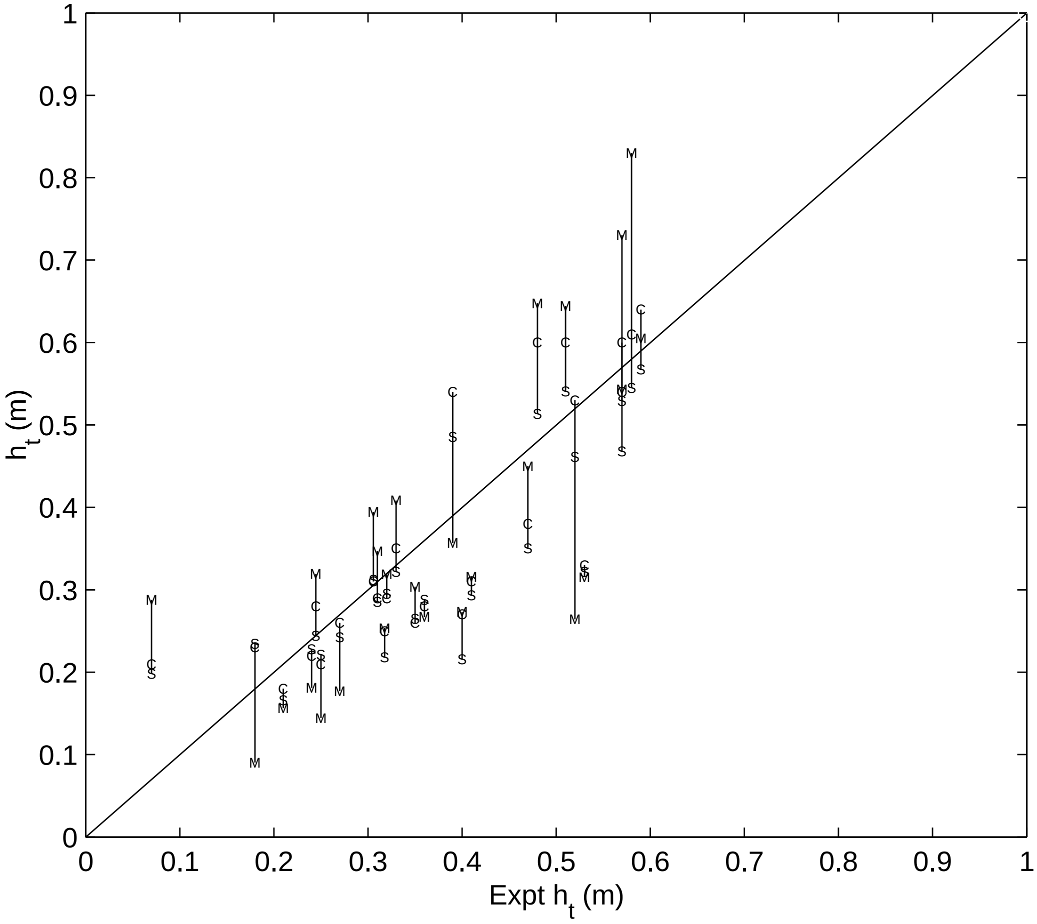

Figure A-55: Comparison between experimental and model predictions for h_t. Data points: S = Equation 2.22; C = CORMIX; M = Integral Model. Lines join the numerical predictions for the same experimental run.

Bibliography

[1] Illinois EPA: Effects of destratification and circulation. http://www.epa.state.il.us/water/conservation-2000/lake-notes/aeration-circulation/effects.html.

[2] Experimental discharge of gas and oil at Helland Hansen – June 2000. Technical report, SINTEF Applied Chemistry, 2000.

[3] E. E. Adams, J. Caulfield, and X. Y. Zhang. Sinking of a CO_2-enriched gravity current. In *Proc. XXVII IAHR Congress, San Francisco*, 1997.

[4] E. E. Adams, D. Golomb, X. Y. Zhang, and H. J. Herzog. Confined release of CO_2 into shallow sea water. In *Direct Ocean Disposal of Carbon Dioxide*, pages 153–164. TERRAPUB, Toyko, 1995.

[5] G. Alendal and H. Drange. Two-phase, near field modeling of purposefully released CO_2 in the ocean. *Journal of Geophysical Research*, 106(C1):1085–1096, 2001.

[6] A. Angelopoulos and G. D. Benign form of carbon dioxide sequestration in the ocean. *Abstracts of Papers of the American Chemical Society*, 222(Part 1):312–COLL, 2001.

[7] T. Asaeda and J. Imberger. Structure of bubble plumes in linearly stratified environments. *Journal of Fluid Mechanics*, 249:35–57, 1993.

[8] D. I. Auerbach, J. A. Caulfield, E. E. Adams, and H. J. Herzog. Impacts of ocean CO_2 disposal on marine life: I. a toxicological assessment integrating constant-

concentration laboratory assay data with variable concentration field exposure. *Environmental Modeling and Assessment*, 2:333–343, 1997.

[9] I. Aya, K. Yamane, and K. Shiozaki. Proposal of self sinking CO_2 sending system: Cosmos. *Greenhouse Gas Control Technologies*, pages 269–274, 1999.

[10] W. D. Baines and A. M. Leitch. Destruction of stratification by bubble plumes. *Journal of Hydroaulic Engineering*, 118(4):559–577, 1992.

[11] K. Caldeira and G. H. Rau. Accelerating carbonate dissolution to sequester carbon dioxide in the ocean: Geochemical implications. *Geophysical Research Letters*, 27(2):225–228, 2000.

[12] S. S. S. Cardoso and A. W. Woods. Mixing by a turbulent plume in a confined stratified region. *Journal of Fluid Mechanics*, 250:277–305, 1993.

[13] S. S. S. Cardoso and M. Zarrebini. Sedimentation from surface currents generated by particle-laden jets. *Chemical Engineering Science*, 57(8):1425–1437, 2002.

[14] S. N. Carey, H. Sigurdsson, and R. S. J. Sparks. Experimental studies of particle-laden plumes. *Journal of Geophydical Research*, 93(B12):15314–15328, 1988.

[15] C.-C. P. Caulfield and A. W. Woods. Plumes with non-monotonic mixing behaviour. *Geophysical and Astrophysical Fluid Dynamics*, 79:173–199, 1995.

[16] J. A. Caulfield, E. E. Adams, D. I. Auerbach, and H. J. Herzog. Impacts of ocean CO_2 disposal on marine life: Ii. probablistic plume exposure model used with a time-varying dose-response analysis. *Environmental Modeling and Assessment*, 2:345–353, 1997.

[17] C. J. Chen and W. Rodi. *Vertical Turbulent Buoyant Jets - A Review of Experimental Data.* Pergamon Press, 1980.

[18] M. H. Chen and S. S. S. Cardoso. The mixing of liquids by a plume of low-reynolds number bubbles. *Chemical Engineering Science*, 55:2585–2594, 2000.

[19] H. J. Creighton and W. A. Koehler. *Electrochemistry, vol. II: Applications*. Wiley, 1944.

[20] B. Crounse, E. J. Wannamaker, and E. E. Adams. Integral model of a multiphase plume in quiescent stratification. *Submitted to Journal of Hydraulic Engineering*, 2004.

[21] B. C. Crounse. Modeling buoyant droplet plumes in a stratified environment. Master's thesis, Massachusetts Institute of Technology, 2000.

[22] S. Dhamotharan, J. S. Gulliver, and H. G. Stefan. Unsteady one-dimenstional settling of suspended sediment. *Water Resources Research*, 17(4):1125–1132, 1981.

[23] W. Dietrich. *Water Resources Research*, 18(6):1615–1626, 1982.

[24] F. Dobran. *Volcanic Processes: Mechanism in Material Transport*. Kluwer Academic/Plenum Publishers, 1997.

[25] R. L. Doneker and G. H. Jirka. *D-CORMIX continuous dredge disposal mixing zone water quality model laboratory and field data validation study*, 1997.

[26] H. B. Fischer, E. J. List, R. C. Y. Koh, and J. Imberger. *Mixing in Inland and Coastal Waters*. Academic Press, 1979.

[27] J. E. García. Density of aqueous solutions of CO_2. Technical Report LBNL-49023, Lawrence Berkeley National Laboratory, 2001.

[28] P. Haugen and H. Drange. Sequestration of CO_2 in the deep ocean by shallow injection. *Nature*, 357(28):1065–1072, 1992.

[29] H. Herzog, B. Eliasson, and O. Kaarstad. Capturing greenhouse gases. *Scientific American*, February 2000.

[30] A. J. Hogg, H. E. Huppert, and M. A. Hallworth. Reversing buoyancy of particle-driven gravity currents. *Physical Fluids*, 11(10):2891–2900, 1999.

[31] G. Holder, L. Mokka, and R. Warzinski. Formation of hydrates from single-phase aqueous solutions and implications for ocean sequestration of CO_2. In *Preprints of Spring 2000 National Meeting in San Diego, CA*. ACS Division of Fuel Chemistry, 2001.

[32] P. Holland. *Offshore blowouts: Causes and Control.* Gulf Pub. Co., 1997.

[33] G. R. Hunt and N. G. Kaye. Virtual origin correction for lazy turbulent plumes. *Journal of Fluid Mechanics*, 435:377–396, 2001.

[34] G. H. Jirka, R. L. Doneker, and S. W. Hinton. *User's manual for CORMIX: A hydrodynamic mixing zone model and decision support system for pollutant discharges into surface waters.*

[35] J. Knutzen. Effects of decreased pH on marine organisms. *Marine Pollution Bulletin*, 12(1):25–29, 1981.

[36] H. E. Kobus. Analysis of the flow induced by air-bubble plueme systems. In *Proceedings of the 11th International Conference of Coastal Engineering, London*, pages 1016–1031. ASCE, 1968.

[37] A. M. Leitch and W. D. Baines. Liquid volume flux in a weak bubble plume. *Journal of Fluid Mechanics*, 205:77–98, 1989.

[38] C. J. Lemckert and J. Imberger. Energetic bubble plumes in arbitrary stratification. *Journal of Hydraulic Engineering*, 119(6):680–703, 1993.

[39] E. J. List. *Mechanics of Turbulent Buoyant Jets and Plumes (Ed. Rodi, W.).* Pergamon Press, 1982.

[40] S. C. McCutcheon, J. L. Martin, and T. O. J. Barnwell. *Handbook of Hydrology.* McGraw-Hill, New York, 1993.

[41] T. J. McDougall. Bubble plumes in stratified environments. *Journal of Fluid Mechanics*, 85(4):655–672, 1978.

[42] J. H. Milgram. Mean flow in round bubble plumes. *Journal of Fluid Mechanics*, 133:345–376, 1983.

[43] F. M. M. Morel and J. G. Hering. *Principles and Applications of Aquatic Chemistry.* Wiley-Interscience, 1993.

[44] B. R. Morton, G. I. Taylor, and J. S. Turner. Turbulent gravitational convection from maintained and instantaneous sources. In *Proceedings of the Royal Society of London, Series A, Mathematical and Physical Sciences*, volume 234, pages 1–23, 1956.

[45] C. N. Murray, L. Visitini, G. Bidoglio, and B. Henry. Permanent storgae of carbon dioxide in the marine environment: The solid CO_2 penetrator. *Energy Conversion Management*, 37(6-8):1067–1072, 1996.

[46] N. Nakanishi, T. Ohsumi, and K. Shitashima. Sequestering of CO_2 in a deep ocean. *Technical Report, Central Research Insitute of Electric Power Industry*, 1994. 1646 Abiko, Abiko-City, Chiba 270-11, Japan.

[47] G. H. Rau and K. Caldeira. Enhanced carbonate dissolution: a means of sequestering waste co_2 as ocean bicrabonate. *Energy Conversion and Management*, 40:1803–1813, 1999.

[48] L. S. Reingold. An experimental comparison of bubble and sedimment plumes in stratified environments. Master's thesis, Massachusetts Institute of Technology, 1994.

[49] G. J. Ruggaber. *Dynamics of particle clouds related to open-water sediment disposal.* PhD thesis, Massachusetts Institute of Technology, 2000.

[50] T. Sato, S. Abe, and H. Miyata. Numerical simulation of droplet flow with mass transfer through interface. In *Proceedings of FEDSM 1998 ASME Fluids Engineering Division Summer Meeting, Washington, DC*, 1998.

[51] T. Sato, T. Kajishima, and R. Naguosa. CO_2 sequestration at sea by gas-lift system of shallow injection and deep releasing. *Environmental Science and Technology*, 34:4140–4145, 2000.

[52] S. A. Socolofsky. *Laboratory experiments of multi-phase plumes in stratification and crossflow.* PhD thesis, Massachusetts Institute of Technology, 2001.

[53] S. A. Socolofsky and E. E. Adams. Multi-phase plumes in uniform and stratified crossflow. *Journal of Hydraulic Research*, 40(6):661–672, 2002.

[54] S. A. Socolofsky and E. E. Adams. Liquid volume fluxes in stratified multiphase plumes. *Journal of Hydraulic Engineering*, 11:905 – 914, 2003.

[55] S. A. Socolofsky and E. E. Adams. The role of slip velocity in controlling the behavior of stratified multi-phase plumes. *Journal of Hydraulic Engineering*, 2003, in press.

[56] O. Söhnel and P. Novotný. *Densities of Aqueous Solutions of Inorganic Substances.* Elsevier, New York, 1985.

[57] R. S. J. Sparks, R. T. Bonnecaze, H. Huppert, J. R. Lister, M. A. Hallworth, H. Mader, and J. Philips. Sediment-laden gravity currents with reversing buoyancy. *Earth and Planetary Science Letters*, 114:243–257, 1993.

[58] R. S. J. Sparks, M. I. Bursik, S. N. Carey, J. S. Gilbert, L. S. Glaze, H. Sigurdsson, and A. W. Woods. *Volcanic Plumes.* Wiley, 1997.

[59] R. S. J. Sparks, S. N. Carey, and H. Sigurdsson. Sedimentation from gravity currents generated by turbulent plumes. *Sedimentology*, 38:839–856, 1991.

[60] K. H. Tacke, H. G. Schubert, D. J. Weber, and K. Schwerdtfeger. Characteristics of round vertical gas bubble jets. *Metallurgical Transactions B*, 16B(2):263–275, 1985.

[61] M. N. Tamburri, E. T. Peltzer, G. E. Friederich, I. Aya, K. Yamane, and P. G. Brewer. A field study of the effects of CO_2 ocean disposal on mobile deep-sea animals. *Marine Chemistry*, 72:95–101, 2000.

[62] J. S. Turner. Turbulent entrainment: the development of the entrainment assumption, and its application to geophysical flows. *Journal of Fluid Mechanics*, 173:431–471, 1986.

[63] E. J. Wannamaker. Modeling carbon dioxide hydrate particle releases in the deep ocean. Master's thesis, Massachusetts Institute of Technology, 2002.

[64] E. J. Wannamaker and E. E. Adams. Modeling descending carbon dioxide injections in the ocean. *Submitted to Journal of Hydraulic research*, 2004.

[65] R. P. Warzinski, R. J. Lynn, and G. D. Holder. The impact of CO_2 clathrate hydrate on deep ocean sequestration of CO_2: experimental observations and modeling results. *Annals of the New York Academy of Sciences*, 912:226–234, 2000.

[66] R. T. Watson, editor. *Climate Change 2001: Synthesis Report, Intergovernmental Panel on Climate Change (IPCC).* Cambridge University Press, 2001.

[67] A. W. Woods and J. W. M. Bush. Dimensions and dynamics of megaplumes. *Journal of Geophysical Research*, 104(C9):20495–20507, 1999.

[68] A. Wüest, N. H. Brooks, and D. M. Imboden. Bubble plume modeling for lake restoration. *Water Resources Research*, 28(12):3235–3250, 1992.

[69] T. P. Yeh. *Transverse mixing of heated effluents in open channel flows.* PhD thesis, University of Iowa, 1974.

[70] M. Zarrebini and S. S. S. Cardoso. Patterns of sedimentation from surface currents generated by turbulent plumes. *AICHE Journal*, 46(10):1947–1956, 2000.